

NORTHWESTERN UNIVERSITY

Classically Modeling the Coupling Between Quantum Emitters and Noble  
Metal Nanoparticles

A DISSERTATION

SUBMITTED TO THE GRADUATE SCHOOL  
IN PARTIAL FULFILLMENT OF THE REQUIREMENTS

for the degree

DOCTOR OF PHILOSOPHY

Field of Chemistry

By

Thomas A. R. Purcell

EVANSTON, ILLINOIS

August 2018

© Copyright by Thomas A. R. Purcell 2018

All Rights Reserved

## ABSTRACT

Classically Modeling the Coupling Between Quantum Emitters and Noble Metal Nanoparticles

Thomas A. R. Purcell

This dissertation develops computational models to study the optical coupling between plasmonic nanoparticles and quantum emitters. A large number of nanophotonic applications function by using either plasmon enhanced fields to enhance optical processes within quantum emitters or the sensitivity of plasmon resonances to their environment. Developing computational methods to fully describe the interactions between metal nanoparticles and emitters is vital for the future design of nanophotonic devices. Here we incorporate classical and semiclassical models of quantum emitters into classical electrodynamics methods, which have been previously demonstrated to accurately study the optical response of metal nanoparticles. First we describe the absorption of a quantum dot film with a classical dielectric and a quantum mechanical inhomogeneously broadened three level system. We then describe the coupling of the quantum dots to a gold nanoisland film, providing insights into how to best design photodetectors. We then extend that model to include effects from a film of linker molecules, investigating how the orientation of the molecular induced dipoles affect the plasmon resonances of the nanoislands. Then we develop a new methodology to study the chiroptical coupling between an arbitrary

plasmonic system and thin molecular films. Finally we utilized the built up methodology to attempt to optimize metal nanostructures for dye-sensitized solar cell applications. The results from this dissertation provide a framework for the future study of quantum emitters coupled to metal nanoparticles.

## **Acknowledgements**

The two people who had the greatest influence on me becoming a scientist and finishing my Ph. D. are my parents Elsa Reichmanis and Frank Purcell. As chemists themselves they always tried to expose me to various scientific experiences and encouraged me to take opportunities in the sciences, even bringing me to American Chemical Society meetings when I was younger. I have to especially thank my mom for being a sounding board and editor throughout my graduate school career. I also have to thank my sister, Liz, and brother, Edd, for being there for me and keeping me in line for my entire life. Finally I have to thank my Uncle Vince for his continued interest in my work.

The first time I considered becoming physical or computational scientist was in high school thanks to a group of great teachers. Mr. Seiler, Mr. Scipioni, and Mr. Maruschak taught my AP Chemistry, AP Physics, and AP Computer Science classes respectively. They challenged me to not only reach my academic potential, but also gave me the latitude to explore my interests within and sometimes slightly beyond the curriculum. They also pushed me to get out of my comfort zone by consistently assigning group work in a way where I could not take over and do everything myself. Thank you Mr. Seiler, Mr. Scipioni, and Mr. Maruschak for introducing me to the fields that I would get my Ph. D. in.

Prof. Mark Tuckerman at New York University was the person who inspired me to become a chemist let alone a theoretical chemist. Before his general chemistry class my exposure to chemistry made me think it was insular, a field focused solely on molecular interactions and

chemical reactions. In his class we learned the basics of quantum mechanics letting me recognize that chemistry is the intersection of mathematics, physics and what is traditionally considered chemistry. The next year I would join his group as an undergraduate researcher where he and one of his post docs Dr. Michel Cudent would teach me how to be a successful computational chemist. I have to thank them and the entire Tuckerman group for introducing me to computational chemistry and chemical research.

My Ph.D. would not be successful without the great working environment on the 4<sup>th</sup> floor of Ryan Hall. The Seideman group has been vital for my progress here so I have to thank my former and current group members, who helped guide me throughout my time at Northwestern: Dr. Ramakrishna Sesa Shankar (Sai), Dr. Shane Parker, Dr. Benjamin Ashwell, Dr. Andrew Rasmussen, Prof. Matthew Sonntag, Dr. Thomas Grohmann, Dr. Partha Pal, Dr. Erik Hoy, Dr. Dmitry Zhdanov, Dr. Maxim Artamonov, Dr. Naihao Chiang, Dr. Emily Sprague Klien, Xinyuan You, Azra Dizdarevic, Dr. Yuling Liu, Dr. Alexei Deinega, and Dr. Andrew Hu. I also have to thank my other coworkers in the other theory groups that contributed to my success at Northwestern: Prof. Craig Chapman, Dr. Andrew Sirjoosingh, Prof. Jefferson Bates, Prof. Bess Vlasisavljevich, Dr. Matt MacLeod, Dr. Lindsey Madison, Dr. Kevin Kohlstedt, Marc Bourgeois, Dr. Martin Mosquera, Dr. Wendu Ding, Dr. Dhara Trivedi, Dr. Mike McAnally, Dr. Vince Cho, Dr. Adam Ashwell, Prof. Matthew Reuter, Dr. Micaela Matta, Dr. Bo Fu, and Dr. Bryan Lau. Finally I'd like to thank my current and former officemates for providing a good work environment Dr. Tomekia Simon, Matthew Kelley, Prof. Kelsey Stocker, Prof. Wei Lin, Dr. Chad Heaps, Laurel Jones, Nils Strand, and Yeonjun Jeong. Finally I'd like to thank the Program Assistants Tory Helgeson and Jenna Pawlicki for helping ensure everything runs smoothly on the Theory floor.

In particular I'd like to thank my friends at Northwestern University for the climbing, games and general good times in no particular order: Dr. Jackie Cantwell, Dr. Josh Szelkely, Dr. Laura Lilley, Ryan Reynolds, Anh Le, Chelsea Mueller, Dolev Rimmerman, Nolan Wong, Jennifer Grant, Dr. Mark Kokish, Dr. Kelvin Chang, Dr. Gavin Campbell, Meg Lee, David Roszkowski, Daniel Kim, Prof. Stephanie Knezz, Ruby Kruger, Dr. Rachel Harris, Garret Lau, Aparna Sodhi, and Caitlin Bray

I thank Tamar Seideman for being an excellent adviser my five years at Northwestern. She has allowed me to grow as an independent researcher and work on and develop projects that I find both interesting and challenging. Without her patient guidance I would not be the researcher I am today.

I also thank my collaborators for the research in this dissertation. Prof. Yossi Paltiel has been a valuable mentor throughout my Ph. D. helping me get multiple projects to publications since our collaboration started. Matan Galanty and Dr. Shira Yochelis were vital in providing the experimental work for my first publication on the quantum dot photodetectors. I thank Prof. Maxim Sukharev for hosting me at Arizona State University and our work together on the Maxwell-Liouville method.

I thank Prof. Leeor Kronik and his group for my month long visit to his group. I learned a lot about Density Functional Theory and the culture at the Weizmann Institute. I particularly thank Dr. David Egger, Dr. Ariel Biller, Georgia Prokopiou, and Daphna Yahav for helping get situated in the group.

Finally I'd like to thank my current and former committee members: Prof. George Schatz, Prof. Toru Shiozaki, and Prof. Teri Odom for their advice and guidance throughout my time at

Northwestern University. Their insights allowed me to rethink my projects and connect them to real world phenomenon and played a crucial role in getting my doctoral degree.

## List of abbreviations

<b>E</b>	Electric Filed
<b>H</b>	Magnetic Filed
<b>D</b>	Electric Flux Density
<b>B</b>	Magnetic Flux Density
<b>P</b>	Electric Polarization Density
<b>M</b>	Magnetic Polarization Density
$\epsilon_0$	Vacuum Permittivity
$\mu_0$	Vacuum Permeability
<b>FDTD</b>	Finite Difference Time Domain
<b>ML</b>	Maxwell-Liouville
$\Delta_w$	Grid Spacing in the $w$ Direction, $w = x, y, \text{ or } z$
$\Delta_t$	Time Step
<b>TF/SF</b>	Total Field/Scattered Field
<b>PML</b>	Perfectly Matched Layer
<b>CPML</b>	Convolution Perfectly Matched Layer
<b>PBC</b>	Periodic Boundary Condition
<b>ADE</b>	Auxiliary Differential Equations

SPR	Surface Plasmon Resonance
LSPR	Local Surface Plasmon Resonance
SPP	Surface Plasmon Polariton
CD	Circular Dichroism
$\mu_B$	Bohr Magneton
FMN	Flavin mononucleotide
MNP	Metal Nanoparticle
QD	Quantum Dot
UV	Ultraviolet
DSSC	Dye-Sensitized Solar Cell
PCE	Power Conversion Efficiency
GA	Genetic Algorithm
IPCE	Incident Photon Current Efficiency
TERS	Tip Enhanced Raman Spectroscopy
SERS	Surface Enhanced Raman Spectroscopy

## Table of Contents

ABSTRACT	3
Acknowledgements	5
List of abbreviations	9
Table of Contents	11
List of Figures	15
Chapter 1. Introduction	26
1.1 Optics of Metal Nanoparticles	26
1.1.1 Maxwell's Equations	26
1.1.2 Dielectric Response of a Free Electron Gas	28
1.1.3 The Effects of Inter-Band Transitions	29
1.2 Surface Plasmon Resonance	30
1.2.1 Surface Plasmon Polaritons	31
1.2.2 Local Surface Plasmon Resonance	31
1.3 Applications	33
1.3.1 Plasmonic Devices	34
1.3.2 Raman Spectroscopy	35
1.4 Coupling Between Plasmons and Quantum Emitters	36

	12
1.5 Dissertation Overview	37
Chapter 2. Modeling Classical Electrodynamics with Finite-Difference Time-Domain	38
2.1 Coupled Differential Equation Scheme for FDTD	39
2.2 The FDTD Algorithm	40
2.2.1 Applying the Finite Difference Scheme to Maxwell's Equations	41
2.3 Dispersive Materials within FDTD	43
2.4 Boundary Conditions	44
2.4.1 Periodic Boundary Conditions	45
2.4.2 Perfectly Matched Layers	45
2.5 Generating Incident Radiation	50
2.5.1 Total Field/Scattered Field	51
2.6 Time Stepping with the Yee Algorithm	56
Chapter 3. Coupling Quantum Emitters to Random 2D Nanoplasmonic Structures	58
3.1 Introduction	59
3.2 Methodology	60
3.2.1 Theoretical Methods	60
3.2.2 Experimental Methods	62
3.3 Results	64
3.3.1 Building the Gold Nanoisland Model	64
3.3.2 The Nature of the Nanoisland-Quantum Dot Coupling	67
3.3.3 Experimental Confirmation Through Changing the Quantum Dot Number Density	71

	13	
3.4	Conclusions	75
Chapter 4.	The Maxwell-Liouville Method to Better Model Quantum Emitters	77
4.1	Introduction	78
4.2	Methodology	79
4.2.1	Maxwell-Liouville Propagator	79
4.2.2	Inhomogeneously Broadened States	80
4.3	Results	81
4.3.1	Scattering from a Molecular Sphere	81
4.3.2	Photon Echoes From Inhomogeneously Broadened states	83
4.4	Conclusion	86
Chapter 5.	Determining the Molecular Dipole Orientation on Nanoplasmonic Structures	87
5.1	Introduction	88
5.2	Methodology	89
5.3	Results	92
5.3.1	Modifying the LSPR of Tetrahedral Nanoparticles with Molecular Coatings	92
5.3.2	The Effects of Linker Molecules on the Coupling Between Quantum Dots and Nanoisland Films	94
5.4	Conclusions	103
Chapter 6.	A Study of Chiral Imprinting	105
6.1	Introduction	106
6.2	Methodology	107

	14
6.3 Results	112
6.3.1 Chiral Imprinting For Gold Nanospheres	112
6.3.2 Mixed Orientational and Isotropic Coupling Between Chiral Molecules and a Gold Nanocross Array	116
6.3.3 How Chiral Molecules Affect the Coupling Between Nanoparticles and Quantum Dots	122
6.4 Conclusions	125
Chapter 7. Optimizing Nanoparticles for Dye-Sensitized Solar Cells	127
7.1 Introduction	128
7.2 Methodology	129
7.3 Results	131
7.3.1 Initial Optimization	131
7.3.2 Developing a Better Objective Function	134
7.4 Conclusions	137
References	138
Appendix A. Consistency Conditions for TF/SF	A-1
Appendix B. Curriculum Vita	B-1

## List of Figures

1.1	a) Description of the field intensity perpendicular to the surface. b) Schematic illustrating SPP excitations	31
1.2	Schematic illustrating LSPR resonances. The blue circle represents the electron cloud while the yellow circle is the metal nucleus background.	32
1.3	Field lines describing the inter-particle coupling for nanoparticles coupled a) longitudinally and b) transversely relative to the incident polarization.	33
2.1	Unit cell for FDTD calculations. The electric field components are located on the edges of the cell and represented by red triangles (component of the field is in the direction of the longer dimension). The magnetic field components are stored on the faces of the cell and represented by blue arrows (component represented by the direction of the arrow).	40
2.2	Schematic showing the coupling between each incident field grid.	54
2.3	Flow chart illustrating the time stepping of the FDTD method.	56
3.1	The absorption cross-section of a single CdSe 610 nm (red) and PbS 850 nm (blue) quantum dot using the single Lorentzian model.	61
3.2	The cell diagram for the nanoislands (gold ellipses) coupled to the quantum dots (green filled in circle). The absorption, scattering and quantum dot	

absorption are calculated on the surfaces defined by the labeled blue boxes. The incident Gaussian plane wave is introduced from the TF/SF region defined by the red box. The cell is surrounded by a convolution perfectly matched layer to act as absorbing boundary conditions.

62

3.3 a) Experimental extinction of the random Au nanoparticles. b) Theoretical absorption cross-section of the gold nanoisland surfaces as approximated by the monomer, symmetric dimer, and asymmetric dimer models. c) An illustration of the depicted models with the box color corresponding to the line color in part b

64

3.4 a) Absorption spectra of a 200 nm long, 11 nm high gold nanoellipse monomer and symmetric dimer. b) Map of the  $H_z$  field for the symmetric dimer under a constant wavelength excitation centered at i) 658 nm and ii) 1,008 nm, and iii) a monomer excited at 862 nm.

66

3.5 Absorption spectra of a symmetric trimer and dimer model of the nanoisland films with a 7 and 10 nm gap. For the trimers the gap between all nanoellipses are the same.

66

3.6 Simulated absorption cross-section of gold nanoellipse dimers with a gap size of 7 nm with PbS 850 nm or CdSe 610 nm quantum dots in the hot spot.

67

3.7 a) Absorption cross sections calculated directly, represented by the solid curves compared with results determined from the difference between the gold nanoisland absorption with and without quantum dots. The subscripts

correspond to the gap size. b) Absorption enhancement for CdSe 610 nm and PbS 850 nm quantum dots inside a hot-spot of the nanodimer for a 7 nm and a 10 nm gap.

68

- 3.8 a) An approximation to the plasmonic loss into the 40 nm (a and c) and 110 nm (b and d) long dimers coupled to both the CdSe 610 nm QD (a and b) and PbS 850 nm QD (c and d) inside a 10 nm gap. The orange and green lines are the quantum dot absorption while the red and blue lines are the difference between the gold nanoislands with and without the quantum dots. The purple lines represent the approximate change in the gold nanoislands absorption cross-section. 70
- 3.9 An illustration of the density based nanoisland system. The red “X” corresponds to an invalid quantum dot position. 71
- 3.10 A scatterplot showing the simulated change in a) peak wavelength and b) peak height shift with changing quantum dot density. Triangles are from the peak location/value of the mean spectra, and circles are the mean of the peak location/value for all calculations. 72
- 3.11 Convergence of the density calculations for the CdSe 610 nm QD (a and b) and the PbS 850 nm QD (c and d). The legends are in QDs/100 nm. 73
- 3.12 Experimental light extinction from the random Au-NPs with different density of a) CdSe 610 nm QDs and b) PbS 850 nm QDs. Solid curves correspond to the smoothed absorption spectra using a Savitzky-Golay filter, dashed curves are a sixth degree polynomial fit used to extract the

peak position (marked with a circle) accurately. Scatter plot showing the change in c) red-shift and d) peak extinction against change in CdSe (red and orange) or PbS (blue and green) quantum dot solution exposure time. Triangles are at the maximum of the smoothed spectra; circles are at the maximum of the polynomial fits. The errors of the data are estimated to be less than 4%.

74

- 4.1 Schematic of the test cell. The red box is the TFSF boundary, the green circle is the emitters, and the inset represents the electronic structure of the emitters 80
- 4.2 (a) Scattering intensity at different emitter densities, with  $\gamma_p = 1 \times 10^{13}$   
 (b) Scattering intensity at different dephasing rates with  $n_e = 1 \times 10^{26}$   
 (c) Scattering Intensity of the high frequency resonance as a function of density on a double log scale 82
- 4.3 (a) Diagram of the emitter coated Ag nanoparticle cell. The red box is the TFSF boundary, the pink coating is the emitter layer, the silver is the silver nanoparticle, (b) Scattering Intensity for the QE coated NP, with the inset showing the particle (c) Scattering Intensity for the QE coated with a 2 nm  $\text{TiO}_2$  layer between the silver and QE layer. The inset shows the particle structure with the green layer representing the  $\text{TiO}_2$ . 83
- 4.4 The distribution of quantum emitters in the system 84
- 4.5 A comparison of the a) analytical and b) numerical photon echo of the inhomogeneously broadened quantum dots. The  $x$ -axis is a normalized

time unit, the  $y$ -axis is the area under the first pulse ( $\Omega_1 \tau_p$ ) and the map corresponds to the value of  $\rho_{01}$  or the off diagonal density matrix element. 85

- 5.1 Unit cell for FDTD calculations including oriented dipole moments. The electric field components are located on the edges of the cell and represented by red triangles (the component of the field is in the direction of the longer dimension). The magnetic field components are stored on the faces of the cell and represented by blue arrows (the component represented by the direction of the arrow). The pink circles represent the molecular dipoles and all three components are individually stored there. 91
- 5.2 Schematic showing how  $\mu_1$  is calculated from the surface normal of a nanoparticle. 92
- 5.3 a) Extinction spectrum of a silver truncated tetrahedron with a perpendicular bisector of 90 nm and a height of 55 nm, with and without a 2 nm coating of a constant dielectric material with a relative permittivity of 1.2. Inset shows a schematic of the uncoated tetrahedron b) LSPR red-shift caused by the molecular coating vs. the energy of the molecular excitation. The horizontal dashed line is the red-shift caused by the constant dielectric coating and the vertical line is the energy of the plasmon resonance of the tetrahedron, coated with the constant dielectric layer. 93
- 5.4 Cell diagram for the calculation in the a)  $xy$ - and b)  $xz$ - planes. The green ball represents the quantum dot, the blue arc is the molecular layer, and the gold ellipses are the nanoparticles. The system is excited from above by a

TF/SF surface (red), and the absorption and scattering fluxes are calculated over a box 6 nm inside and outside the TF/SF surface respectively. The cell has 50 unit cell thick PML regions at the boundary.

95

- 5.5 a) The absorption spectra of i) normally and ii) tangentially oriented molecules relative to the gold nanoellipsoid surfaces. The molecular resonances are on ( $\lambda_0 = 588$  nm) and off-resonance ( $\lambda_0 = 300$  nm) with the LSPR. b) Peak shifts (blue squares and circles) and maximum extinction cross-sections (red triangles) of the coated nanoellipsoid dimers with varying degrees of alignment to the surface normal. Insets illustrate the orientation of the molecules relative to the nanoparticle surface.
- 97
- 5.6 a) The extinction cross-section of gold nanoellipsoid dimers ( $x$ -axis is the inter-particle axis) coated with a molecular monolayer with an excitation at 300 nm and a transition dipole moment of 2.5 D oriented i) normally and ii) tangentially with molecular densities  $10^{25}$  and  $10^{26} \frac{\text{molecules}}{\text{m}^3}$ . b) Peak shifts (blue squares) and maximum extinction cross-sections (red triangles) of the coated nanoellipsoid dimers with varying degrees of alignment to the surface normal. Inset schematics demonstrate the dipole orientation (blue arrow) relative to the surface.
- 99
- 5.7 a) Extinction cross-section of the bare nanoellipsoid dimers with and without a quantum dot in the hot-spot. b) The difference between the extinction cross-section of the dimers coupled and uncoupled to the quantum dot. c) The peak shift (blue squares) and change in extinction cross-section (red triangles) for dimers coated with a molecular monolayer

for different molecular densities reported in  $\frac{\text{molecules}}{\text{m}^3}$ . The dashed lines correspond to the bare gold nanoellipsoid dimers' peak shift (short dashes and blue) and change in peak extinction (long dashes and red) d) The change of oscillator strength for dimers coated with a molecular monolayer for different molecular densities normalized to the integral without coupling to a quantum dot. The dashed line is the change of the integral for the bare gold nanodimer. The inset schematic demonstrates the dipole orientation (blue arrow) relative to the surface.

100

## 5.8

Effects of coating gold nanoellipsoids with a molecular layer that has an excitation wavelength of 588 nm and a transition dipole moment of 2.5 D oriented at different angles,  $\theta$ , from the surface normal. a) i) Peak shift (blue squares) and maximum extinction cross-section (red triangles) of the coated nanoellipsoid dimers. ii) The peak shift (blue squares) and change in extinction cross-section (red triangles) caused by coupling to a CdSe 610 nm quantum dot. The dashed lines correspond to the bare gold nanoellipsoid dimer's peak shift (short dashes and blue) and change in peak extinction (long dashes and red) b) The change of oscillator strength upon the addition of the quantum dot for dimers. The values are normalized to the integral without coupling to a quantum dot. The dashed line is the change of the integral for the bare gold nanodimer. Inset schematic demonstrates the dipole orientation (blue arrow) relative to the surface.

102

- 6.1 Schematic illustration of the FDTD unit cell for chiral materials. The blue arrows represent the magnetic field components, the red triangles represent the electric field components, the pink circles are the location of the dipole moments needed to calculate  $\mathbf{P}_{\text{Molecule}}$ , and the light blue square represent the locations of the dipole moments needed to calculate  $\mathbf{M}_{\text{Molecule}}$ . 110
- 6.2 Schematic showing how  $\boldsymbol{\mu}_c$  (blue) and  $\mathbf{m}_c$  (red) are calculated from the surface normal of the nanoparticle. a) The real system and b) the approximated molecular resonance 111
- 6.3 a) Illustration of normally, longitudinally, and latitudinally oriented dipoles on a gold sphere. b) The extinction cross-section of a 40 nm gold sphere. c) The CD spectrum for the 5 nm chiral shell coating the spheres. 112
- 6.4 Cell map for the sphere in the a)  $yz$ - and b)  $xy$ - planes. The gold circle represents the gold nanospheres. The blue shell is the 5 nm chiral shell. The blue boxes represent the absorption and scattering flux regions. The system is excited from a TF/SF surface (red box) along either the longitudinal axis (dark red arrows), latitudinal axis (red arrows), or the diagonal (pink arrows) with a pulse centered at 333 nm, and a width of 1.67 fs. The cell has 20 unit cell thick CPML regions at the boundary. 113
- 6.5 CD spectra of gold spheres coated with a 5 nm layer of chiral molecules treated isotropically, oriented along the surface normal, and oriented along the tangential vectors excited by a plane wave with a  $\mathbf{k}$  of a)  $\mathbf{k} = \left[\frac{2\pi}{\lambda}, 0, 0\right]$ , b)  $\mathbf{k} = \left[0, 0, \frac{2\pi}{\lambda}\right]$ , c)  $\mathbf{k} = \left[\frac{2\pi}{\lambda\sqrt{3}}, \frac{2\pi}{\lambda\sqrt{3}}, \frac{2\pi}{\lambda\sqrt{3}}\right]$ . 115

- 6.6 a) Illustration of the tangential dipole moments oriented at an azimuthal angle of  $45^\circ$  (red) and  $135^\circ$  (green) relative to the surface normal (perspective down the latitudinal axis). b) CD spectra of the gold sphere coated with a i) chiral and an ii) achiral molecular monolayer with a tangential orientation and an azimuthal angle of  $45^\circ$  (red, solid) and  $135^\circ$  (green, dashed) propagated along the latitudinal, longitudinal, and diagonal axes 116
- 6.7 Cell map of the FDTD cell used to model the nanocross array in the a)  $xz$ - and b)  $xy$ - planes. The c) absorbance and d) CD spectra of an 875 nm thick film of FMN molecules. 117
- 6.8 a) Absorbance spectra for the gold nanocross array coated with a layer of FMN molecules of different thicknesses b) Anisotropy factor spectra for the gold nanocross array coated with a layer of FMN molecules of different thicknesses c) Anisotropy factor at 650 nm against the thickness of the FMN films. 119
- 6.9 a-b) Cell map of the partially oriented molecular films in the a)  $xz$ - and b)  $xy$ - planes. The dark green crosses represent the oriented dipole regions. c-d) Anisotropy factor spectra for the gold nanocross array coated with a 50 nm oriented dipole FMN film: c) without and d) with a 220 nm isotropic layer above it. 121
- 6.10 Cell diagram for the calculation in the a)  $xy$ - and b)  $xz$ - planes. The green ball represents the quantum dot, the blue arc is the molecular layer, and the gold ellipses are the nanoparticles. The system is excited from above by a

TF/SF surface (red), and the absorption and scattering fluxes are calculated over a box 6 nm inside and outside the TF/SF surface, respectively. The cell has 20 unit cells thick PML regions at the boundary. 123

6.11 a) Extinction cross-section of the molecularly coated nanoellipsoid dimers coupled and uncoupled to a quantum dot in the center of the gap b) The extinction cross-section of the dimers coated with chiral molecules coupled to a quantum dot with and without the quantum dot also coated with the molecular layer. 124

7.1 (a) Schematic of the computational cell, (b) Fitness surface as generated by a grid search 131

7.2 The results of applying the GA to an interpolated fitness surface for the a) the convergence of a representative run for the GA with the uniform distribution mutation operator, where best is the best individual in a generation and Avg is the average individual in the population b) The best (white circles) and average (black circles) solutions plotted on the fitness surface for GA with the uniform distribution mutation operator c) the convergence of a representative run of the GA with the normal distribution mutation operator, where best is the best individual in a generation and Avg is the average individual in the population d) The best (white circles) and average (black circles) solutions plotted on the fitness surface for GA with the normal distribution mutation operator 133

- 7.3 a) Diagram of the new FDTD cell for the objective function. The silver sphere in the center is the silver nanoparticle with a variable radius. The green circles with a blue border represent the coated  $\text{TiO}_2$  nanoparticles separated by 5 nm from the silver nanoparticle. The absorption of the photoanode is approximated by adding the two flux regions (blue dashed line) with positive flux pointing towards the coated nanoparticles. The cell is excited from a plane wave generated from the TF/SF surface and the cell uses CPMLs as the boundary conditions. b) Absorption cross-section for the molecularly coated  $\text{TiO}_2$  nanoparticle. 134
- 7.4 a) Absorption cross-section of the total system subtracted by the absorption cross-section of the silver nanoparticle. b) Absorption cross-section of the total system for silver nanoparticles with a radius of 10, 20, 30, and 40 nm. 135
- 7.5 a) Fitness of the nanoparticles against the radius. b) The fitness of the nanoparticles divided by the area of the circles. 136

## CHAPTER 1

### Introduction

#### 1.1 Optics of Metal Nanoparticles

The optical properties of metal nanostructures are well described with classical electrodynamics methods.<sup>1</sup> The energy level spacing of metal nanoparticles larger than a few nanometers is sufficiently smaller than thermal energy, such that their energy structure can be treated as a continuum.<sup>2</sup> Despite the small level spacings, the optical properties of the nanoparticles are still highly dependent on the frequency of excitation. At long wavelengths the skin depth of the metal is almost zero making the nanoparticles perfect electric conductors, and therefore perfect reflectors.<sup>2</sup> As the frequency increases, so does the skin depth, intensifying the dissipation induced by the nanoparticles.<sup>2</sup> Finally as the light frequency approaches the plasma frequency of the metal, the particles act as a dielectric media with the inter-band transitions controlling their light attenuation.<sup>2</sup> All of these interactions are described by the metal's complex dielectric function,  $\epsilon$ , in conjunction with Maxwell's equations.<sup>2</sup>

##### 1.1.1 Maxwell's Equations

The optical properties of the metal nanostructures are calculated classically using Maxwell's equations,

$$(1.1a) \quad \nabla \cdot \mathbf{D} = \rho_{ext}$$

$$(1.1b) \quad \nabla \cdot \mathbf{B} = 0$$

$$(1.1c) \quad \nabla \times \mathbf{H} = \frac{\partial \mathbf{D}}{\partial t} + \mathbf{J}_{\text{ext}}$$

$$(1.1d) \quad -\nabla \times \mathbf{E} = \frac{\partial \mathbf{B}}{\partial t} + \mathbf{M}_{\text{ext}}$$

where  $\rho_{\text{ext}}$  is the external charge density,  $\mathbf{E}$  and  $\mathbf{H}$  are the electric and magnetic fields,  $\mathbf{D}$  and  $\mathbf{B}$  are the electric and magnetic flux densities, and  $\mathbf{J}_{\text{ext}}$  and  $\mathbf{M}_{\text{ext}}$  are the external electric and magnetic current densities.<sup>3</sup> For optical problems there is typically no external charge density, so  $\rho_{\text{ext}}$  is set to zero and Maxwell's equations reduce to only Ampere's (Equation 1.1c) and Faraday's (Equation 1.1d) Law<sup>2</sup>

$$(1.2a) \quad \nabla \times \mathbf{H} = \frac{\partial \mathbf{D}}{\partial t} + \mathbf{J}_{\text{ext}}$$

$$(1.2b) \quad -\nabla \times \mathbf{E} = \frac{\partial \mathbf{B}}{\partial t} + \mathbf{M}_{\text{ext}}.$$

The electric and magnetic fields are related to their respective flux densities via the constitutive relations, which for achiral, isotropic media are defined as

$$(1.3a) \quad \mathbf{D} = \epsilon_{\infty} \mathbf{E} + \mathbf{P},$$

$$(1.3b) \quad \mathbf{B} = \mu_{\infty} \mathbf{H} + \mathbf{M},$$

where  $\epsilon_{\infty}$  is the high frequency dielectric constant,  $\mu_{\infty}$  is the high frequency permeability,  $\mathbf{P}$  is the polarization density, and  $\mathbf{M}$  is the magnetization density of the media.<sup>2</sup>  $\mathbf{P}$  and  $\mathbf{M}$  represent the strength of electric and magnetic dipole moments per unit volume and are related to the internal electric and magnetic current densities by,

$$(1.4a) \quad \mathbf{J}_{\text{int}} = \frac{\partial \mathbf{P}}{\partial t}$$

$$(1.4b) \quad \mathbf{M}_{\text{int}} = \frac{\partial \mathbf{M}}{\partial t}.$$

The electric susceptibility,  $\chi_e$ , and magnetic susceptibility,  $\chi_m$ , of the media are defined as

$$(1.5a) \quad \chi_e = \epsilon - \epsilon_\infty$$

$$(1.5b) \quad \chi_m = \mu - \mu_\infty,$$

and they control the excitation of  $\mathbf{P}$  and  $\mathbf{M}$ , by  $\mathbf{E}$  and  $\mathbf{H}$  via<sup>2</sup>

$$(1.6a) \quad \mathbf{P} = \epsilon_0 \chi_e \mathbf{E}$$

$$(1.6b) \quad \mathbf{M} = \mu_0 \chi_m \mathbf{H}.$$

Substituting Equations 1.5 and 1.6 into Equation 1.3 leads to the following recasting of the constitutive relations

$$(1.7a) \quad \mathbf{D} = \epsilon \mathbf{E},$$

$$(1.7b) \quad \mathbf{B} = \mu \mathbf{H}.$$

### 1.1.2 Dielectric Response of a Free Electron Gas

The metals are assumed to be magnetically inactive, so  $\chi_m$  is assumed to be zero. The electric susceptibility of metal nanoparticles can be approximated by the plasma model, treating the electron cloud as a free electron gas over a positive point charge array.<sup>2</sup> In this model the motion of the electrons is described by

$$(1.8) \quad m_e \ddot{\mathbf{x}} + m_e \gamma \dot{\mathbf{x}} = -e \mathbf{E}(t),$$

where  $\gamma = \frac{1}{\tau}$  is the collision frequency,  $\tau$  is the relaxation time of the free electron gas,  $m_e$  is the mass of an electron,  $e$  is the elementary charge, and  $\mathbf{x}$  is the displacement of the electron.<sup>2</sup> Assuming a time harmonic driving field,  $\mathbf{E}(t) = \mathbf{E}_0 e^{-i\omega t}$ , where  $\omega$  is the angular frequency of light, Equation 1.8 can be solved by

$$(1.9) \quad \mathbf{x}(t) = \frac{e}{m_e(\omega^2 + i\gamma\omega)} \mathbf{E}_0 e^{-i\omega t}.$$

The displacement of electrons can be used to calculate  $\mathbf{P}$  via,

$$(1.10) \quad \mathbf{P} = n_e e \mathbf{x},$$

where  $n_e$  is the number density of the electrons.<sup>2</sup> Substituting Equation 1.10 into Equation 1.3a and comparing the result with Equation 1.7a, the dielectric function for the free electron gas model is obtained

$$(1.11) \quad \epsilon_D = \epsilon_0 \left( \epsilon_\infty - \frac{\sigma_D \omega_p^2}{\omega^2 - i\gamma\omega} \right),$$

where  $\sigma_D$  is the oscillator strength of the resonance and  $\omega_p = \sqrt{\frac{n_e e^2}{m_e \epsilon_0}}$  is the plasma frequency of the metal.<sup>2</sup> Due to the similarity with the AC conductivity of metals this dielectric function is known as the Drude dielectric function.<sup>2</sup>

### 1.1.3 The Effects of Inter-Band Transitions

At higher frequencies, the Drude model disagrees with real metallic dielectric functions because of inter-band transitions.<sup>2</sup> For gold and silver the onset of the disagreements occurs in the visible range making the Drude model inadequate for describing the plasmonic properties of noble metal nanoparticles.<sup>2</sup> The Lorentz oscillator model is used to replicate an inter-band

transition, which modifies Equation 1.8 to include the resonant frequency of the transition,  $\omega_L$ ,

$$(1.12) \quad m_e \ddot{\mathbf{x}} + m_e \gamma_L \dot{\mathbf{x}} + m_e \omega_L^2 \mathbf{x} = -e\mathbf{E}.$$

Following the same procedure as the Drude model the Lorentzian dielectric function can be defined as

$$(1.13) \quad \epsilon_L = \epsilon_0 \left( \epsilon_\infty + \frac{\sigma_L \omega_L^2}{\omega_L^2 - \omega^2 + i\gamma_L \omega} \right),$$

where  $\sigma_L$  is the oscillator strength scaled by  $\left(\frac{\omega_p}{\omega_L}\right)^2$ .<sup>2</sup> Combining the free electron oscillation with all inter-band transitions leads to the following Lorentz-Drude approximation to metallic dielectric functions

$$(1.14) \quad \epsilon_{LD} = \epsilon_0 \left( \epsilon_\infty - \frac{\sigma_D \omega_p^2}{\omega^2 - i\gamma\omega} + \sum_{L=1}^{n_{Lor}} \frac{\sigma_L \omega_L^2}{\omega_L^2 - \omega^2 + i\gamma_L \omega} \right),$$

where  $n_{Lor}$  is the number of inter-band transition of the metal.<sup>2</sup> The parameters for  $\epsilon_{LD}$  are taken from Rakic et al.<sup>4</sup> and McMahon et al.<sup>5</sup>

## 1.2 Surface Plasmon Resonance

Surface plasmon resonances (SPRs) are coherent, light induced oscillations of conduction band electrons at interfaces between negative and positive permittivity materials.<sup>2</sup> Typically the negative dielectric material is metallic, but recently some ceramic materials have also been shown to have plasmonic properties.<sup>6,7</sup> By converting electromagnetic energy to electro-mechanical energy SPRs can confine light below the diffraction limit

$$(1.15) \quad d \geq \frac{\lambda}{2n \sin \theta}$$

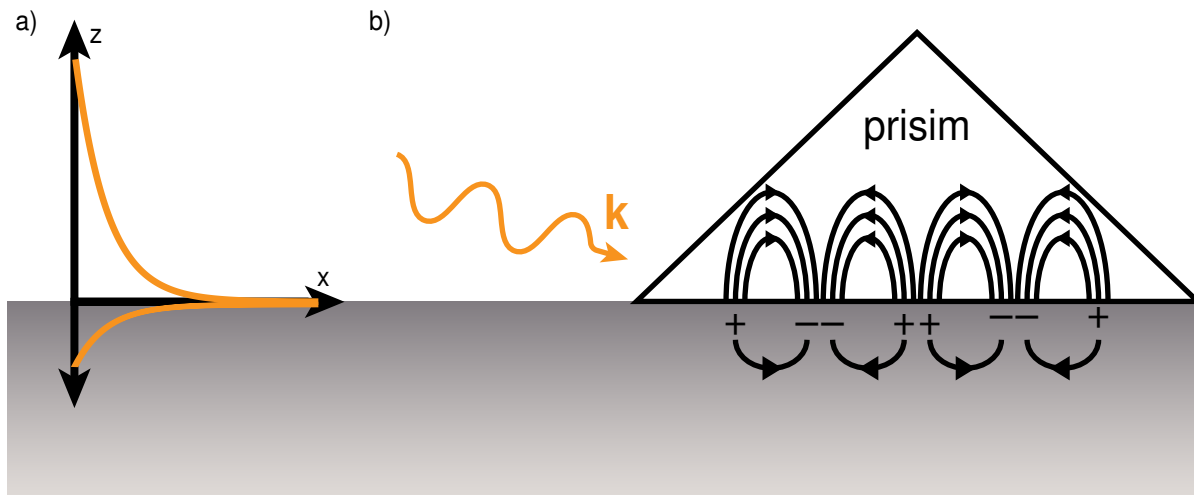


Figure 1.1. a) Description of the field intensity perpendicular to the surface. b) Schematic illustrating SPP excitations

where  $n$  is the index of refraction,  $\lambda$  is the wavelength of light,  $d$  is the size of the structures, and  $\theta$  is the angle of incidence.<sup>2</sup> Depending on the surface geometry SPRs can be either a surface plasmon polariton (SPP) or a local surface plasmon resonance (LSPR).

### 1.2.1 Surface Plasmon Polaritons

SPPs are propagating electromagnetic excitations occurring at metal-dielectric interfaces, as illustrated in Figure 1.1.<sup>2</sup> In SPPs the SPR is coupled to an evanescent electromagnetic wave in the dielectric material, which has subwavelength confinement perpendicular to the surface.<sup>2</sup> An SPP will continue to propagate until the energy of the resonance decays through either absorption in the metal or scattering.<sup>2</sup> For photons to excite SPPs both their energy and momentum has to match the plasmon resonance.<sup>2</sup> Because of the momentum matching restriction, SPPs cannot be directly excited, but their excitation requires either a prism, grating, or surface defect.<sup>2</sup>

### 1.2.2 Local Surface Plasmon Resonance

LSPRs are the second type of SPRs that occur on the surface of particles significantly smaller than the wavelength of light.<sup>2</sup> Unlike SPPs, LSPRs can be directly excited because

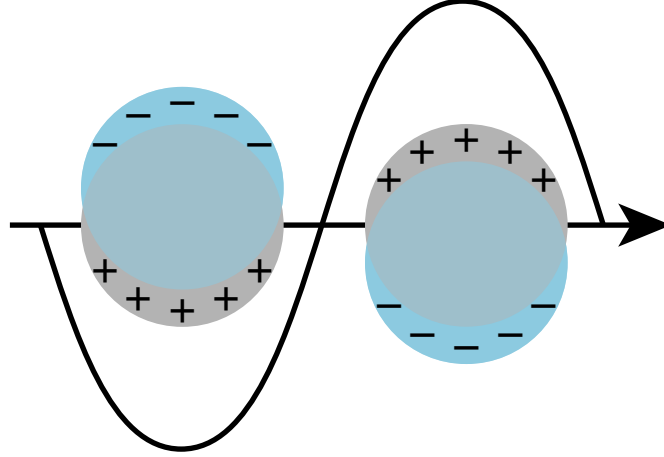


Figure 1.2. Schematic illustrating LSPR resonances. The blue circle represents the electron cloud while the yellow circle is the metal nucleus background.

the metal surface provides the restoring force for the oscillator, as illustrated in Figure 1.2.<sup>2</sup> The electron oscillations generate intense electric fields on the surface of the nanoparticles, which decay exponentially from the surface.<sup>2</sup> The polarizability,  $\alpha$ , of a sphere of radius,  $a$ , in the quasi-static limit gives a qualitative understanding of the excitation of LSPRs,

$$(1.16) \quad \alpha = 4\pi a \frac{\varepsilon - \varepsilon_m}{\varepsilon + 2\varepsilon_m},$$

where  $\varepsilon$  is the dielectric function of the metal and  $\varepsilon_m$  is the dielectric constant of the media.<sup>2</sup> From Equation 1.16 the Fröhlich condition for LSPR excitation can be obtained,<sup>2</sup>

$$(1.17) \quad \text{Re}[\varepsilon(\omega)] = -2\varepsilon_m.$$

A key feature of LSPRs is their highly tunable plasmon resonances. Because the surface geometry provides the restoring force for the resonance, minor changes in the size, shape or

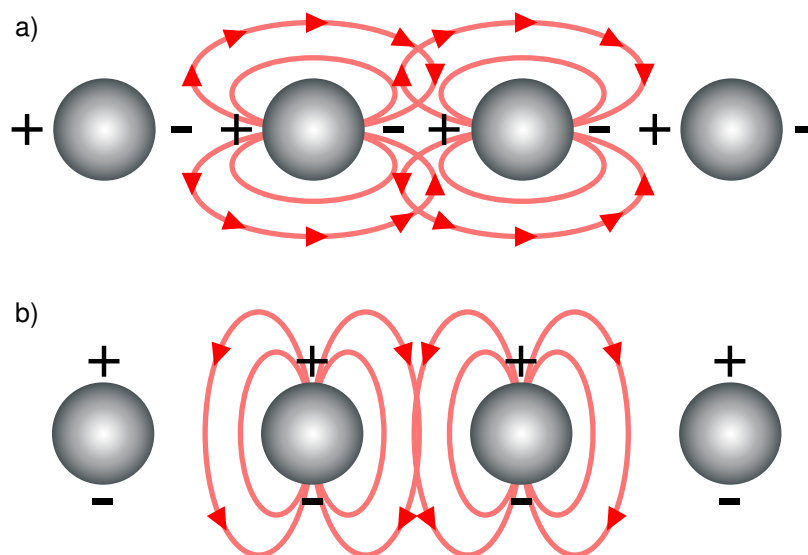


Figure 1.3. Field lines describing the inter-particle coupling for nanoparticles coupled a) longitudinally and b) transversely relative to the incident polarization.

dielectric environment of the nanoparticles lead to significant changes in their plasmon resonance. Work by Kuwata et al.<sup>8</sup> and Kelley et al.<sup>9</sup> demonstrated the effects of the size and shape of nanoparticles on their LSPR. The LSPRs are affected by not only the dielectric constant of the embedded media but also the degree of inter-particle coupling. The shift induced by the coupling is dependent on the overlap between the plasmonic fields, with a longitudinal coupling leading to a red-shift and transverse coupling leading to a blue-shift as illustrated in Figure 1.3.<sup>2</sup>

### 1.3 Applications

The tunability of plasmon resonances and their ability to confine light makes them attractive for many applications in optics and nanophotonics. Recently plasmonic nanowire waveguides have garnered significant interest because of their ability to support deep-subwavelength propagation of light.<sup>10,11</sup> Optical signals provide significantly higher data transfer rates than

electronic signals, so incorporating optical components in nanoscale circuits would greatly improve device performance.<sup>12</sup> Currently the diffraction limit hinders the general applicability of optical components in circuitry by preventing their miniaturization.<sup>12</sup> Plasmonic waveguides confine light to metal dielectric interfaces, allowing for the miniaturization of these components.<sup>10</sup> While these waveguides have to overcome ohmic losses from their absorption at the LSPR frequency, they remain the only convenient technique for deep-subwavelength confinement of optical signals.<sup>12</sup>

Plasmonic nanostructures also provide the means to create new materials with novel optical properties. Plasmonic metamaterials mimic natural crystal lattices, but with plasmonically active components acting as the atoms.<sup>13</sup> These lattices have useful optical properties not seen in natural systems such as a negative refractive index, perfectly matched absorption, and super chiral light generation.<sup>13–16</sup> Using these unique optical properties metamaterials can potentially develop new devices such as perfect lenses and invisibility cloaks.<sup>13</sup> Further experimental and computational investigation is necessary for the development of metamaterials with prespecified optical properties.

### **1.3.1 Plasmonic Devices**

One of the primary uses of plasmonic nanoparticles is as antennae for optical devices. By focusing light on optically active materials in the devices, plasmonic nanoparticles can significantly increase their performance. These principles have been used to improve solar cells,<sup>17–20</sup> light emitting diodes,<sup>21–23</sup> and light sensors.<sup>24–27</sup> Plasmonic nanostructures can also be used as scattering centers in solar cells, increasing the optical path length in the cell.<sup>28–30</sup> Coupling nanostructures to gain material has also led to the development of the first nanolasers, a key component for optical circuitry.<sup>31,32</sup>

A second class of devices uses the sensitivity of the plasmon resonance to the dielectric environment as a chemical sensing platform. Equation 1.16 demonstrates that the location of the plasmon resonance is partially controlled by the dielectric constant of the embedded media. As the index of refraction of the background medium increases, the plasmon resonance red-shifts allowing for the detection of chemical and biomolecular species.<sup>33-35</sup> Utilizing this technique the van Duyne lab was able to develop a system capable of detecting amyloid-derived diffusible ligands, a neurotoxin associated with Alzheimer's disease, at 100 fM concentrations.<sup>35</sup> The sensors are even able to detect molecular level changes in the environment because of the exponential decay of the plasmonic fields.<sup>34</sup> Utilizing chiral nanostructures and plasmonic field enhancement can also generate superchiral light, which can be further developed to detect the handedness of a single chiral molecule.<sup>16</sup>

### 1.3.2 Raman Spectroscopy

One of the more successful applications of plasmonic structures is the enhancement of spectroscopic signals. The use of plasmonic enhancement has particularly focused on non-linear spectroscopy techniques such as Raman spectroscopy, where the spectral cross-section is typically small. Surface enhanced Raman spectroscopy (SERS) is one of the two commonly used plasmonically enhanced Raman spectroscopy techniques.<sup>36,37</sup> SERS utilizes rough metal nanosurfaces to generate electromagnetic hot-spots that intensify both the incident and scattered electric fields by several orders of magnitude. While it has been successful in measuring molecular Raman spectra at the few or single molecule level, generating consistent substrates and uniform hot-spot distributions remains a challenge. The second approach known as tip-enhanced Raman spectroscopy (TERS) controls the location of the hot-spot by using either a plasmonically active atomic force microscope or scanning tunneling microscope tip to scan a

molecular layer adsorbed to a substrate.<sup>38–42</sup> This technique is capable of simultaneously imaging a surface and tracking chemical changes of a molecular layer adsorbed on it.<sup>43</sup> The mechanism of TERS is still not fully understood and active research is trying to better understand the process.<sup>42,43</sup>

#### 1.4 Coupling Between Plasmons and Quantum Emitters

Understanding the coupling between metal nanoparticles and quantum emitters is vital for predicting the performance of many plasmonic devices.<sup>44–51</sup> As the coupling strength changes, different optical processes become dominant, changing the spectroscopic signature. At low coupling strength, the plasmonic nanoparticles simply enhance the optical processes of the quantum emitters, with separate plasmonic and emitter modes.<sup>45,52</sup> As the coupling strengthens a dip begins to appear in the system's absorption spectra at the molecular resonance due to dipole induced exciton transparency.<sup>45,52</sup> As the coupling continues to increase the absorption continues to decrease, until the mode splits, with both resulting modes having partial molecular and plasmonic character.<sup>45,52</sup> Recent developments demonstrated the ability to actively control the coupling between the nanoparticles and quantum emitters creating the potential for all-optical switching.<sup>53</sup>

Modeling the coupling between quantum emitters and metal nanoparticles has traditionally occurred through classical, isotropic dielectric models.<sup>45,46,51</sup> These models fail to address the importance of molecular orientation on the coupling, and can only qualitatively approximate experiments.<sup>45</sup> While work has been done treating the molecular layer anisotropically or quantum mechanically, those approaches are only valid for either idealized systems or single molecular dipole moments.<sup>54–57</sup> Semiclassical methods such as the Maxwell-Liouville (ML) method can incorporate both anisotropic and quantum mechanical effects, but they greatly increase the

computational cost of the calculations.<sup>58-61</sup> Developing classical approaches to model the coupling between anisotropic quantum emitters and metal nanoparticles will provide fundamental insights into the future development of devices.

## 1.5 Dissertation Overview

The rest of this dissertation will focus on developing classical and semiclassical methods for understanding the coupling between metal nanoparticles and quantum emitters within a finite-difference time-domain (FDTD) framework. FDTD was chosen to allow for the methodology to be applied to an arbitrary nanoparticle-quantum emitter system and excitation profile. Chapter 2 provides an overview of FDTD and the algorithms implemented for all calculations in this dissertation. Chapter 3 then applies a two dimensional FDTD model to a gold metal nanoisland film coupled to a colloidal quantum dot monolayer. The model averages over a set of gold nanoellipses coupled to quantum dots at varying number densities to understand the coupling between the films. A semiclassical model of a PbS 850 nm quantum dot is then developed in Chapter 4 and used to understand the effects of the short wavelength tail on the coupled spectra. Then Chapter 5 investigates the effects of molecular monolayers, including their orientation relative to the metal surface, on the plasmon resonance. Chapter 6 extends the molecular models to include chiroptical properties to study the chiral imprinting of metal nanostructures. Finally, Chapter 7 applies the molecular layer models to plasmonic nanospheres for dye-sensitized solar cell applications, with attempts to optimize the nanostructures for that application.

## CHAPTER 2

### **Modeling Classical Electrodynamics with Finite-Difference Time-Domain**

A particularly popular method for modeling classical electrodynamics is FDTD because of its flexibility in modeling a particle's geometry, and its ability to study systems across a broad frequency range. This chapter outlines the application of FDTD to solve Maxwell's equations for optical problems. It will focus on how the method propagates light, treats dispersive materials, terminates the cell, and introduces incident waves into the cell, for all work described in the dissertation.

## 2.1 Coupled Differential Equation Scheme for FDTD

Solutions to Equations 1.2 are found by expanding the curl operators and solving the six coupled differential equations for each component of  $\mathbf{E}$  and  $\mathbf{H}$ <sup>62</sup>

$$(2.1a) \quad \frac{\partial E_x}{\partial t} = \frac{1}{\epsilon} \left( \frac{\partial H_y}{\partial z} - \frac{\partial H_z}{\partial y} - J_x \right),$$

$$(2.1b) \quad \frac{\partial E_y}{\partial t} = \frac{1}{\epsilon} \left( \frac{\partial H_z}{\partial x} - \frac{\partial H_x}{\partial z} - J_y \right),$$

$$(2.1c) \quad \frac{\partial E_z}{\partial t} = \frac{1}{\epsilon} \left( \frac{\partial H_x}{\partial y} - \frac{\partial H_y}{\partial x} - J_z \right),$$

$$(2.1d) \quad \frac{\partial H_x}{\partial t} = \frac{1}{\mu} \left( \frac{\partial E_z}{\partial y} - \frac{\partial E_y}{\partial z} - M_x \right),$$

$$(2.1e) \quad \frac{\partial H_y}{\partial t} = \frac{1}{\mu} \left( \frac{\partial E_x}{\partial z} - \frac{\partial E_z}{\partial x} - M_y \right),$$

$$(2.1f) \quad \frac{\partial H_z}{\partial t} = \frac{1}{\mu} \left( \frac{\partial E_y}{\partial x} - \frac{\partial E_x}{\partial y} - M_z \right).$$

To reduce the dimensionality of the system, it is assumed to be isotropic in a direction,  $w$ , and all  $\frac{\partial}{\partial w}$  are set to zero.<sup>62</sup> The reduction will result in two uncoupled modes, which in two dimensions are called the transverse electric (TE<sub>w</sub>) and transverse magnetic (TM<sub>w</sub>), and are defined for  $w = z$  as<sup>62</sup>

TE <sub>z</sub>	TM <sub>z</sub>
$\frac{\partial E_x}{\partial t} = \frac{1}{\epsilon} \left( -\frac{\partial H_z}{\partial y} - J_x \right)$	$\frac{\partial H_x}{\partial t} = \frac{1}{\mu} \left( \frac{\partial E_z}{\partial y} - M_x \right),$
$\frac{\partial E_y}{\partial t} = \frac{1}{\epsilon} \left( \frac{\partial H_z}{\partial x} - J_y \right)$	$\frac{\partial H_y}{\partial t} = \frac{1}{\mu} \left( -\frac{\partial E_z}{\partial x} - M_y \right),$
$\frac{\partial H_z}{\partial t} = \frac{1}{\mu} \left( \frac{\partial E_y}{\partial x} - \frac{\partial E_x}{\partial y} - M_z \right)$	$\frac{\partial E_z}{\partial t} = \frac{1}{\epsilon} \left( \frac{\partial H_x}{\partial y} - \frac{\partial H_y}{\partial x} - J_z \right).$

## 2.2 The FDTD Algorithm

The FDTD algorithm, first developed by Yee in 1966,<sup>63</sup> numerically solves Equations 2.1 on a grid. It discretizes real space-time on a three dimensional grid with grid spacings of  $\Delta_x$ ,  $\Delta_y$ , and  $\Delta_z$  in the  $x$ ,  $y$ , and  $z$  directions and a time step  $\Delta_t$ . In order to be numerically stable,  $\Delta_t$  is set to a value obeying the following inequality<sup>62</sup>

$$(2.2) \quad \Delta_t \leq \frac{1}{\sqrt{\Delta_x^2 + \Delta_y^2 + \Delta_z^2}}.$$

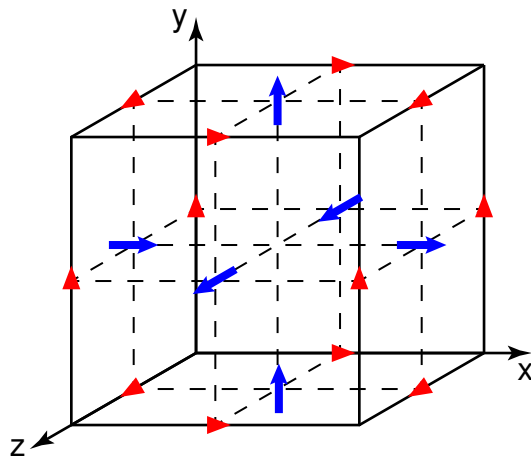


Figure 2.1. Unit cell for FDTD calculations. The electric field components are located on the edges of the cell and represented by red triangles (component of the field is in the direction of the longer dimension). The magnetic field components are stored on the faces of the cell and represented by blue arrows (component represented by the direction of the arrow).

The grid point  $(i, j, k, n)$  corresponds to the real space point  $(i\Delta_x, j\Delta_y, k\Delta_z)$  at time  $n\Delta_t$ . The following notation will be used to describe any function,  $u$ , on the grid at time  $n\Delta_t$ ,

$$u(i\Delta_x, j\Delta_y, k\Delta_z, n\Delta_t) = u_{i,j,k}^n.$$

The Yee algorithm uses central-difference operators to approximate all spatial and temporal derivatives, of a function  $u$

$$(2.3a) \quad \frac{\partial u}{\partial x}(i\Delta_x, j\Delta_y, k\Delta_z, n\Delta_t) = \frac{u_{i+\frac{1}{2},j,k}^n - u_{i-\frac{1}{2},j,k}^n}{\Delta_x} + O[(\Delta_x)^2]$$

$$(2.3b) \quad \frac{\partial u}{\partial t}(i\Delta_x, j\Delta_y, k\Delta_z, n\Delta_t) = \frac{u_{i,j,k}^{n+\frac{1}{2}} - u_{i,j,k}^{n-\frac{1}{2}}}{\Delta_t} + O[(\Delta_t)^2],$$

where  $O[(\Delta)^2]$  represents higher order corrections.<sup>62</sup> To facilitate the central-difference scheme the electro-magnetic fields are dislocated on the grid such that the operators in Equation 2.3a can be applied to all derivatives, as illustrated in Figure 2.1. To accommodate the temporal derivatives the magnetic fields are updated to times  $(n + \frac{1}{2})\Delta_t$ .<sup>62</sup>

### 2.2.1 Applying the Finite Difference Scheme to Maxwell's Equations

As an example, the update equations for  $E_x$  are generated from applying the finite difference operators to Equation 2.1a, repeated here for reference

$$\frac{\partial E_x}{\partial t} = \frac{1}{\epsilon} \left( \frac{\partial H_y}{\partial z} - \frac{\partial H_z}{\partial y} - J_x \right).$$

Applying the operators in Equation 2.3 to Equation 2.1a results in

$$(2.4) \quad \frac{E_x|_{i+\frac{1}{2},j,k}^{n+1} - E_x|_{i+\frac{1}{2},j,k}^n}{\Delta_t} = \frac{1}{\epsilon_{i+\frac{1}{2},j,k}} \left( \frac{H_y|_{i+\frac{1}{2},j,k+\frac{1}{2}}^{n+\frac{1}{2}} - H_y|_{i+\frac{1}{2},j,k-\frac{1}{2}}^{n+\frac{1}{2}}}{\Delta_z} - \frac{H_z|_{i+\frac{1}{2},j+\frac{1}{2},k}^{n+\frac{1}{2}} - H_z|_{i+\frac{1}{2},j-\frac{1}{2},k}^{n+\frac{1}{2}}}{\Delta_y} - J_x|_{i+\frac{1}{2},j,k}^{n+\frac{1}{2}} \right),$$

where  $H_y^{n+\frac{1}{2}}$ ,  $H_z^{n+\frac{1}{2}}$ ,  $E_x|_{i+\frac{1}{2},j,k}^n$ , and  $J_x|_{i+\frac{1}{2},j,k}^{n+\frac{1}{2}}$  are assumed to be stored in memory. Multiplying both sides by  $\Delta_t$ , isolating the  $E_x|_{i+\frac{1}{2},j,k}^{n+1}$  term in Equation 2.4, and repeating the procedure for all components gives the following update equations

$$(2.5a) \quad E_x|_{i+\frac{1}{2},j,k}^{n+1} = E_x|_{i+\frac{1}{2},j,k}^n + \frac{\Delta_t}{\epsilon_{i+\frac{1}{2},j,k}} \left( \frac{H_y|_{i+\frac{1}{2},j,k+\frac{1}{2}}^{n+\frac{1}{2}} - H_y|_{i+\frac{1}{2},j,k-\frac{1}{2}}^{n+\frac{1}{2}}}{\Delta_z} - \frac{H_z|_{i+\frac{1}{2},j+\frac{1}{2},k}^{n+\frac{1}{2}} - H_z|_{i+\frac{1}{2},j-\frac{1}{2},k}^{n+\frac{1}{2}}}{\Delta_y} - J_x|_{i+\frac{1}{2},j,k}^{n+\frac{1}{2}} \right),$$

$$(2.5b) \quad E_y|_{i,j+\frac{1}{2},k}^{n+1} = E_y|_{i,j+\frac{1}{2},k}^n + \frac{\Delta_t}{\epsilon_{i,j+\frac{1}{2},k}} \left( \frac{H_z|_{i+\frac{1}{2},j+\frac{1}{2},k}^{n+\frac{1}{2}} - H_z|_{i-\frac{1}{2},j-\frac{1}{2},k}^{n+\frac{1}{2}}}{\Delta_x} - \frac{H_x|_{i+\frac{1}{2},j,k+\frac{1}{2}}^{n+\frac{1}{2}} - H_x|_{i+\frac{1}{2},j,k-\frac{1}{2}}^{n+\frac{1}{2}}}{\Delta_z} - J_y|_{i,j+\frac{1}{2},k}^{n+\frac{1}{2}} \right),$$

$$(2.5c) \quad E_z|_{i,j,k+\frac{1}{2}}^{n+1} = E_z|_{i,j,k+\frac{1}{2}}^n + \frac{\Delta_t}{\epsilon_{i,j,k+\frac{1}{2}}} \left( \frac{H_x|_{i,j+\frac{1}{2},k+\frac{1}{2}}^{n+\frac{1}{2}} - H_x|_{i,j-\frac{1}{2},k+\frac{1}{2}}^{n+\frac{1}{2}}}{\Delta_y} - \frac{H_y|_{i+\frac{1}{2},j,k+\frac{1}{2}}^{n+\frac{1}{2}} - H_y|_{i-\frac{1}{2},j,k+\frac{1}{2}}^{n+\frac{1}{2}}}{\Delta_x} - J_z|_{i,j,k+\frac{1}{2}}^{n+\frac{1}{2}} \right),$$

$$(2.5d) \quad H_x|_{i,j+\frac{1}{2},k+\frac{1}{2}}^{n+\frac{1}{2}} = H_x|_{i,j+\frac{1}{2},k+\frac{1}{2}}^{n-\frac{1}{2}} + \frac{\Delta_t}{\mu_{i,j+\frac{1}{2},k+\frac{1}{2}}} \left( \frac{E_z|_{i,j+1,k+\frac{1}{2}}^n - E_z|_{i,j,k+\frac{1}{2}}^n}{\Delta_y} - \frac{E_y|_{i,j+\frac{1}{2},k+1}^n - E_y|_{i,j+\frac{1}{2},k}^n}{\Delta_z} - M_x|_{i,j+\frac{1}{2},k+\frac{1}{2}}^{n+\frac{1}{2}} \right),$$

$$(2.5e) \quad H_y|_{i+\frac{1}{2},j,k+\frac{1}{2}}^{n+\frac{1}{2}} = H_y|_{i+\frac{1}{2},j,k+\frac{1}{2}}^{n-\frac{1}{2}} + \frac{\Delta_t}{\mu_{i+\frac{1}{2},j,k+\frac{1}{2}}} \left( \frac{E_x|_{i+\frac{1}{2},j,k+1}^n - E_x|_{i+\frac{1}{2},j,k}^n}{\Delta_z} - \frac{E_z|_{i+1,j,k+\frac{1}{2}}^n - E_z|_{i,j,k+\frac{1}{2}}^n}{\Delta_x} - M_y|_{i+\frac{1}{2},j,k+\frac{1}{2}}^{n+\frac{1}{2}} \right),$$

$$(2.5f) \quad H_z|_{i+\frac{1}{2},j+\frac{1}{2},k}^{n+\frac{1}{2}} = H_z|_{i+\frac{1}{2},j+\frac{1}{2},k}^{n-\frac{1}{2}} + \frac{\Delta_t}{\mu_{i+\frac{1}{2},j+\frac{1}{2},k}} \left( \frac{E_y|_{i+1,j+\frac{1}{2},k}^n - E_y|_{i,j+\frac{1}{2},k}^n}{\Delta_x} - \frac{E_x|_{i+\frac{1}{2},j+1,k}^n - E_x|_{i+\frac{1}{2},j,k}^n}{\Delta_y} - M_z|_{i+\frac{1}{2},j+\frac{1}{2},k}^{n+\frac{1}{2}} \right).$$

### 2.3 Dispersive Materials within FDTD

Dispersive materials are included within FDTD through the auxillary differential equation (ADE) method.<sup>62,64</sup> ADE uses the constitutive relations defined in Equations 1.3 and propagates  $\mathbf{D}$ ,  $\mathbf{B}$ ,  $\mathbf{P}$ , and  $\mathbf{M}$  separately.<sup>62</sup> To update  $\mathbf{D}$  and  $\mathbf{B}$ , Equations 2.5 are used, with  $\frac{\partial \mathbf{E}}{\partial t}$  and  $\frac{\partial \mathbf{H}}{\partial t}$  replaced by  $\frac{\partial \mathbf{D}}{\partial t}$  and  $\frac{\partial \mathbf{B}}{\partial t}$ , and  $\epsilon = \epsilon_0$  and  $\mu = \mu_0$ .<sup>62</sup> The noble metals are assumed to be magnetically inactive with a dielectric function approximated by the Lorentz-Drude model (Equation 1.14). Substituting Equations 1.14 and 1.5a into Equation 1.6 and separating the individual

poles gives the definitions for  $\mathbf{P}_D$  and  $\mathbf{P}_L$  in the frequency domain as

$$(2.6a) \quad \check{\mathbf{P}}_D = \frac{\sigma_D \omega_p^2}{\omega(\omega - i\gamma_D)} \check{\mathbf{E}}$$

$$(2.6b) \quad \check{\mathbf{P}}_L = \frac{\sigma_L \omega_p^2}{\omega_L^2 - \omega^2 + i\gamma_L \omega} \check{\mathbf{E}}.$$

Then Equations 2.6 are inverse Fourier transformed to get the time domain differential equations for  $\mathbf{P}_D$  and  $\mathbf{P}_L$

$$(2.7a) \quad \left( \frac{\partial^2}{\partial t^2} + \gamma_D \frac{\partial}{\partial t} \right) \mathbf{P}_D = \sigma_D \omega_p^2 \mathbf{E}$$

$$(2.7b) \quad \left( \frac{\partial^2}{\partial t^2} + \gamma_L \frac{\partial}{\partial t} + \omega_L^2 \right) \mathbf{P}_L = \sigma_L \omega_p^2 \mathbf{E}.$$

Central difference operators are applied to Equations 2.7 resulting in the following update equations for  $\mathbf{P}_D$  and  $\mathbf{P}_L$

$$(2.8a) \quad \mathbf{P}_D|_{i,j,k}^{n+1} = \frac{2}{\gamma_D \Delta_t + 1} \mathbf{P}_D|_{i,j,k}^n + \frac{\gamma_D \Delta_t - 1}{\gamma_D \Delta_t + 1} \mathbf{P}_D|_{i,j,k}^{n-1} + \frac{\sigma_D \omega_p^2 \Delta_t^2}{\gamma_D \Delta_t + 1} \mathbf{E}|_{i,j,k}$$

$$(2.8b) \quad \mathbf{P}_L|_{i,j,k}^{n+1} = \frac{2 - \omega_L^2 \Delta_t^2}{\gamma_L \Delta_t + 1} \mathbf{P}_L|_{i,j,k}^n + \frac{\gamma_L \Delta_t - 1}{\gamma_L \Delta_t + 1} \mathbf{P}_L|_{i,j,k}^{n-1} + \frac{\sigma_L \omega_L^2 \Delta_t^2}{\gamma_L \Delta_t + 1} \mathbf{E}|_{i,j,k}.$$

## 2.4 Boundary Conditions

Modifying the boundary conditions in FDTD is necessary to increase its efficiency. The native boundary conditions in FDTD are perfect electric conductors, where all field components are set to zero at all boundaries, resulting in the perfect reflection of all outgoing waves.<sup>62</sup> If these bounds are used, then computational cells would have to be large enough to ensure that none of the reflected light interacts with the system, greatly increasing the size of the cell.

Depending on the system's symmetry either periodic boundary conditions (PBC) or perfectly matched layers (PMLs) are used.

#### 2.4.1 Periodic Boundary Conditions

Bloch PBCs are used to model systems with translational symmetry. Bloch PBCs copy the values of a function,  $u$ , from one side of the cell to the other and scales them by

$$(2.9) \quad u^n(\mathbf{r}) = \exp[-i\mathbf{k} \cdot \mathbf{x}_{\text{Bound}}] u^n(\mathbf{r} + \mathbf{x}_{\text{Bound}}),$$

where  $\mathbf{k}$  is the wavevector of the incident light,  $\mathbf{r}$  is the position of the point, and  $\mathbf{x}_{\text{Bound}}$  is the vector connecting  $\mathbf{r}$  to the reflected point on the opposite bound. If PBCs are used and  $\mathbf{k}$  is not oriented axially, then complex electric and magnetic fields are used to ensure correct scaling at the boundaries. An axial  $\mathbf{k}$  can still be treated with real valued  $\mathbf{E}$  and  $\mathbf{H}$  because  $\mathbf{k} \cdot \mathbf{x}_{\text{Bound}}$  is strictly zero or  $2\pi$ .

#### 2.4.2 Perfectly Matched Layers

PMLs are used to absorb outgoing light, approximating an infinite computational domain. This implementation of FDTD uses convolution PMLs (CPMLs),<sup>65</sup> which are an extension of the stretched-coordinate formulation of Berenger's PMLs,<sup>66,67</sup> first developed by Chew and Weedon<sup>68</sup> and independently by Rappaport.<sup>69</sup> The approach maps Maxwell's equations into a complex coordinate space,

$$\tilde{x} \rightarrow \int_0^x s_x(x') dx'; \quad \tilde{y} \rightarrow \int_0^y s_y(y') dy'; \quad \tilde{z} \rightarrow \int_0^z s_z(z') dz'.$$

Assuming  $s_w$ , where  $w = x, y, \text{ or } z$ , is a continuous function along the axial directions the  $\nabla$  operator can be defined as<sup>62</sup>

$$(2.10) \quad \nabla = \left[ \frac{1}{s_x} \frac{\partial}{\partial x}, \frac{1}{s_y} \frac{\partial}{\partial y}, \frac{1}{s_z} \frac{\partial}{\partial z} \right].$$

Using Equation 2.10 the frequency domain Maxwell's Equations inside the PMLs can be rewritten as

$$(2.11a) \quad i\omega\epsilon\check{\mathbf{E}} = \hat{x} \left( \frac{1}{s_y} \frac{\partial}{\partial y} \check{H}_z - \frac{1}{s_z} \frac{\partial}{\partial z} \check{H}_y \right) + \hat{y} \left( \frac{1}{s_z} \frac{\partial}{\partial z} \check{H}_x - \frac{1}{s_x} \frac{\partial}{\partial x} \check{H}_z \right) + \hat{z} \left( \frac{1}{s_x} \frac{\partial}{\partial x} \check{H}_y - \frac{1}{s_y} \frac{\partial}{\partial y} \check{H}_x \right)$$

$$(2.11b) \quad -i\omega\mu\check{\mathbf{H}} = \hat{x} \left( \frac{1}{s_y} \frac{\partial}{\partial y} \check{E}_z - \frac{1}{s_z} \frac{\partial}{\partial z} \check{E}_y \right) + \hat{y} \left( \frac{1}{s_z} \frac{\partial}{\partial z} \check{E}_x - \frac{1}{s_x} \frac{\partial}{\partial x} \check{E}_z \right) + \hat{z} \left( \frac{1}{s_x} \frac{\partial}{\partial x} \check{E}_y - \frac{1}{s_y} \frac{\partial}{\partial y} \check{E}_x \right).$$

Taking the inverse Fourier transform of Equations 2.11 results in the following time domain expressions

$$(2.12a) \quad \epsilon \frac{\partial}{\partial t} \mathbf{E} = \hat{x} \left( \bar{s}_y * \frac{\partial}{\partial y} H_z - \bar{s}_z * \frac{\partial}{\partial z} H_y \right) + \hat{y} \left( \bar{s}_z * \frac{\partial}{\partial z} H_x - \bar{s}_x * \frac{\partial}{\partial x} H_z \right) + \hat{z} \left( \bar{s}_x * \frac{\partial}{\partial x} H_y - \bar{s}_y * \frac{\partial}{\partial y} H_x \right)$$

$$(2.12b) \quad -\mu \frac{\partial}{\partial t} \mathbf{H} = \hat{x} \left( \bar{s}_y * \frac{\partial}{\partial y} E_z - \bar{s}_z * \frac{\partial}{\partial z} E_y \right) + \hat{y} \left( \bar{s}_z * \frac{\partial}{\partial z} E_x - \bar{s}_x * \frac{\partial}{\partial x} E_z \right) + \hat{z} \left( \bar{s}_x * \frac{\partial}{\partial x} E_y - \bar{s}_y * \frac{\partial}{\partial y} E_x \right),$$

where  $\bar{s}_x$ ,  $\bar{s}_y$ , and  $\bar{s}_z$  are the respective inverse Fourier transforms of  $\frac{1}{s_x}$ ,  $\frac{1}{s_y}$ , and  $\frac{1}{s_z}$  and  $*$  is the convolution operator.<sup>62</sup> It is assumed  $s_w$  has the form of

$$(2.13) \quad s_w = \kappa_w + \frac{\sigma_w}{a_w + i\omega\varepsilon},$$

where  $\sigma_w$  is the electric conductivity or magnetic loss in the  $w$  direction,  $a_w$  is a pole shift term to remove the singularity at  $\omega = 0$ , and  $\kappa_w$  affects the attenuation of the incident waves. Taking the inverse Fourier transform of  $s_w$  results in an expression for  $\bar{s}_w$

$$(2.14) \quad \bar{s}_w = \frac{\delta(t)}{\kappa_w} - \frac{\sigma_w}{\varepsilon\kappa_w^2} e^{-(\frac{\sigma_w}{\varepsilon\kappa_w} + \frac{a_w}{\varepsilon})t} u(t) \equiv \frac{\delta(t)}{\kappa_w} + \zeta(t)$$

where  $\delta(t)$  is the impulse function and  $u(t)$  is the unit step function. Substituting Equation 2.14 into Equation 2.12 results in a set of coupled update equations,

$$(2.15a) \quad \begin{aligned} \varepsilon \frac{\partial}{\partial t} \mathbf{E} = & \hat{x} \left( \frac{1}{\kappa_y} \frac{\partial}{\partial y} H_z + \zeta_y * \frac{\partial}{\partial y} H_z - \frac{1}{\kappa_z} \frac{\partial}{\partial z} H_y - \zeta_z * \frac{\partial}{\partial z} H_y \right) + \\ & \hat{y} \left( \frac{1}{\kappa_z} \frac{\partial}{\partial z} H_x + \zeta_z * \frac{\partial}{\partial z} H_x - \frac{1}{\kappa_x} \frac{\partial}{\partial x} H_z - \zeta_x * \frac{\partial}{\partial x} H_z \right) + \\ & \hat{z} \left( \frac{1}{\kappa_x} \frac{\partial}{\partial x} H_y + \zeta_x * \frac{\partial}{\partial x} H_y - \frac{1}{\kappa_y} \frac{\partial}{\partial y} H_x - \zeta_y * \frac{\partial}{\partial y} H_x \right) \end{aligned}$$

$$(2.15b) \quad \begin{aligned} -\mu \frac{\partial}{\partial t} \mathbf{H} = & \hat{x} \left( \frac{1}{\kappa_y} \frac{\partial}{\partial y} E_z + \zeta_y * \frac{\partial}{\partial y} E_z - \frac{1}{\kappa_z} \frac{\partial}{\partial z} E_y - \zeta_z * \frac{\partial}{\partial z} E_y \right) + \\ & \hat{y} \left( \frac{1}{\kappa_z} \frac{\partial}{\partial z} E_x + \zeta_z * \frac{\partial}{\partial z} E_x - \frac{1}{\kappa_x} \frac{\partial}{\partial x} E_z - \zeta_x * \frac{\partial}{\partial x} E_z \right) + \\ & \hat{z} \left( \frac{1}{\kappa_x} \frac{\partial}{\partial x} E_y + \zeta_x * \frac{\partial}{\partial x} E_y - \frac{1}{\kappa_y} \frac{\partial}{\partial y} E_x - \zeta_y * \frac{\partial}{\partial y} E_x \right). \end{aligned}$$

To solve for  $\zeta_w(t) * \frac{\partial H_v}{\partial w}$  the discrete impulse response of  $\zeta_w(t)$ ,  $Z_w(m)$ , is calculated<sup>62</sup>

$$Z_w(m) = \int_{m\Delta_t}^{(m+1)\Delta_t} \zeta_w(\tau) d\tau = c_w e^{mb_w}$$

where  $b_w$  is defined as

$$b_w = e^{-\left(\frac{\sigma_w}{\varepsilon \kappa_w} + \frac{a_w}{\varepsilon}\right) \Delta_t},$$

and  $c_w$  is defined as

$$c_w = \frac{\sigma_w}{\sigma_w \kappa_w + \kappa_w^2 a_w} (b_w - 1).$$

The convolution can then be implemented discretely in a recursive fashion by

$$(2.16) \quad \psi_{w,v}(n) = \zeta_w(t) * \frac{\partial H_v}{\partial w} \Big|_{t=n\Delta_t} \approx b_w \psi_{w,v}(n-1) + c_w \frac{\partial}{\partial w} H_v(n).$$

The same procedure can be repeated for  $\zeta_w(t) * \frac{\partial E_v}{\partial w}$ . Substituting Equation 2.16 into Equations 2.15, the Maxwell curl equations inside the PMLs can be written as

$$(2.17a) \quad \begin{aligned} \varepsilon \frac{\partial}{\partial t} \mathbf{E} = & \hat{x} \left( \psi_{E_{x,y}} - \psi_{E_{x,z}} + \frac{1}{\kappa_y} \frac{\partial}{\partial y} H_z - \frac{1}{\kappa_z} \frac{\partial}{\partial z} H_y \right) + \\ & \hat{y} \left( \psi_{E_{y,z}} - \psi_{E_{y,x}} + \frac{1}{\kappa_z} \frac{\partial}{\partial z} H_x - \frac{1}{\kappa_x} \frac{\partial}{\partial x} H_z \right) + \\ & \hat{z} \left( \psi_{E_{z,x}} - \psi_{E_{z,y}} + \frac{1}{\kappa_x} \frac{\partial}{\partial x} H_y - \frac{1}{\kappa_y} \frac{\partial}{\partial y} H_x \right) \end{aligned}$$

$$(2.17b) \quad \begin{aligned} -\mu \frac{\partial}{\partial t} \mathbf{H} = & \hat{x} \left( \psi_{E_{x,y}} - \psi_{E_{x,z}} + \frac{1}{\kappa_y} \frac{\partial}{\partial y} E_z - \frac{1}{\kappa_z} \frac{\partial}{\partial z} E_y \right) + \\ & \hat{y} \left( \psi_{E_{y,z}} - \psi_{E_{y,x}} + \frac{1}{\kappa_z} \frac{\partial}{\partial z} E_x - \frac{1}{\kappa_x} \frac{\partial}{\partial x} E_z \right) + \\ & \hat{z} \left( \psi_{E_{z,x}} - \psi_{E_{z,y}} + \frac{1}{\kappa_x} \frac{\partial}{\partial x} E_y - \frac{1}{\kappa_y} \frac{\partial}{\partial y} E_x \right). \end{aligned}$$

From here the same discretization and update equation generation scheme from the Yee algorithm can be used to generate update equations for the PML regions.<sup>62</sup>

In continuous space the fraction of light that is reflected off the PML surface at an angle  $\theta$  from the surface normal is

$$(2.18) \quad R(\theta) = e^{-2\sigma_w \eta d \cos \theta},$$

where  $\eta$  is the PML's impedance, and  $d$  is the PML thickness.<sup>62</sup> While Equation 2.18 implies that a large  $\sigma$  should be chosen to limit the reflection of light off the PML, discretization errors increase the reflection with increasing  $\sigma$ . To balance the two sources of error, a polynomial grading scheme is used for  $\sigma_w$

$$(2.19) \quad \sigma_w(w) = \begin{cases} \left(\frac{w}{d}\right)^m \sigma_{w,max}, & w \leq d \\ 0, & w > d \end{cases},$$

where  $w$  is the distance of the point from the front edge of the PML,  $m$  is the polynomial scaling factor (typically a value in between 3 and 4), and  $\sigma_{w,max}$  is the maximum value of  $\sigma$ .<sup>62</sup> Using this grading the reflection error becomes

$$(2.20) \quad R(\theta) = e^{-2\eta \cos \theta \int_0^d \sigma_w(w') dw'}.$$

If the desired maximum reflection error,  $R(0)$ , is known then  $\sigma_{w,max}$  can be calculated from 2.20 with

$$(2.21) \quad \sigma_{w,max} = -\frac{(m+1) \ln[R(0)]}{2\eta d},$$

but the optimal value of  $\sigma_{max}$  is system dependent.<sup>62</sup> A good starting point for  $\sigma_{max}$  has been discovered through an extensive series of numerical tests where an optimal value for  $\sigma_{w,max}$  is

$$(2.22) \quad \sigma_{w,opt} = -\frac{0.8(m+1)}{\eta\Delta_w},$$

but further scaling maybe necessary.<sup>62</sup> The same grading scheme is used for  $\kappa_w$ , but with a slight modification such that  $\kappa_w$  is always greater than or equal to one,<sup>62</sup>

$$(2.23) \quad \kappa_w(w) = \begin{cases} 1 + \left(\frac{w}{d}\right)^m (\kappa_{w,max} - 1), & w \leq d \\ 1, & w > d \end{cases}.$$

A different grading scheme is used for  $a_w$ .

$$(2.24) \quad a_w = \begin{cases} a_{w,max} \left(\frac{d-w}{d}\right)^{m_a}, & w \leq d \\ 0, & w > d \end{cases},$$

where  $m_a$  is a different polynomial scaling factor that is typically one.<sup>62</sup> The scheme maximizes  $a_w$  at the surface to reduce reflections, but gets smaller deeper into the PML to increase the attenuation of the fields.<sup>62</sup>

## 2.5 Generating Incident Radiation

The final aspect of the FDTD algorithm to be discussed in this chapter is the introduction of incident waves into the cell. The easiest way to introduce a source term in FDTD is specifying the values of  $\mathbf{E}$  and  $\mathbf{H}$  at certain points within the cell. While this will introduce the desired wave form into the cell, it also creates reflection surfaces that limit the accuracy of the calculation. A second approach is to introduce the electromagnetic waves through the  $\mathbf{J}$  and  $\mathbf{M}$  terms in

Equations 2.5.<sup>62</sup> This approach scales the current densities such that the resulting electromagnetic fields match the initial pulse function,  $f$ .<sup>62</sup> While including the source terms via  $\mathbf{J}$  and  $\mathbf{M}$  does not introduce reflection surfaces, it can lead to persistent diverging fields depending on the source geometry and the shape of  $f$ .<sup>62</sup>

### 2.5.1 Total Field/Scattered Field

A better approach to generate the incident waves is through total field/scattered field (TF/SF) surfaces.<sup>62,70</sup> TF/SF method separates  $\mathbf{E}$  and  $\mathbf{H}$  into

$$(2.25a) \quad \mathbf{E} = \mathbf{E}_{\text{inc}} + \mathbf{E}_{\text{scat}},$$

$$(2.25b) \quad \mathbf{H} = \mathbf{H}_{\text{inc}} + \mathbf{H}_{\text{scat}},$$

where  $\mathbf{E}_{\text{inc}}$  and  $\mathbf{H}_{\text{inc}}$  are the incident electric and magnetic fields and  $\mathbf{E}_{\text{scat}}$  and  $\mathbf{H}_{\text{scat}}$  are the scattered electric and magnetic fields.<sup>62</sup> The FDTD grids are then separated into total and scattered field regions, by a set of six planes,  $\mathcal{S}$ , representing the faces of a rectangular prism

$$(2.26) \quad \mathcal{S} = \{i_0, i_1, j_0, j_1, k_0, k_1\},$$

where  $i_0$  and  $i_1$  are the  $x$ - coordinates of the left and right faces,  $j_0$  and  $j_1$  are the  $y$ - coordinates of the bottom and top faces, and  $k_0$  and  $k_1$  are the  $z$ - coordinates of the back and front faces of the prism.<sup>62</sup> It is assumed that  $\mathbf{E}_{\text{inc}}$  and  $\mathbf{H}_{\text{inc}}$  are known for all points in the computational domain.<sup>62</sup> By selectively including or excluding the incident field along  $\mathcal{S}$  an incident plane wave can be introduced in only the total field region.<sup>62</sup>

### 2.5.1.1 Calculation of Incident Fields

The largest challenge with the TF/SF method is efficiently calculating the incident fields. Calculating the source terms across all points in  $\mathcal{S}$  is too computationally expensive to be practical for most systems.<sup>71</sup> The integer mapping technique developed by Tan and Potter is a relatively inexpensive method for calculating the incident field at all points.<sup>72-75</sup> The method propagates the incident fields on separate one dimensional FDTD grids, oriented along a line parallel to the direction of propagation,  $\mathbf{p}$ .<sup>71</sup> The only restrictions on  $\mathbf{p}$  is that it must contain two points in  $\mathbf{x}$ , such that  $\{x \in [i\Delta_x, j\Delta_y, k\Delta_z]\}$ .<sup>71</sup> The propagation angles for the system can then be determined by the following

$$(2.27a) \quad \tan \varphi = \frac{p_y}{p_x}$$

$$(2.27b) \quad \tan \theta = \frac{\sqrt{p_x^2 + p_y^2}}{p_z}.$$

Using  $\mathbf{p}$ , a point in  $\mathbf{x}$  can be mapped onto a point on the one-dimensional grids,  $\mathbf{r}$ , via

$$(2.28) \quad \mathbf{r}_{i,j,k} = p_x i \Delta_x + p_y j \Delta_y + p_z k \Delta_z = \mathbf{r}_{ir} = i_r \Delta_r,$$

where  $i_r = m_x i + m_y j + m_z k$ ;  $m_x$ ,  $m_y$ , and  $m_z$  are integers; and  $\Delta_r$  is a uniform discrete spacing for the one dimensional incident grids.<sup>71</sup> The components of  $\mathbf{p}$  and  $\mathbf{m}$  are related to each other by

$$(2.29) \quad p_w \Delta_w = m_w \Delta_r,$$

where  $w = x, y,$  or  $z$ .<sup>71</sup> Using Equations 2.28 and 2.29 the incident field update equations can be generated from Equations 2.5

$$(2.30a) \quad E_{x,inc} \Big|_{i_r + \frac{m_x}{2}}^{n+1} = E_{x,inc} \Big|_{i_r + \frac{m_x}{2}}^n + \frac{\Delta_t}{\epsilon_{i_r + \frac{m_x}{2}}} \left( \frac{H_{y,inc} \Big|_{i_r + \frac{m_x+m_z}{2}}^{n+\frac{1}{2}} - H_{y,inc} \Big|_{i_r + \frac{m_x-m_z}{2}}^{n+\frac{1}{2}}}{\Delta_z} - \frac{H_{z,inc} \Big|_{i_r + \frac{m_x+m_y}{2}}^{n+\frac{1}{2}} - H_{z,inc} \Big|_{i_r + \frac{m_x-m_y}{2}}^{n+\frac{1}{2}}}{\Delta_y} - J_{x,inc} \Big|_{i_r + \frac{m_x}{2}}^{n+\frac{1}{2}} \right).$$

$$(2.30b) \quad E_{y,inc} \Big|_{i_r + \frac{m_y}{2}}^{n+1} = E_{y,inc} \Big|_{i_r + \frac{m_y}{2}}^n + \frac{\Delta_t}{\epsilon_{i_r + \frac{m_y}{2}}} \left( \frac{H_{z,inc} \Big|_{i_r + \frac{m_y+m_x}{2}}^{n+\frac{1}{2}} - H_{z,inc} \Big|_{i_r + \frac{m_y-m_x}{2}}^{n+\frac{1}{2}}}{\Delta_x} - \frac{H_{x,inc} \Big|_{i_r + \frac{m_y+m_z}{2}}^{n+\frac{1}{2}} - H_{x,inc} \Big|_{i_r + \frac{m_y-m_z}{2}}^{n+\frac{1}{2}}}{\Delta_z} - J_{y,inc} \Big|_{i_r + \frac{m_y}{2}}^{n+\frac{1}{2}} \right),$$

$$(2.30c) \quad E_{z,inc} \Big|_{i_r + \frac{m_z}{2}}^{n+1} = E_{z,inc} \Big|_{i_r + \frac{m_z}{2}}^n + \frac{\Delta_t}{\epsilon_{i_r + \frac{m_z}{2}}} \left( \frac{H_{x,inc} \Big|_{i_r + \frac{m_z+m_y}{2}}^{n+\frac{1}{2}} - H_{x,inc} \Big|_{i_r + \frac{m_z-m_y}{2}}^{n+\frac{1}{2}}}{\Delta_y} - \frac{H_{y,inc} \Big|_{i_r + \frac{m_z+m_x}{2}}^{n+\frac{1}{2}} - H_{y,inc} \Big|_{i_r + \frac{m_z-m_x}{2}}^{n+\frac{1}{2}}}{\Delta_x} - J_{z,inc} \Big|_{i_r + \frac{m_z}{2}}^{n+\frac{1}{2}} \right),$$

$$(2.30d) \quad H_{x,inc} \Big|_{i_r + \frac{m_y+m_z}{2}}^{n+\frac{1}{2}} = H_{x,inc} \Big|_{i_r + \frac{m_y+m_z}{2}}^{n-\frac{1}{2}} + \frac{\Delta_t}{\mu_{i_r + \frac{m_y+m_z}{2}}} \left( \frac{E_{z,inc} \Big|_{i_r + \frac{m_z}{2} + m_y}^n - E_{z,inc} \Big|_{i_r + \frac{m_z}{2}}^n}{\Delta_y} - \frac{E_{y,inc} \Big|_{i_r + \frac{m_y}{2} + m_z}^n - E_{y,inc} \Big|_{i_r + \frac{m_y}{2}}^n}{\Delta_z} - M_{x,inc} \Big|_{i_r + \frac{m_y+m_z}{2}}^{n+\frac{1}{2}} \right),$$

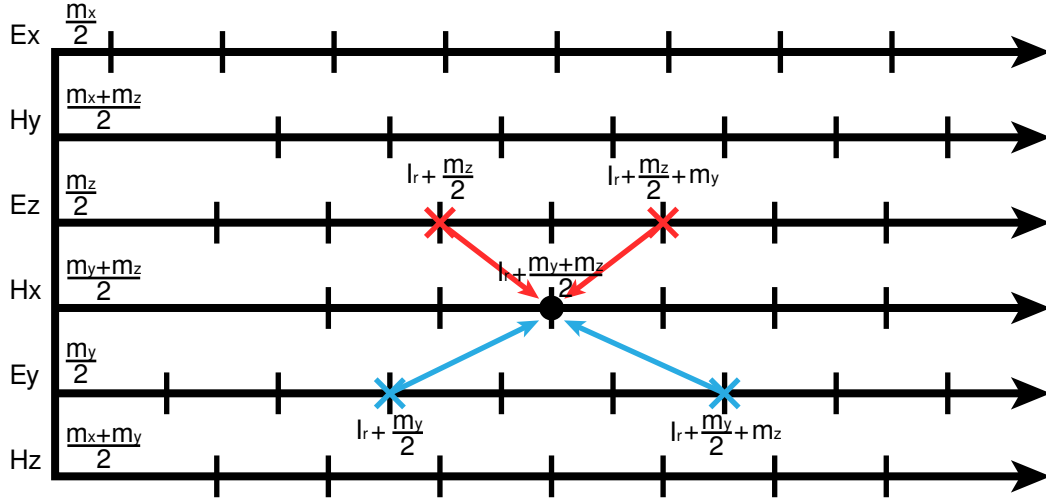


Figure 2.2. Schematic showing the coupling between each incident field grid.

$$(2.30e) \quad H_{y,inc} \Big|_{i_r + \frac{m_x + m_z}{2}}^{n + \frac{1}{2}} = H_{y,inc} \Big|_{i_r + \frac{m_x + m_z}{2}}^{n - \frac{1}{2}} + \frac{\Delta_t}{\mu_{i_r + \frac{m_x + m_z}{2}}} \left( \frac{E_{x,inc} \Big|_{i_r + \frac{m_x}{2} + m_z}^n - E_{x,inc} \Big|_{i_r + \frac{m_x}{2}}^n}{\Delta_z} - \frac{E_{z,inc} \Big|_{i_r + \frac{m_z}{2} + m_x}^n - E_{z,inc} \Big|_{i_r + \frac{m_z}{2}}^n}{\Delta_x} - M_{y,inc} \Big|_{i_r + \frac{m_x + m_z}{2}}^{n + \frac{1}{2}} \right),$$

$$(2.30f) \quad H_{z,inc} \Big|_{i_r + \frac{m_x + m_y}{2}}^{n + \frac{1}{2}} = H_{z,inc} \Big|_{i_r + \frac{m_x + m_y}{2}}^{n - \frac{1}{2}} + \frac{\Delta_t}{\mu_{i_r + \frac{m_x + m_y}{2}}} \left( \frac{E_{y,inc} \Big|_{i_r + \frac{m_y}{2} + m_x}^n - E_{y,inc} \Big|_{i_r + \frac{m_y}{2}}^n}{\Delta_x} - \frac{E_{x,inc} \Big|_{i_r + \frac{m_x}{2} + m_y}^n - E_{x,inc} \Big|_{i_r + \frac{m_x}{2}}^n}{\Delta_y} - M_{z,inc} \Big|_{i_r + \frac{m_x + m_y}{2}}^{n + \frac{1}{2}} \right).$$

Figure 2.2 illustrates that the incident grids are six coupled and staggered 1-D grids, and it illustrates the update procedure for the  $H_{x,inc}$  grid.

The incident fields are bounded by a CPML at both ends, and a soft source is used to inject the plane waves into the incident grids. The incident wave is generated by scaling the time

profile of the wave,  $f$ , with the correct projection vectors  $\mathbf{P}_E$  and  $\mathbf{P}_H$

$$(2.31a) \quad \mathbf{J}_{\text{inc}}(\mathbf{x}, t) = \frac{\Delta_t}{\Delta_r(m_x + m_y + m_z)} \mathbf{P}_E(\psi, \varphi, \theta, \alpha) f(t - \sqrt{\mu_b \varepsilon_b} \mathbf{p} \cdot \mathbf{x})$$

$$(2.31b) \quad \mathbf{M}_{\text{inc}}(\mathbf{x}, t) = \frac{\Delta_t}{\Delta_r(m_x + m_y + m_z)} \mathbf{P}_H(\psi, \varphi, \theta, \alpha) f(t - \sqrt{\mu_b \varepsilon_b} \mathbf{p} \cdot \mathbf{x}) \frac{1}{\eta_B},$$

where  $\varepsilon_B$ ,  $\mu_B$ , and  $\eta_B$  are the permittivity, permeability and impedance of the background media, respectively;  $\psi$  is the polarization orientation angle; and  $\alpha$  describes the ellipticity of the light.<sup>71</sup>

The prefactor in front of  $\mathbf{J}_{\text{inc}}$  and  $\mathbf{M}_{\text{inc}}$  ensures the incident electro-magnetic fields have the same intensity as  $f$ . The components of  $\mathbf{P}_E$  and  $\mathbf{P}_H$  are

$$(2.32a) \quad P_{E_x}(\psi, \theta, \varphi, \alpha) = \cos \psi \sin \varphi - e^{i\alpha} \sin \psi \cos \theta \cos \varphi$$

$$(2.32b) \quad P_{E_y}(\psi, \theta, \varphi, \alpha) = \cos \psi \sin \varphi - e^{i\alpha} \sin \psi \cos \theta \cos \varphi$$

$$(2.32c) \quad P_{E_z}(\psi, \theta, \varphi, \alpha) = e^{i\alpha} \sin \psi \cos \theta.$$

$$(2.32d) \quad P_{H_x}(\psi, \theta, \varphi, \alpha) = e^{i\alpha} \sin \psi \sin \varphi - \cos \psi \cos \theta \cos \varphi$$

$$(2.32e) \quad P_{H_y}(\psi, \theta, \varphi, \alpha) = e^{i\alpha} \sin \psi \sin \varphi - \cos \psi \cos \theta \cos \varphi$$

$$(2.32f) \quad P_{H_z}(\psi, \theta, \varphi, \alpha) = \cos \psi \cos \theta.$$

### 2.5.1.2 Consistency Conditions

With the incident field now known at all grid locations the final consistency conditions for all faces of the prism can be derived. These conditions extend Equations 2.5a-f to add or subtract the incident fields along  $\mathbf{S}$  such that the total and scattered field regions are updated with only total and scattered fields, respectively. For a complete list of all consistency conditions see Appendix A.<sup>62,71</sup>

## 2.6 Time Stepping with the Yee Algorithm

Figure 2.3 illustrates the FDTD time stepping algorithm. The first step in the FDTD algorithm is to initialize all fields to zero at time zero. Then the  $\mathbf{H}$  fields including the associated PML fields are propagated to time  $\frac{\Delta_t}{2}$ .<sup>62</sup> Then the incident electric and magnetic fields are updated to a time  $\Delta_t$  and  $\frac{\Delta_t}{2}$  respectively.<sup>62</sup> Finally the electric fields are propagated to  $\Delta_t$  and all field outputs are taken.<sup>62</sup> For outputs that require multiple field components, the individual components are averaged to a central point and then combined.<sup>62</sup> The algorithm then repeats

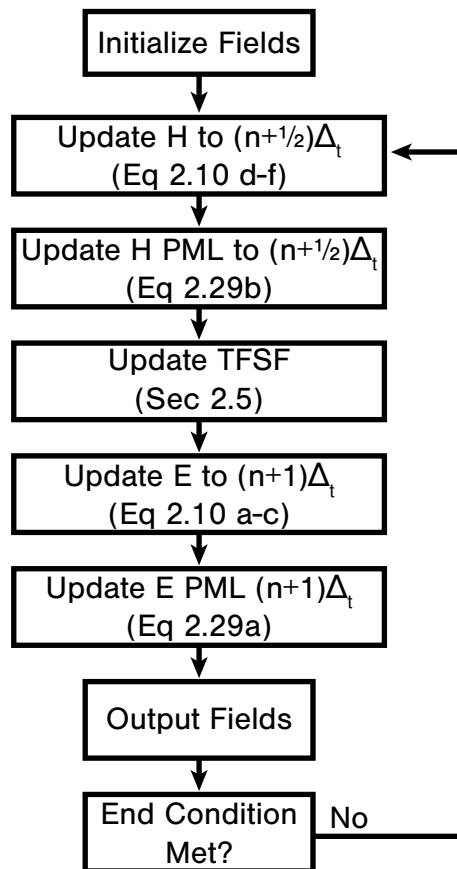


Figure 2.3. Flow chart illustrating the time stepping of the FDTD method.

until some convergence condition is met.<sup>62</sup> Throughout this work, the end condition will be a specified end time, but field convergence conditions could also be used.<sup>62</sup>

## CHAPTER 3

**Coupling Quantum Emitters to Random 2D Nanoplasmonic Structures**

We combine theory and experimental studies to investigate the coupling between colloidal quantum dots and randomly generated gold nanoislands. In such systems, the gold nanoislands act as classical antennas, amplifying the light absorbed by the quantum dots. They may thus find applications in detection, sensing, and plasmon-enhanced solar energy conversion. We use the two-dimensional finite-difference time-domain method to demonstrate plasmonic control of the enhancement factor near the islands plasmon resonance. Furthermore, we experimentally and numerically show how tuning the plasmon resonance to the band gap energy of the quantum dot can lead to a broadening of the quantum dots absorption peak. The simulations predict a surprising linear scaling with quantum dot density, which is confirmed by experimental results.

This chapter has been reproduced with permission, from Ref 132

### 3.1 Introduction

Devices based on colloidal quantum dots (QDs) and specific organic linker molecules offer a compelling combination of low-cost, solution processability, tunability, light-sensitivity, and quantum properties at room temperature. Nevertheless, despite tremendous improvement in QD synthesis, film formation, and electron transport properties, the overall device performance remains limited.<sup>76</sup> A major challenge associated with improving QD-based devices is the relatively small absorption cross-section of the QDs. In order to realize devices that combine sensitivity with high performance, one must increase the light absorption at a low-cost.

One way to improve the absorption and emission quantum efficiency of the QDs is to couple them to plasmonically active nanoparticles.<sup>24,26,76-82</sup> Plasmons are collective oscillations of conduction band electrons at metal-dielectric interfaces that generate intense electromagnetic fields in their vicinity with spatial variations on the nanometer scale.<sup>2,83</sup> Therefore plasmonics is attractive for nanooptics applications, where focusing light beyond the diffraction limit is important.<sup>2</sup> Indeed, plasmonic nanostructures are used to enhance the efficiencies of photodetectors,<sup>24,26,84</sup> solar cells,<sup>85-87</sup> and light emitting diodes,<sup>88-90</sup> in addition to their well-established use in tip-enhanced spectroscopies.<sup>91-95</sup> In many cases ordered nanostructure morphologies, such as metal nanoparticle arrays, gratings,<sup>96</sup> and circular antennas,<sup>77</sup> are used to improve the devices quantum efficiency. Although such structures lead to the desired efficiency-enhancement, establishing their application in research laboratories, the costs associated with their production are too high for general use. Wrinkled metal films<sup>97</sup> and etched alloys<sup>79</sup> are also used to enhance photoluminescence but they cannot be integrated easily into existing devices.

In this work we illustrate, experimentally and numerically, the potential of self-assembled QD films coupled to random gold nanoisland films as a route to overcome these challenges. After developing a model for the gold nanoisland films, we study the effects of detuning of the QDs energy band gap with respect to the plasmon resonance by monitoring the red-shift and intensity of the gold nanoislands plasmon resonance. Next, we compare the QDs absorption enhancement factors calculated for different gold nanoisland configurations. Finally, we test a realistic system and explore the effects of the QD number density on the absorption of the films.

## 3.2 Methodology

### 3.2.1 Theoretical Methods

The two dimensional FDTD method was used to calculate the optical properties of the gold nanoisland films within classical electrodynamics. Non-local effects have at most a minor influence on the optical properties of 10 nm long particles,<sup>98-100</sup> and become insignificant for larger particles, therefore a classical description is appropriate. The dielectric function parameters for gold were taken from the work of Rakic et al,<sup>4</sup> and the QD parameters were obtained by fitting the experimental absorption spectra at the band gap energy to a single Lorentzian.<sup>101</sup> Recently developed methods can include quantum mechanical effects into the optical response of the QDs,<sup>61,102</sup> but for the observables and the system considered here the classical approximation is valid.<sup>101</sup> The high frequency dielectric constant for the quantum dots are taken to be that of the bulk semiconductor for both CdSe and PbS. The pole parameters used for the CdSe (610 nm) quantum dot's dielectric function are  $\omega_{QD} = 2.03\text{eV}$ ,  $\gamma_{QD} = 140\text{meV}$ , and  $\sigma = 0.65$ . The PbS (850 nm) quantum dot's dielectric function are  $\omega_{QD} = 1.46\text{eV}$ ,  $\gamma_{QD} = 260\text{meV}$ , and  $\sigma = 5.0$ . Figure 3.1 shows the absorption cross-section of both QDs.

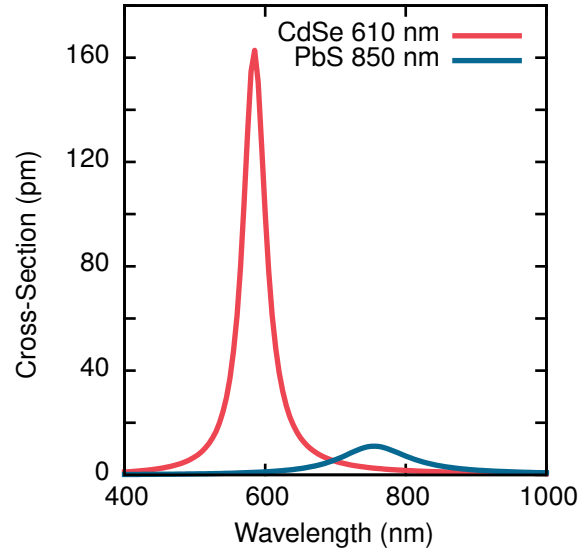


Figure 3.1. The absorption cross-section of a single CdSe 610 nm (red) and PbS 850 nm (blue) quantum dot using the single Lorentzian model.

Figure 3.2 shows a diagram of the FDTD cell. The nanoparticle system is in the center of the cell, with TF/SF region placed 20 nm away from the gold nanoellipse at all sides. The system is excited using a Gaussian pulse with a center frequency of 480 THz and a pulse duration of 1.39 fs propagating from the bottom of the TF/SF region represented by the red box. The enhancement factor calculations are performed using a 2 Å step size, while the other CdSe 610 nm QD and PbS 850 nm QD calculations used a 5 Å and a 2.5 Å step size respectively. The time step ( $\Delta_t$ ) is set by  $\Delta_t = \Delta_x c S$ , where  $\Delta_x$  is the spatial step size,  $c$  is the speed of light, and  $S$  is the Courant factor, set to 0.5 for all calculations. The absorption and scattering cross-sections are calculated in the regions shown in the blue boxes 10 nm inside and outside the TF/SF region respectively. The QD absorption cross-section is calculated in a region surrounding only the QD. The cell is terminated by a convolution perfectly matched layer that is at least 20 grid points wide in all directions.

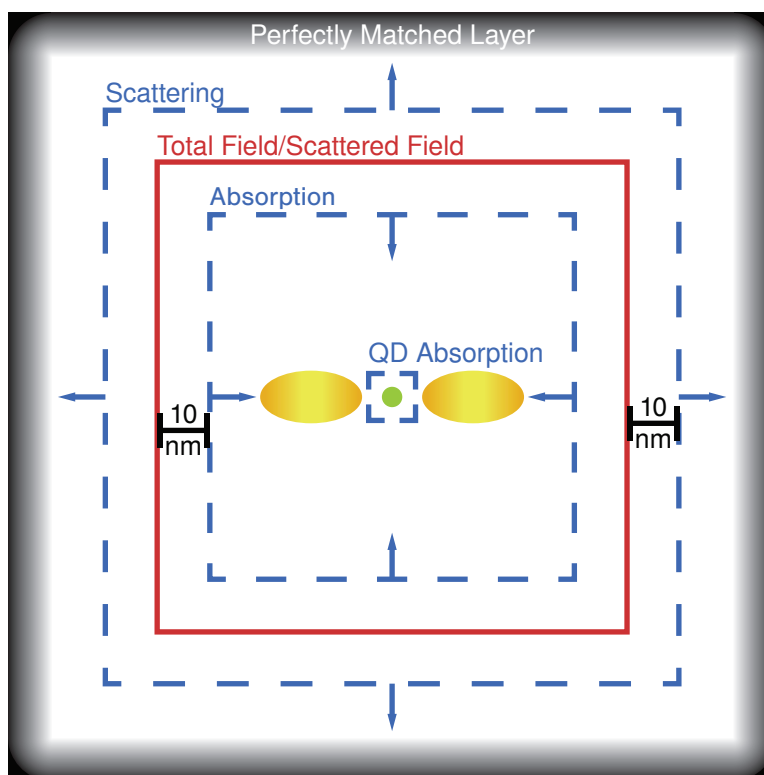


Figure 3.2. The cell diagram for the nanoislands (gold ellipses) coupled to the quantum dots (green filled in circle). The absorption, scattering and quantum dot absorption are calculated on the surfaces defined by the labeled blue boxes. The incident Gaussian plane wave is introduced from the TF/SF region defined by the red box. The cell is surrounded by a convolution perfectly matched layer to act as absorbing boundary conditions.

### 3.2.2 Experimental Methods

Following a previous study,<sup>103</sup> samples were prepared in two consecutive stages starting with the random gold nanoisland film preparation and followed by adsorption of the QDs. In the first step, glass substrates are cleaned in acetone and ethanoal and an ultrathin Au film with a nominal thickness of 5 nm was deposited using e-gun evaporation. The deposition rate was 0.3 Å/s and it was done at room temperature under pressure of  $10^{-6}$  torr. To adjust and tune the

plasmonic resonance of this random film, the samples were annealed on a hot plate for several minutes with temperatures reaching up to  $\sim 200$  °C.

In the second step the QDs were covalently bound to a homogenous, self-assembled layer of molecules on the gold surface. The samples were immersed for 17 h in a 1mM 1,9-nonanedithiol ethanol solution under a nitrogen environment, then washed in absolute ethanol and toluene and immersed in a diluted 0.05%ww QDs solution. We used 2 types of commercial QDs: CdSe 610nm and PbS 850nm (the numbers represent the peaks of the corresponding emission wavelengths). Half of the sample was not immersed in the QD solution to act as a bare gold nanoisland film reference.

In order to understand the enhancement process better, the spectral behavior of the samples was studied at different QD densities. To control the QD surface density the samples were immersed in the QD solution several times for 20 min. After every 20 min exposure the samples were washed in absolute toluene and dried under a nitrogen gas stream. Then the optical properties of the film were measured and the process was repeated 10 times to get a maximum exposure time of 200 min. The nanoisland surfaces were not changed through each iteration to ensure changes in the optical spectra were from changes in the QD density and not the nanoisland films.

Spectral analysis of the films was used to explore the optical properties because of the highly dispersive nature of plasmons. A broad-band white light source of a Tungsten-Halogen lamp with an integrating sphere and a spectrometer was used to record the changes in the absorption of the films with changing QD number density. A minimal amount of reflection was seen in the films, and scattering was reduced by measuring the total transmission, meaning the measured

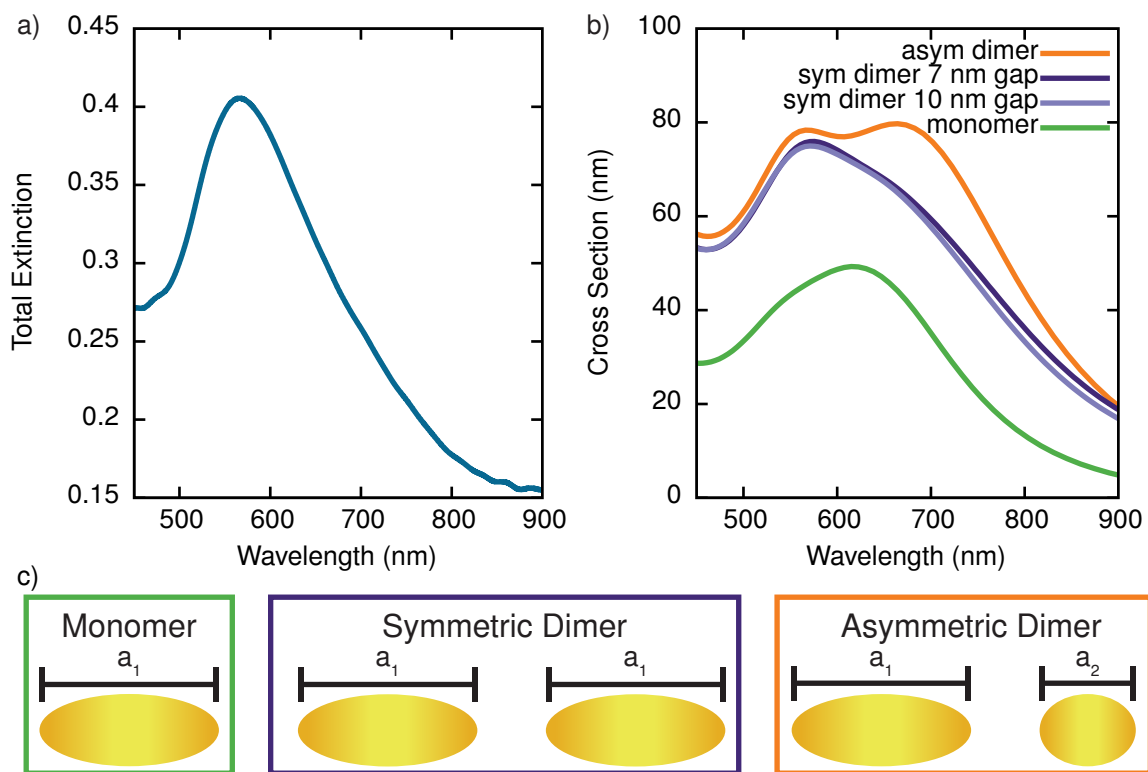


Figure 3.3. a) Experimental extinction of the random Au nanoparticles. b) Theoretical absorption cross-section of the gold nanoisland surfaces as approximated by the monomer, symmetric dimer, and asymmetric dimer models. c) An illustration of the depicted models with the box color corresponding to the line color in part b

light extinction ( $1 - T_{\text{tot}}$ ) indicates mostly the absorption of the samples. Data was recorded with Ocean Optics usb4000 VIS-NIR spectrometer.

### 3.3 Results

#### 3.3.1 Building the Gold Nanoisland Model

Figure 3.3 compares the measured extinction spectrum of the gold nanoisland films and the calculated absorption cross-section of various model systems. The three models tested are

monomers; symmetric dimers, where both nanoellipses have the same dimensions; and asymmetric dimers, where the nanoellipses have different particle lengths. As the QDs and nanoparticles interact mainly with the local electro-magnetic fields, their overall optical properties can be modeled as a statistical average over all gold particle arrangements. The nanoislands are 11 nm high with lengths ranging from 10 nm to 200 nm and the weights for each structure taken from an analysis of similar nanoisland films.<sup>104</sup> The bare gold nanoisland surfaces have a broad absorption peak at 566 nm, which is best matched by the symmetric dimer model, with a broad peak centered at 572 nm. Both the monomer and the asymmetric dimer models have peaks at 620 nm and 660 nm respectively, significantly red-shifted from the experimental values. The dimer model is largely unaffected by increasing the gap size to 10 nm, mostly increasing the long wavelength tail. The gap sizes of 7 nm and 10 nm were chosen because those are representative gaps seen in the films and are large enough to support a quantum dot in the center of the gap. The agreement between the symmetric dimer spectra and the gold nanoisland film suggests the possibility of a domain structure in the films, where similarly sized nanoparticles are more likely to couple to each other.

The surprising blue-shift of the dimer plasmon resonance is a result of averaging over islands with higher order resonance exemplified in Figure 3.4. The monomers absorption cross-section in Figure 3.4a has a single peak at 862 nm, while the dimer has two peaks at 1,008 nm and 658 nm. The field maps in Figure 3.4b show that the 658 nm peak is the result of the quadrupole resonance that begins to grow in. The blue-shift is thus a result of averaging the quadrupole resonance and dipole resonance for dimers of different sizes. Understanding how to control the film morphologies could improve existing and suggest new devices.

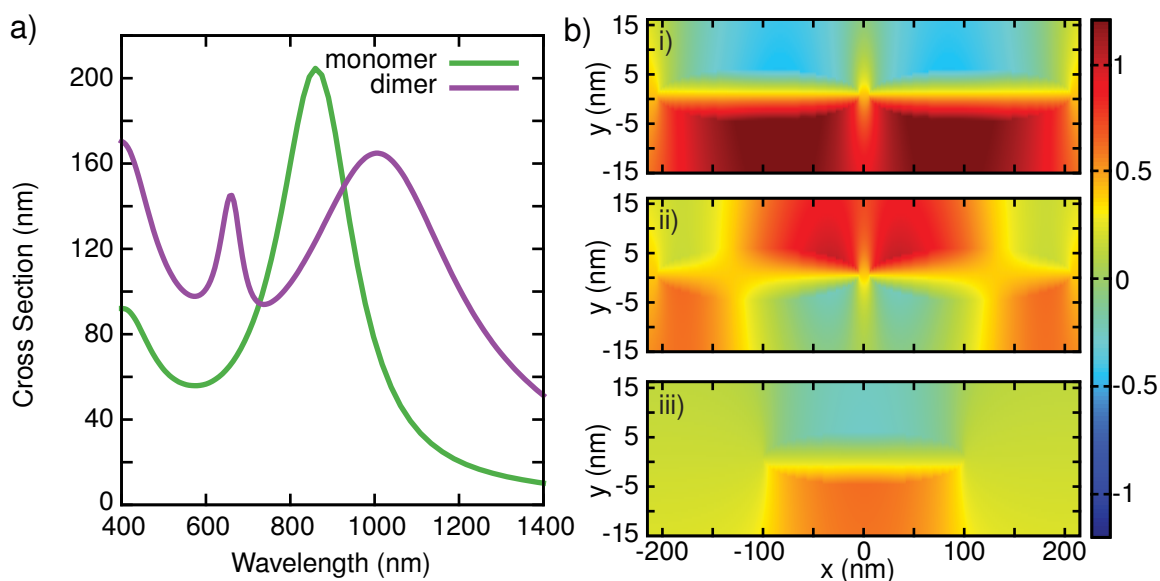


Figure 3.4. a) Absorption spectra of a 200 nm long, 11 nm high gold nanoellipse monomer and symmetric dimer. b) Map of the  $H_z$  field for the symmetric dimer under a constant wavelength excitation centered at i) 658 nm and ii) 1,008 nm, and iii) a monomer excited at 862 nm.

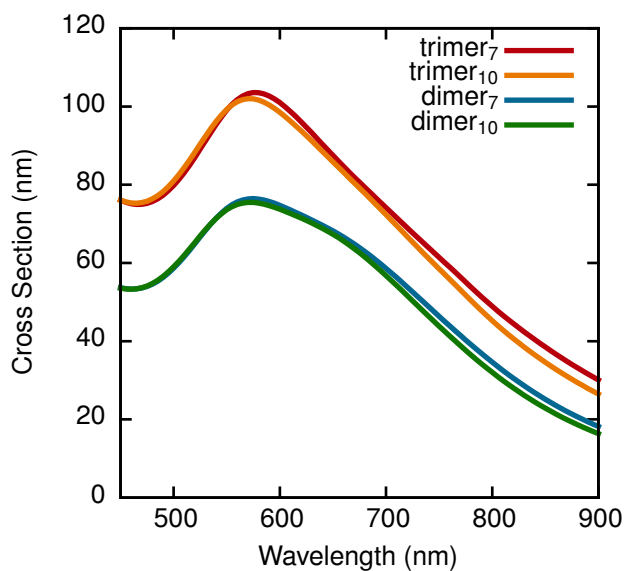


Figure 3.5. Absorption spectra of a symmetric trimer and dimer model of the nanoisland films with a 7 and 10 nm gap. For the trimers the gap between all nanoellipses are the same.

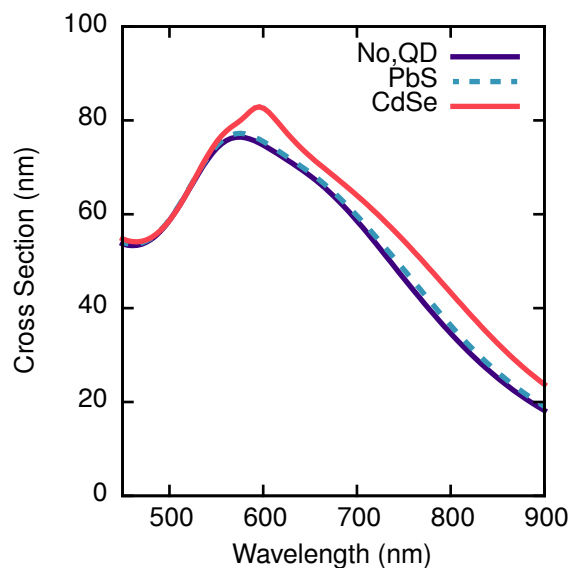


Figure 3.6. Simulated absorption cross-section of gold nanoellipse dimers with a gap size of 7 nm with PbS 850 nm or CdSe 610 nm quantum dots in the hot spot.

Further increasing the number of particles to include trimer geometries has minimal effects on the optical response of the nanoisland films as seen in Figure 3.5. Figure 3.5 shows a comparison of the symmetric trimer calculations with the symmetric dimers. The peaks are in the same position for both the 10 nm and 7 nm gap, with the only difference being an increase in the absorption cross-section as a third particle is added and a slight decrease in the shoulder of the peak. These results indicate that including additional islands minimally perturbs the film's optical response, with their main effect being a reduction in relative intensity of the dipolar resonances.

### 3.3.2 The Nature of the Nanoisland-Quantum Dot Coupling

Adding the QDs to the gold nanoislands film results in an increase of the coupled system absorption cross-section and a clear red-shift. Figure 3.6 shows the simulated absorption cross-section of a set of gold nanoellipse dimers with a CdSe 610 nm QD or a PbS 850 nm QD placed

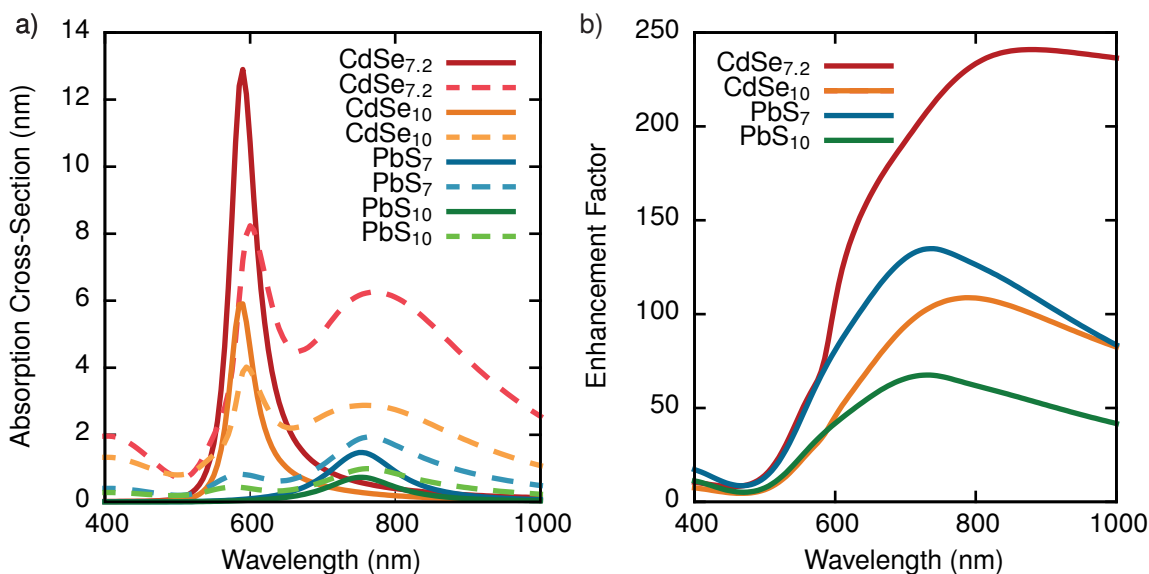


Figure 3.7. a) Absorption cross sections calculated directly, represented by the solid curves compared with results determined from the difference between the gold nanoisland absorption with and without quantum dots. The subscripts correspond to the gap size. b) Absorption enhancement for CdSe 610 nm and PbS 850 nm quantum dots inside a hot-spot of the nanodimer for a 7 nm and a 10 nm gap.

in the center of the 7 nm gap. The CdSe 610 nm QD has a stronger interaction, red-shifting the plasmon resonance by 21 nm and increasing the peak absorption cross-section by 6.44 nm. The PbS 850 nm QD has a weaker effect, red-shifting the plasmon resonance by only 1 nm and increasing the cross-section by 0.7 nm. While these spectra appear to demonstrate high absorption enhancement, effects from the gold nanoislands may have a significant role.

To remove any excess absorption from the gold nanoislands, Figure 3.7a compares the absorption cross-section of the QD calculated from a flux region containing only the QD, to the difference between the absorption of the gold nanoislands with and without the QD inside a 7 nm or 10 nm gap (see Figure 3.2 for a diagram of the cell). The difference spectra indicate both the QD and gold nanoisland absorptions are enhanced. The contribution is seen in the peaks

of the difference spectra that are off-resonance with the QD absorption mode, and red-shifts the main QD absorption peak. The difference spectra also skew the relative peak intensities by over reporting the PbS 850 nm QDs absorption and under reporting the CdSe 610 nm QDs absorption. Although a comparison of the spectra with and without the QDs reproduces the qualitative trends of QD absorption, increased activity in the gold nanoislands will create some differences.

Figure 3.7b shows the absorption enhancement of the QDs in the center of a 7 and a 10 nm gap, calculated by normalizing the QD absorption cross-section coupled to the nanoislands with their cross-section in vacuum. At the plasmon resonance, the CdSe 610 nm QD and PbS 850 nm QD have nearly equal enhancement factors for both gap sizes, suggesting that the plasmonic properties of the nanoislands determine the QDs enhancement factors. Tuning the plasmon resonance of the QDs band gap can also provide additional absorption at longer wavelengths. Coupling the CdSe 610 nm QDs to larger nanoislands induces a smaller, second peak in the QD absorption spectra near the nanoislands plasmon resonance, leading to considerably higher enhancement factor at longer wavelengths. These smaller peaks are responsible for the apparent broadening of the absorption cross-section in Figure 3.7a and the high enhancement factors in Figure 3.7b.

The change in the gold nanoisland absorption after coupling to the QDs is highly dependent on the structural parameters of the system, as seen in Figure 3.8. The plots reinforce the message of Figure 3.7a that changes in the gold nanoisland absorption is the primary cause of the off-resonant peaks in the difference spectra and can make a significant contribution to the systems overall absorption. For the 110 nm nanoislands, the large negative values at wavelengths less than  $\sim 750$  nm is the result of the red-shift of the plasmon resonance.

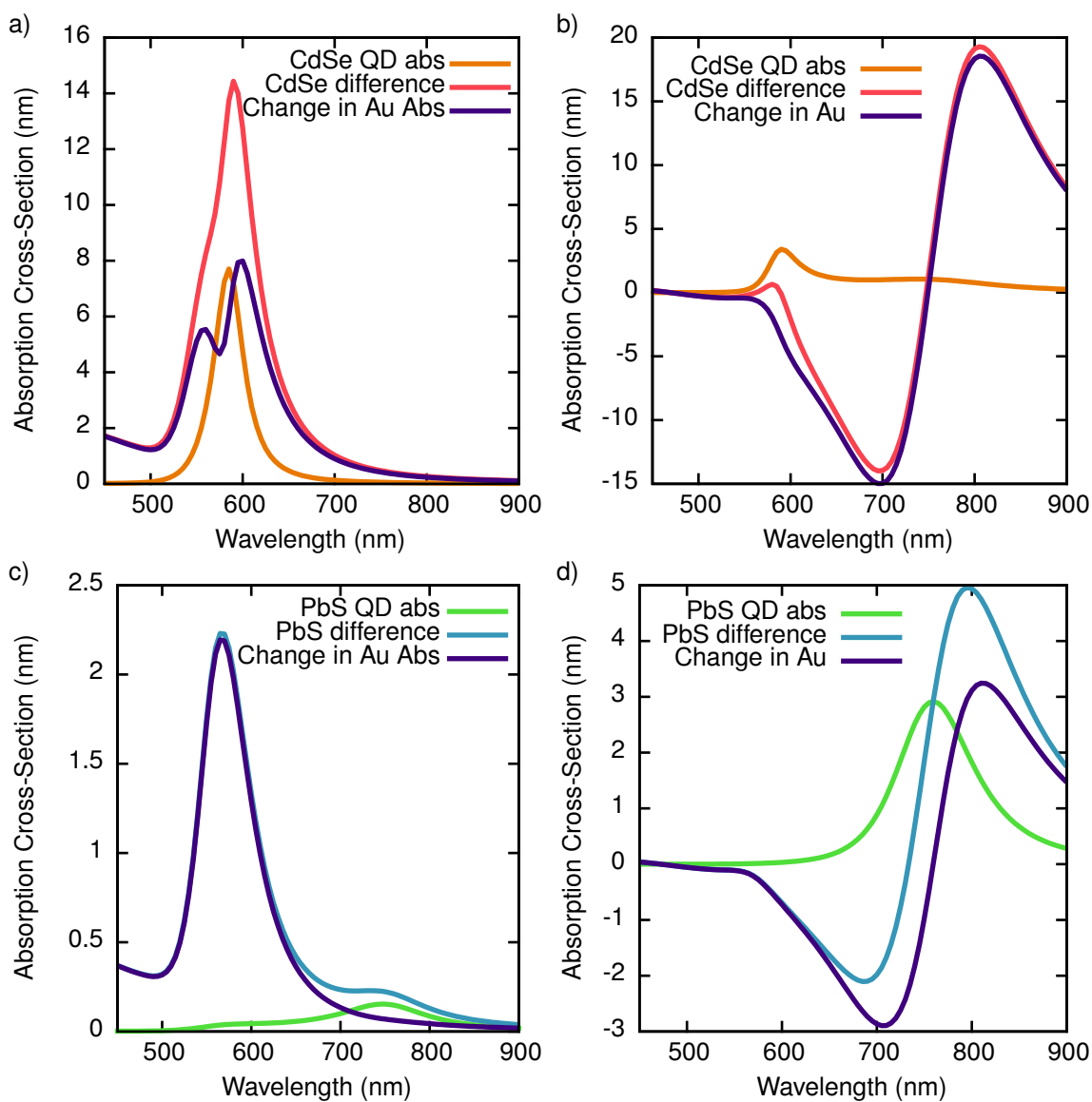


Figure 3.8. a) An approximation to the plasmonic loss into the 40 nm (a and c) and 110 nm (b and d) long dimers coupled to both the CdSe 610 nm QD (a and b) and PbS 850 nm QD (c and d) inside a 10 nm gap. The orange and green lines are the quantum dot absorption while the red and blue lines are the difference between the gold nanoislands with and without the quantum dots. The purple lines represent the approximate change in the gold nanoislands absorption cross-section.

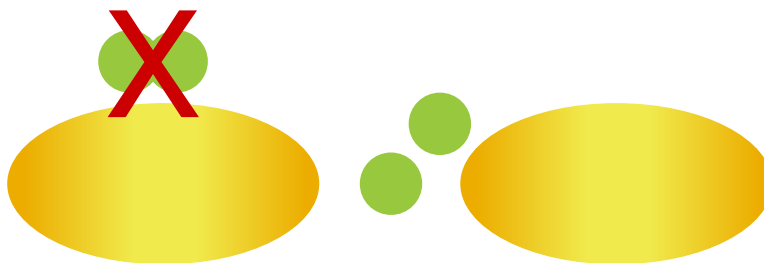


Figure 3.9. An illustration of the density based nanoisland system. The red “X” corresponds to an invalid quantum dot position.

### 3.3.3 Experimental Confirmation Through Changing the Quantum Dot Number Density

A simple way to enhance the working device quantum efficiency is to increase the QDs density on the device surface. Therefore, we model the changes in the plasmon resonance as we change the QDs density. To match the experimental systems, the QD locations were randomized with the number of QDs set via a number density parameter. To place each of the QDs in a cell, a random value for the  $x$ - coordinate was selected and the  $y$ - coordinate set such that the center of the QD is within 4 nm of the surface of the gold nanoparticles. Once placed, the QD was compared with previously placed QDs to avoid overlap between the two QDs. If a single quantum dot failed to find a location after one thousand attempts the neighboring quantum dots were shifted until no conflicts were present. This was repeated until all the QDs were placed in the cell. A schematic of the system is shown in Figure 3.9.

It is clear that the system only reaches a saturation point once the QDs fill the available sites near all the plasmonic hotspots. Figure 3.10 shows scatter plots comparing the calculated change in the red-shift and absorption peak magnitude of nanoellipse dimers with a 10 nm gap after being coupled to a film of CdSe 610 nm QD and Pb S850 nm QDs. At approximately 11 QDs/100 nm, the red-shift due to the CdSe 610 nm and the PbS 850 nm QDs levels off at approximately 23 nm and 1.93 nm respectively. These values are slightly higher than the

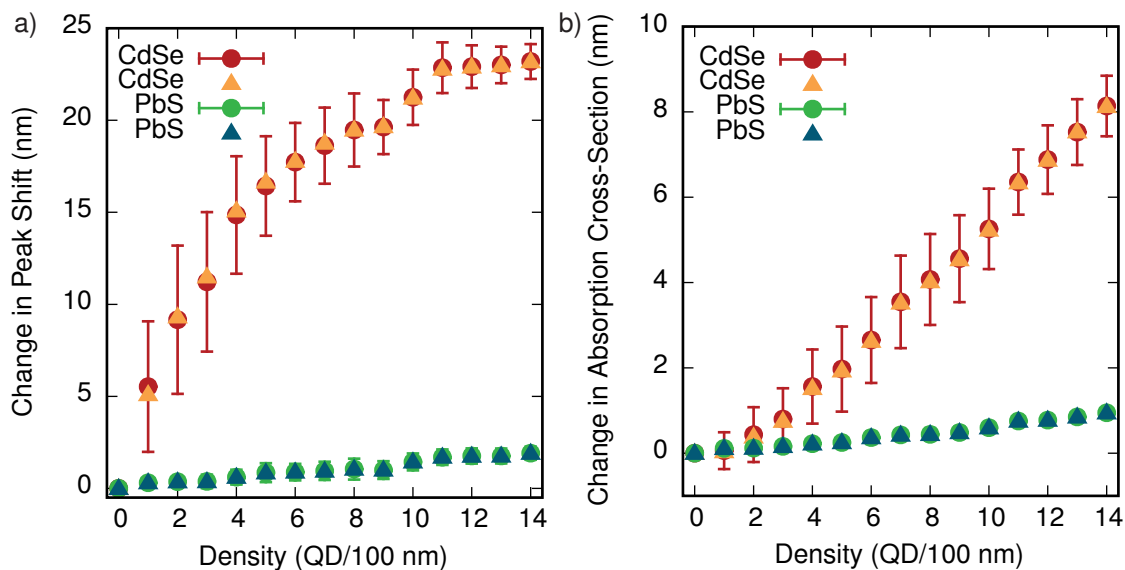


Figure 3.10. A scatterplot showing the simulated change in a) peak wavelength and b) peak height shift with changing quantum dot density. Triangles are from the peak location/value of the mean spectra, and circles are the mean of the peak location/value for all calculations.

shifts seen for a single QD in a 7 nm gap and represent the maximum expected red-shift for the system. Unlike the red-shift, the magnitude of the absorption cross-section does not saturate, as seen in Figure 3.10b. Both QDs show a nearly linear scaling between the magnitude and the QD surface density throughout the entire range tested. The range was not extended further because 14 QDs/100 nm is approximately the density of a complete monolayer. The linear scaling implies that device performance will continue to improve as the QD surface density increases, and should be maximized for achieving efficient photodetectors. The convergence of all calculations is shown in Figure 3.11, where the larger variations for the PbS 850 nm QD is a result of similar numerical errors acting on smaller values.

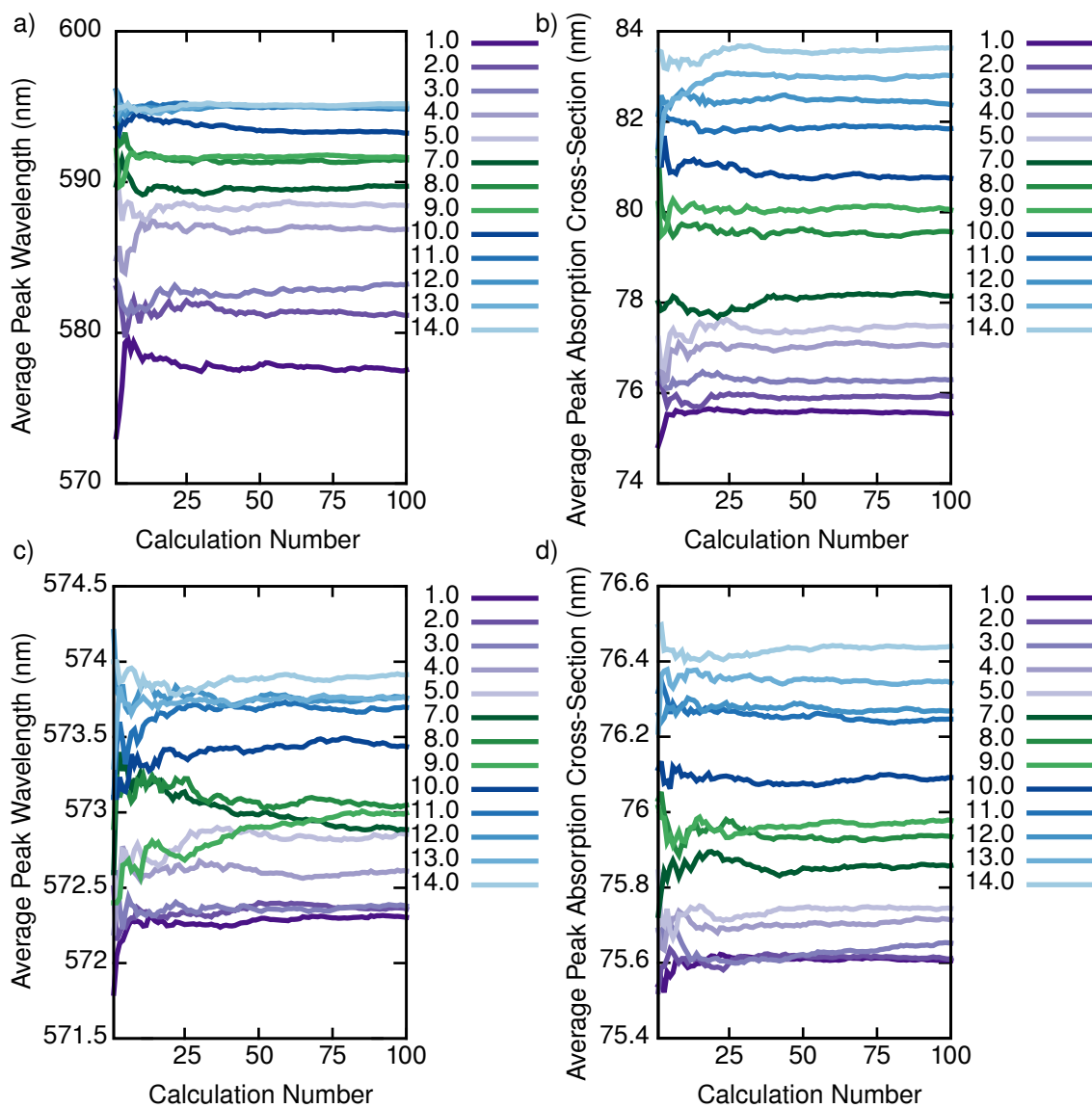


Figure 3.11. Convergence of the density calculations for the CdSe 610 nm QD (a and b) and the PbS 850 nm QD (c and d). The legends are in QDs/100 nm.

The experimentally observed trends agree well with our theoretical predictions. Figures 3.12a and 3.12b show the total extinction spectra of the gold nanoisland films with increasing exposure to the CdSe 610 nm QD and PbS 850 nm QD solutions, corresponding to increasing QD number density. To determine the exact peak characteristics, the spectra in Figures 3.12a and

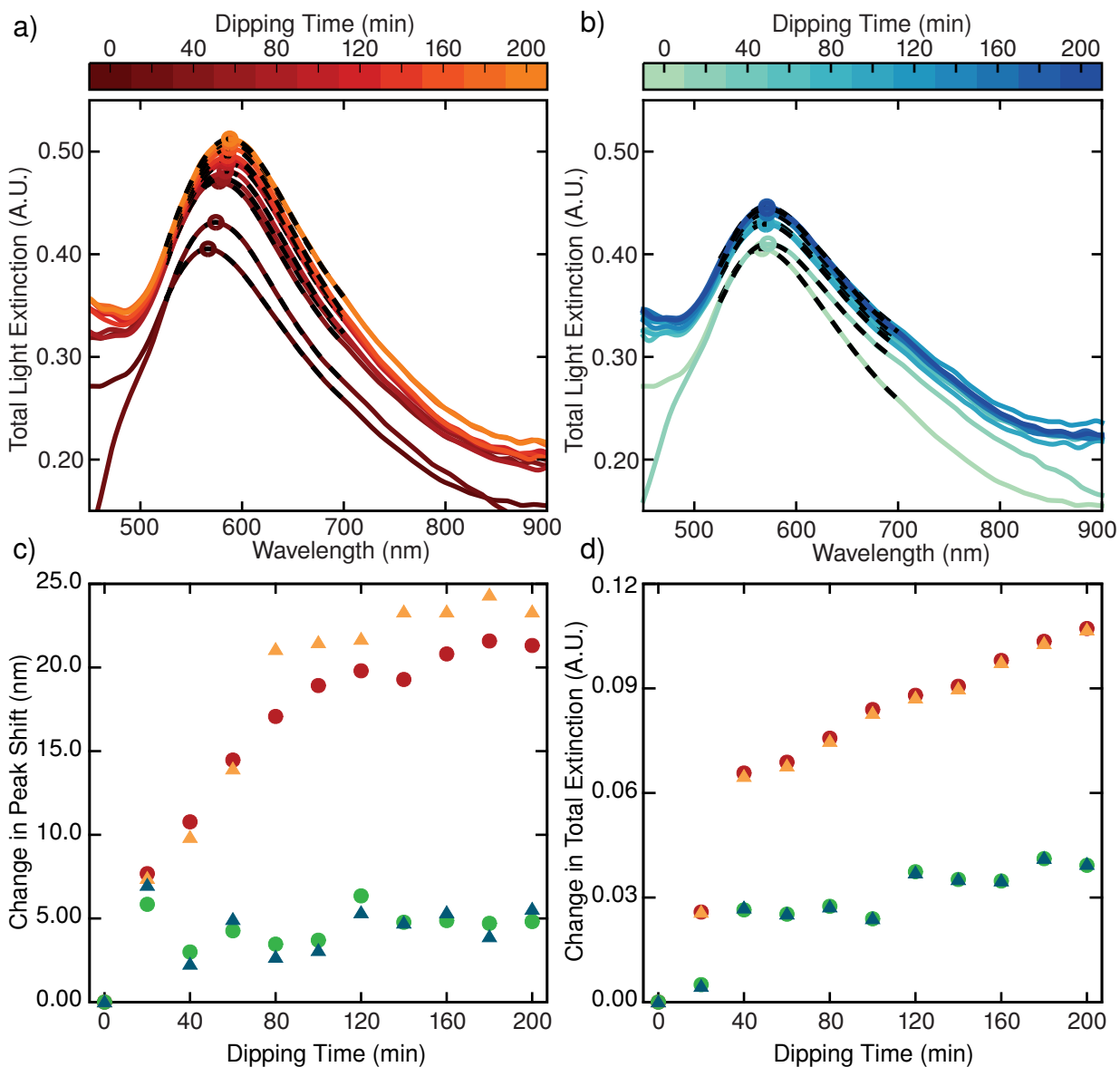


Figure 3.12. Experimental light extinction from the random Au-NPs with different density of a) CdSe 610 nm QDs and b) PbS 850 nm QDs. Solid curves correspond to the smoothed absorption spectra using a Savitzky-Golay filter, dashed curves are a sixth degree polynomial fit used to extract the peak position (marked with a circle) accurately. Scatter plot showing the change in c) red-shift and d) peak extinction against change in CdSe (red and orange) or PbS (blue and green) quantum dot solution exposure time. Triangles are at the maximum of the smoothed spectra; circles are at the maximum of the polynomial fits. The errors of the data are estimated to be less than 4%.

3.12b were smoothed using a Savitzky-Golay algorithm and fitted to a sixth order polynomial. The resulting red-shift and change in total extinction are plotted in Figure 3.12c and Figure 3.12d respectively. The QDs absorption peak follows a linear trend, as predicted by our calculations. The maximum red-shift associated with the CdSe 610 nm QD is 21-24 nm, and for PbS 850 QDs it is about 3-5 nm. While the CdSe 610 nm QDs red-shift is in line with our theoretical prediction, the PbS 850 nm QD is slightly higher than what the simulation predicts. This slight discrepancy could be attributed to our 2-level approximation of the energy spectrum of the QDs, which results in limited absorption near the plasmon resonance for the PbS 850 nm QDs. We would expect an increase of the PbS QDs and gold nanoislands interactions at wavelengths shorter than the main absorption band when including the full quantum dot band structure in the calculation.

The errors of the data presented in Figure 3.12 are estimated to be less than 4%, caused mainly by instability of the white light source and the spectrometer. Each measurement and reference is an average of several measurements taken at different locations around the highly uniform sample.

### 3.4 Conclusions

In this work we suggested self-assembled QDs coupled to a random gold nanoisland film as a design for plasmon-enhanced QD devices. To that end we combined a finite-difference time-domain solution of Maxwell's equation with absorption spectroscopy to investigate the properties of such materials. Using a set of symmetric gold nanoellipse dimers we were able to reproduce the gold nanoislands extinction spectra, suggesting a level of order present in the films. The QDs absorption properties have little effect on the enhancement factor near the plasmon resonance, but tuning the plasmon resonance to the band gap energy can lead to

broadening of the QDs absorption mode. A near linear scaling between the QD density and the absorption cross-section allows maximizing the device performance by increasing the density of QDs. Our results carry implications to the numerical design and optimization of plasmon-enhanced QD devices and, in the longer term, possibly also to several of their applications.

## CHAPTER 4

### **The Maxwell-Liouville Method to Better Model Quantum Emitters**

Coupling quantum emitters to nanoparticles provides the foundation for many plasmonic applications. Including quantum mechanical effects within the calculations can be crucial for designing new devices, but classical approximations are sometimes sufficient. In this chapter we modify the semiclassical Maxwell-Liouville methodology to improve its efficiency, and confirm the implementation's accuracy by calculating the optical properties of a molecular nanosphere and comparing the results against previously published work. We then use these results as a guideline for when to include quantum mechanical effects when modeling the emitters. Finally we extend the algorithm to include inhomogeneous broadening and use it to study the photon echoes from quantum dots.

Manuscript in preparation

## 4.1 Introduction

Correctly modeling all aspects of a quantum emitters' optical properties remains an open challenge within plasmonics. Many plasmonic applications, such as solar cells,<sup>105–108</sup> photodetectors,<sup>24,25,27,109,110</sup> and plasmon enhanced spectroscopy<sup>110–116</sup> rely on coupling molecular layers or quantum dots to metal nanoparticles and measuring their optical response to the plasmonically enhanced fields. Classical methods can describe the interactions to a point, but as the coupling strength increases quantum mechanical effects become more prevalent.<sup>117,118</sup> Quantum chemical approaches have been applied to a subset of these problems, but they focus on single dipole moments or fail to include the effects of the quantum emitters on the plasmonic fields.<sup>119–123</sup>

In this work we modify the Maxwell-Liouville method (ML) first developed by Sukharev and Nitzan,<sup>58</sup> to include inhomogeneously broadened states with an arbitrary distribution.<sup>61,102,124–127</sup> We first present modifications to their methodology to improve the method's efficiency. Then the implementation is used to model the optical response of a molecular sphere, and the results are compared against previously published work.<sup>58</sup> We then describe the Maxwell-Liouville method, and the modifications used to model inhomogeneously broadened states. Finally the implementation is used to approximate the photo echo response of a quantum dot, and the results are compared against analytical models developed by Poltavtsev et al.<sup>128</sup>

## 4.2 Methodology

### 4.2.1 Maxwell-Liouville Propagator

The ML algorithm modifies FDTD by using a Liouville-von Neumann propagator to quantum mechanically calculate the polarization of quantum emitters

$$(4.1) \quad \mathbf{P} = n_e \text{Tr}[\hat{\rho} \hat{\boldsymbol{\mu}}],$$

where  $n_e$  is the emitter's number density,  $\hat{\rho}$  is the emitter's density operator,  $\hat{\boldsymbol{\mu}}$  is the emitter's dipole operator, and Tr is the trace operator. The density matrices are propagated in time using the Liouville-von Neumann operator,  $\mathcal{L}$ ,

$$(4.2a) \quad i\hbar \frac{d\hat{\rho}}{dt} = \mathcal{L} \hat{\rho} = [\hat{H}, \hat{\rho}] - i\hbar \hat{\Gamma} \hat{\rho},$$

$$(4.2b) \quad \hat{H} = \hat{H}_0 - \hat{\boldsymbol{\mu}} \cdot \mathbf{E}(t),$$

where  $\hbar$  is the reduced Plancks constant,  $\hat{H}$  is the Hamiltonian of an emitter with dipole moment  $\hat{\boldsymbol{\mu}}$ ,  $[\hat{A}, \hat{B}]$  is the commutator of operators  $\hat{A}$  and  $\hat{B}$ , and  $\hat{\Gamma}$  is the relaxation operator in the Lindblad form.<sup>129</sup> Equation 4.2a is solved numerically with a predictor-corrector propagator based on the fourth order Adams-Bashforth predictor and the fourth order Adams-Moulton corrector,

$$(4.3a) \quad \hat{\rho}_{predict}^{n+1} = \hat{\rho}^n + \Delta_t \left( \frac{55}{24} \mathcal{L}^n \hat{\rho}^n - \frac{59}{24} \mathcal{L}^{n-1} \hat{\rho}^{n-1} + \frac{37}{24} \mathcal{L}^{n-2} \hat{\rho}^{n-2} - \frac{9}{24} \mathcal{L}^{n-3} \hat{\rho}^{n-3} \right)$$

$$(4.3b) \quad \hat{\rho}^{n+1} = \hat{\rho}^n + \Delta_t \left( \frac{9}{24} \mathcal{L}^{n+1} \hat{\rho}_{predict}^{n+1} + \frac{19}{24} \mathcal{L}^n \hat{\rho}^n - \frac{5}{24} \mathcal{L}^{n-1} \hat{\rho}^{n-1} + \frac{1}{24} \mathcal{L}^{n-2} \hat{\rho}^{n-2} \right),$$

where the values of  $\mathcal{L} \hat{\rho}$  at the three preceding time steps are stored in memory.

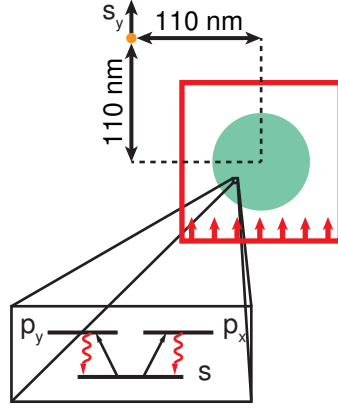


Figure 4.1. Schematic of the test cell. The red box is the TFSF boundary, the green circle is the emitters, and the inset represents the electronic structure of the emitters

#### 4.2.2 Inhomogeneously Broadened States

Inhomogeneously broadened systems are created by replicating the density matrices  $N$  times, and setting the energy of the broadened states to  $\hbar\omega_n = \hbar(\omega_{min} + n\frac{\omega_{max}-\omega_{min}}{N-1})$ , where  $\omega_{min}$  and  $\omega_{max}$  are the transition frequencies from the ground state to the lowest and highest broadened state, respectively, and  $n$  is some integer less than  $N$ . Each emitter has an initial ground state population defined by some normalized distribution  $g(\omega_n)$ . The total polarization vectors are then found by summing together all individual emitter polarizations

$$(4.4) \quad \mathbf{P} = \sum_{n=1}^N n_e \text{Tr}[\rho_n \hat{\boldsymbol{\mu}}].$$

## 4.3 Results

### 4.3.1 Scattering from a Molecular Sphere

The initial test system for the ML implementation is a nanoparticle, with a radius of 25 nm, made of emitters as shown in Figure 4.1. The atoms have a ground state  $s$  orbital and two excited state  $p$  orbitals 3.1 eV higher in energy with a dipole moment of 25 D and a radiationless decay lifetime of 1 ps. The  $y$ -component of the Poynting vector at a point 156 nm away from the center of the nanoparticle measures the scattering response of the emitters. The results for the test calculations agree with those reported by Sukharev and Nitzan.<sup>58</sup>

Figure 4.2a shows the optical scattering spectrum for the atoms, upon changing the emitter density. There are two peaks in the spectra, a weak peak that is slightly red-shifted from the transition frequency and a stronger, broader peak at a higher energy. As the density increases the higher frequency peak blue-shifts, with an increasing intensity that diverges from the Clausius-Mossotti approximation, which describes the classical dielectric response for atomic and non-polar molecular material. Divergence from the Clausius-Mossotti approximation is indicative of quantum mechanical effects.<sup>3</sup> Scaling these results for different  $\hat{\mu}$  and  $n_e$  can give an approximate guide to when classical approximations will fail and quantum mechanical corrections need to be added.

An advantage ML has over other methods is its ability to model the dephasing behavior of quantum emitters. Figure 4.2b shows the optical response of the system with changing dephasing rate. As the dephasing rate decreases the peak at the atomic transition frequency becomes narrower and increases in intensity. The numerical noise in the spectrum without pure dephasing ( $\gamma_p = 0$ ) is from a lack of convergence of the electromagnetic fields, which can be fixed by going to a finer step size.

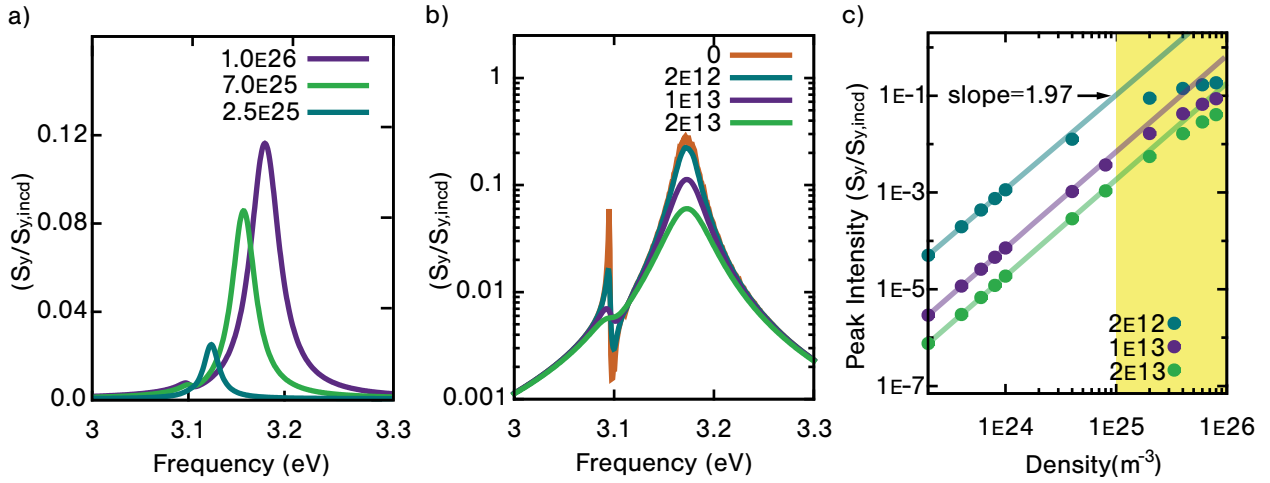


Figure 4.2. (a) Scattering intensity at different emitter densities, with  $\gamma_p = 1 \times 10^{13}$  (b) Scattering intensity at different dephasing rates with  $n_e = 1 \times 10^{26}$  (c) Scattering Intensity of the high frequency resonance as a function of density on a double log scale

A final benchmark shows the quantum emitters' effects on plasmonic fields. The test system in this case is a silver nanoparticle, with a 40 nm diameter, covered by a 10 nm layer of emitters. The emitters have the same electronic structure as the previous system, but with an energy difference of 3.61 eV, a radiationless decay lifetime of 1.0 ps, a dephasing rate of  $10^{13} \text{ s}^{-1}$ , a density of  $2.5 \times 10^{25} \text{ m}^{-3}$ , and a dipole moment of 25 D. As shown in Figure 4.3b, the LSPR peak of the silver nanoparticle is slightly red-shifted as a result of changing the dielectric environment. More importantly, an additional peak at the atomic transition resonance grows in, which is a result of strong coupling between plasmonic and emitter modes.

To test the distance dependence of the coupling between the emitters and metal nanoparticles, a 2 nm  $\text{TiO}_2$  layer is added between the molecules and silver nanoparticle. The 2 nm thickness is chosen because it is the minimal thickness needed to protect the metal nanoparticle from etching in electrolyte solutions.<sup>130</sup> Including the dielectric layer is shown to have a minimal impact on the scattering response of the particles, with the LSPR further red-shifting

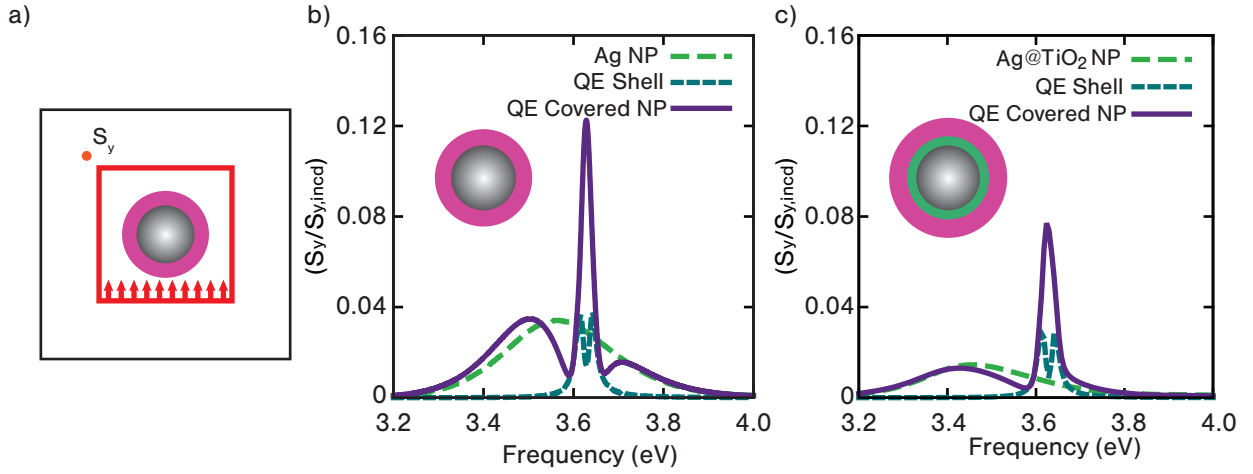


Figure 4.3. (a) Diagram of the emitter coated Ag nanoparticle cell. The red box is the TFSF boundary, the pink coating is the emitter layer, the silver is the silver nanoparticle, (b) Scattering Intensity for the QE coated NP, with the inset showing the particle (c) Scattering Intensity for the QE coated with a 2 nm  $\text{TiO}_2$  layer between the silver and QE layer. The inset shows the particle structure with the green layer representing the  $\text{TiO}_2$ .

and the scattering intensity decreasing. This result is important for certain applications such as dye-sensitized solar cells where the molecular layer is separated from the nanoparticles.

### 4.3.2 Photon Echoes From Inhomogeneously Broadened states

To confirm the validity of the inhomogeneous broadening algorithm the photon echo signal from a quantum dot is numerically calculated and compared against analytical results published by Poltavtsev, et al.<sup>128</sup> Photon echoes occur when an inhomogeneously broadened system is initially excited by a pulse at a time,  $t_1$ , and then excited again by a  $\pi$  pulse at a time,  $t_1 + \tau$ . The  $\pi$  pulse reverses the motion of the emitters' Bloch vectors, restoring the initial polarization state and generating an echo pulse at a time  $t_1 + 2\tau$ .<sup>131</sup> The quantum dots are treated as a broadened two level system, where the transition frequency is determined by a Gaussian distribution

$$(4.5) \quad g(\omega_n) = \frac{1}{A_0} e^{-\frac{(\omega_n - \omega_0)^2}{2\delta_0^2}},$$

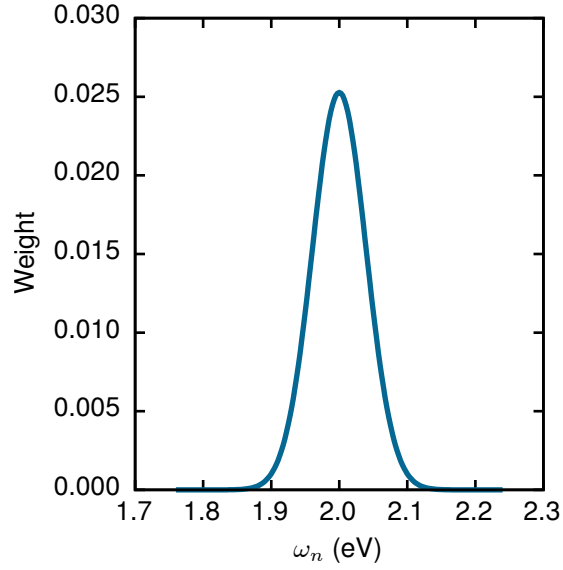


Figure 4.4. The distribution of quantum emitters in the system

where  $\omega_0$  is the center frequency of the band,  $\delta_0$  is the band width of the distribution and  $A_0$  is a normalization factor equal to

$$(4.6) \quad A_0 = \sum_{n=0}^N e^{-\frac{(\omega_n - \omega_0)^2}{2\delta_0^2}}.$$

The system is excited by two rectangular pulses of width,  $\tau_p$ , and separated by a time of  $\tau_{12}$ . Poltavtsev et al. demonstrated the polarization associated with the photon echo,  $P_{PE}$ , can be obtained from the off diagonal elements of  $\hat{\rho}$ , which is proportional to,

$$(4.7) \quad |P_{PE}(t')| \propto \left| \int_{-\infty}^{\infty} \exp\left(-\frac{\Delta^2}{2\delta_0^2}\right) \frac{\Omega_1 \Omega_2^2}{\tilde{\Omega}_1 \tilde{\Omega}_2^2} \sin^2 \frac{\tilde{\Omega}_2 \tau_p}{2} \left[ \frac{2\Delta}{\tilde{\Omega}_1} \sin^2 \frac{\tilde{\Omega}_1 \tau_p}{2} \sin \Delta t' + \sin \tilde{\Omega}_1 \tau_p \cos \Delta t' \right] d\Delta \right|,$$

where  $\Delta = \omega - \omega_n$ ,  $\omega$  is the angular frequency of the rectangular pulse set to  $\omega_0$ ,  $\Omega_1$  and  $\Omega_2$  are the area under the first and second pulse respectively, and  $\tilde{\Omega} = \sqrt{\Omega^2 + \Delta^2}$ .<sup>128</sup>

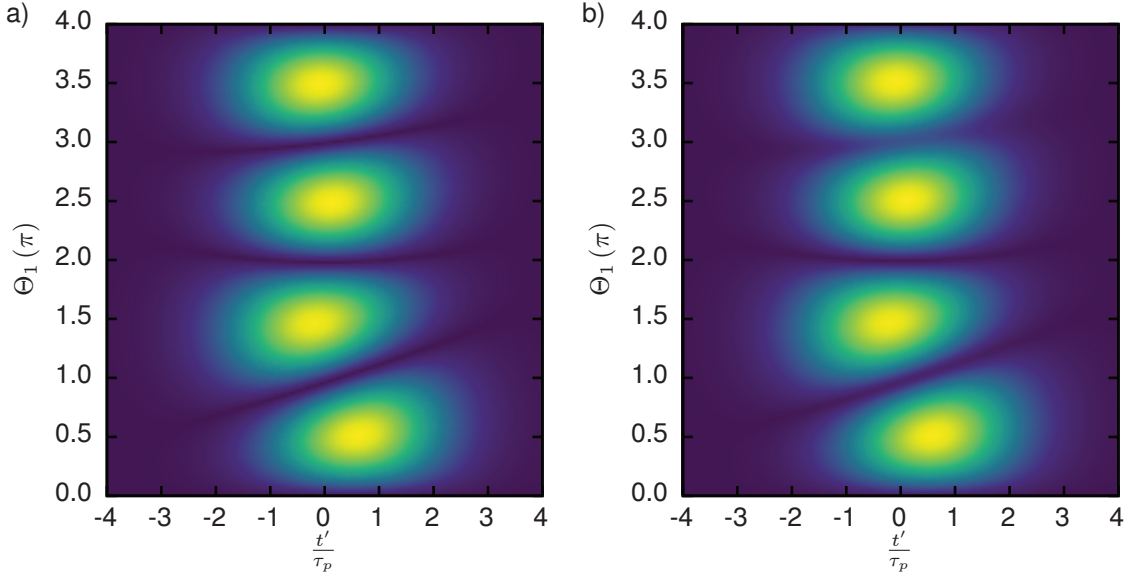


Figure 4.5. A comparison of the a) analytical and b) numerical photon echo of the inhomogeneously broadened quantum dots. The  $x$ -axis is a normalized time unit, the  $y$ -axis is the area under the first pulse ( $\Omega_1 \tau_p$ ) and the map corresponds the the value of  $\rho_{01}$  or the off diagonal density matrix element.

Because only the difference between the pulse and the oscillators is important,  $\hbar\omega_0$  is set to 2 eV,  $\hbar\delta$  is set to 0.1142 eV, and the oscillators are sampled from 1.76 to 2.24 eV, with an interval of 2.5 meV. Figure 4.4 shows  $g(\omega_n)$  for the quantum dots. The system is excited by two rectangular pulses approximated by,

$$(4.8) \quad E = E_0 \frac{1}{\left(\frac{t-t_0}{\tau_p}\right)^n + 1} e^{i\omega(t-t_0)},$$

where  $E_0$  is the field intensity,  $t_0$  is the center time, and  $\omega$  is the frequency of the pulse, and  $n$  describes the shape of the pulse. For these calculations the pulse width is 5.76 fs and  $n$  is 500. The oscillators are located at a single point in the center of the one dimensional cell that has a 10 unit cell convolution perfectly matched layer (CPML) on both sides, a step size of 1 Å, and a time step of 0.1667 as.

Figure 4.5 compares the analytical and numerical photon echo response. Both sets of calculations are in good agreement with each other, with slight disagreements that increase as  $\Theta_1$  increases. For all numerical calculations, the minimum value of  $P_{PE}$  is never perfectly zero because the  $\pi$  pulse does not perfectly invert the population. As  $\Theta_1$  increases the rectangular pulse and therefore final state populations also increases, resulting in a less accurate photon echo response. Properly normalizing Equation 4.7 would lead to quantitative agreement between numerical and analytical results. These results demonstrate that the numerical methodology is capable of replicating the abnormal photon echo timing seen in the experiments of Poltavtsev et al.<sup>128</sup>

#### 4.4 Conclusion

We demonstrate the applicability of the ML method for modeling the optical response of quantum dot and molecular species. After describing slight improvements to the ML algorithm, the optical properties of a molecular nanosphere are calculated and compared against previously published results. These results suggest that if a molecular medium has a low number density or a weak transition dipole moment, then it can be treated classically with minimal error. Finally the methodology is then extended to include inhomogeneous broadening, and used to investigate the photon echoes of quantum dots. This method can be applied to other systems where quantum mechanical effects are important for studying their optical properties.

## CHAPTER 5

**Determining the Molecular Dipole Orientation on Nanoplasmonic Structures**

We develop a theoretical method to investigate the effects of the orientation of a molecular monolayer on plasmonic systems. Molecular layers strongly alter the plasmonic resonance of nanoparticles, affecting their ability to couple to other nanoparticles and quantum emitters. Understanding how the coating impacts the optical properties of the nanostructures is critical for the application of plasmonics in areas such as light detection, sensing, and plasmon-enhanced solar energy conversion. We extend the three-dimensional finite-difference time-domain method to molecular layers with induced dipoles at an arbitrary orientation relative to the nanostructures surface. Numerical calculations show how the orientation of molecular dipoles affects the plasmon resonance of both tetrahedral and ellipsoidal nanoparticles. Finally, we demonstrate how the layer impacts the coupling between ellipsoidal nanoparticles and a colloidal quantum dot.

This chapter has been reproduced with permission, from Ref 183

## 5.1 Introduction

Understanding the effects of the molecular dipole orientation of a monolayer on its coupling to metal nanostructures remains a challenge for molecular plasmonics. The dipole orientation of molecular coatings has been shown to affect not only the molecular vibrational,<sup>132–134</sup> optical,<sup>44, 135–139</sup> chiroptical,<sup>54, 140</sup> bioactivity,<sup>34, 35, 141, 142</sup> and electron transport properties,<sup>136</sup> but also the plasmon resonance of the nanoparticles.<sup>137, 143, 144</sup> Controlling the changes in molecular and plasmonic properties is vital for the use of plasmonic particles in solar cell<sup>138, 144–146</sup> and sensing applications.<sup>34, 147, 148</sup> Of particular interest is the coupling between plasmons and J-aggregate films.<sup>44–51</sup> Recent experimental and theoretical studies have shown that in a strong coupling regime hybrid molecular-plasmonic modes appear with highly controllable resonances.<sup>44–46</sup> Even outside the strong coupling regime, physically relevant processes such as enhanced absorption and exciton induced transparency occur at weaker coupling strengths.<sup>45, 52</sup> Modifying molecular properties such as width, oscillator strength, or orientation has been shown to be a potentially attractive way of obtaining the desired optical properties in model systems.<sup>51, 55</sup> Developing a methodology to extend these studies to an arbitrary system would provide many physical insights.

A key challenge in modeling plexcitonic systems is incorporating oriented molecular dipole moments within the systems actual geometry. Traditional approaches treat the molecular layer isotropically, neglecting the directionality of the dipole moments.<sup>45, 46, 51</sup> Combined experimental and theoretical work demonstrated that this approximation can overestimate the molecular interactions seen in the system.<sup>49</sup> Whereas analytical descriptions for idealized systems have been created,<sup>54–57</sup> here we supply a general approach for all system geometries and orientations.

In this work we propose a new methodology to calculate the optical properties of oriented molecular monolayers for a generalized set of nanoplasmonic structures. By extending FDTD to include molecular dipoles at any orientation relative to a surface, this method can be applied to an arbitrary nanoparticle system. After developing the theoretical methodology we compare computational results of molecularly coated tetrahedral particles with experimental results reported by Haes and coworkers.<sup>143</sup> Next, we explore how a molecular monolayer affects the optical properties of gold metal nanoisland films using a dimer model previously shown to qualitatively describe the system.<sup>103,149,150</sup> Finally, we study how the layer impacts the coupling between the films and a quantum dot monolayer through a model system.

## 5.2 Methodology

The molecular layer is treated anisotropically by replacing the permeability and permittivity scalars with tensors. The molecules are assumed to be magnetically inactive, allowing the permeability tensor to be set to the identity matrix. The permittivity tensor,  $\bar{\bar{\epsilon}}$ , for the molecules is approximated as,

$$(5.1) \quad \bar{\bar{\epsilon}} = \bar{\bar{\epsilon}}_{\infty} + \frac{8\pi}{\hbar} n_m \sum_{m=1}^n \frac{\boldsymbol{\mu}_m \otimes \boldsymbol{\mu}_m \omega_l}{\omega_l^2 + \Gamma_l^2 - \omega^2 + 2i\Gamma_l \omega}$$

where  $\hbar$  is the reduced Planck constant;  $n_m$  is the number density of the molecules;  $n$  is the number of modes; and  $\boldsymbol{\mu}_1$  is the transition dipole moment,  $\omega_l$  is the center frequency, and  $\Gamma_l$  is the linewidth of the  $l^{\text{th}}$  transition.<sup>54,151</sup> ADE is used to incorporate the materials dielectric response, modifying Equation 1.3a,

$$(5.2) \quad \mathbf{D} = \epsilon_0 \epsilon_{\infty} \mathbf{E} + \mathbf{P}_{\text{Metal}} + \mathbf{P}_{\text{Molecule}}$$

where in the frequency domain  $\mathbf{P}_{\text{Metal}}$  and  $\mathbf{P}_{\text{Molecule}}$  are

$$(5.3a) \quad \check{\mathbf{P}}_{\text{Metal}} = \varepsilon \check{\mathbf{E}},$$

$$(5.3b) \quad \check{\mathbf{P}}_{\text{Molecule}} = \bar{\varepsilon} \check{\mathbf{E}}.$$

The metallic and molecular polarization density fields are then inverse Fourier transformed and all derivatives are expanded with a central difference operator to update the fields forward in time. The update equation is demonstrated for the  $x$ -component of the  $m^{\text{th}}$  molecular polarization field at grid point  $(i, j, k)$  by,

$$(5.4) \quad P_{i,j,k}^{n+1} = \frac{2 - (\omega_l^2 + \Gamma_l^2) \Delta_t^2}{\Gamma_l \Delta_t + 1} P_{i,j,k}^n + \frac{\Gamma_l \Delta_t - 1}{\Gamma_l \Delta_t + 1} P_{i,j,k}^{n-1} + \frac{4\pi n_m \omega_l \Delta_t^2}{\hbar (\Gamma_l \Delta_t + 1)} \mu_{m,x} (\boldsymbol{\mu}_m \cdot \mathbf{E}_{i,j,k})$$

where  $\Delta_t$  is the time step used for the calculation. See Equation 2.8 for the update equation of metallic materials. To facilitate the calculation of  $\boldsymbol{\mu}_1 \cdot \mathbf{E}_{i,j,k}$  the molecular dipole moments are stored on the corners of the FDTD unit cell, dislocated from the electric field components as shown in Figure 5.1. The values of  $\mathbf{E}_{i,j,k}$  and  $\mathbf{P}_{i+\frac{1}{2},j,k}$  are obtained by averaging the fields at adjacent grid points, for example

$$(5.5a) \quad E_{i,j,k}^x = \frac{1}{2} \left( E_{i+\frac{1}{2},j,k}^x + E_{i-\frac{1}{2},j,k}^x \right)$$

$$(5.5b) \quad P_{i+\frac{1}{2},j,k}^x = \frac{1}{2} \left( P_{i+1,j,k}^x + P_{i,j,k}^x \right)$$

and the full unit cell is shown in Figure 5.1.

The molecular layer is treated as a set of transition dipole moments oriented at a polar angle,  $\theta$ , relative to the normal vector,  $\mathbf{n}$ , of the nanoparticles surface. At all grid points within the

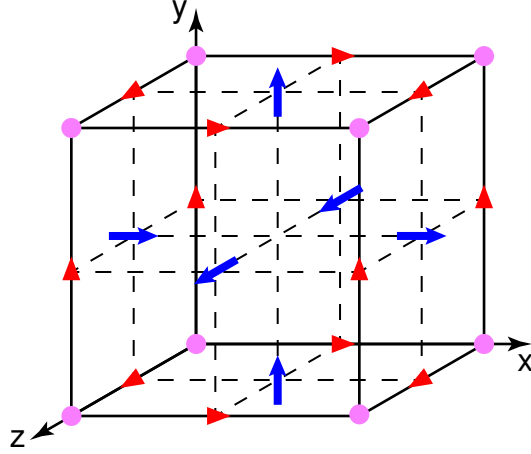


Figure 5.1. Unit cell for FDTD calculations including oriented dipole moments. The electric field components are located on the edges of the cell and represented by red triangles (the component of the field is in the direction of the longer dimension). The magnetic field components are stored on the faces of the cell and represented by blue arrows (the component represented by the direction of the arrow). The pink circles represent the molecular dipoles and all three components are individually stored there.

molecular layer, the surface normal of the nanostructures is calculated by

$$(5.6) \quad \mathbf{n} = \frac{\nabla \mathcal{F}(x, y, z)}{|\nabla \mathcal{F}(x, y, z)|}$$

where  $\mathcal{F}(x, y, z)$  describes the surface of the nanoparticles. The longitudinal and latitudinal tangent vectors,  $\mathbf{t}_{\text{Long}}$  and  $\mathbf{t}_{\text{Lat}}$ , are calculated from the  $\mathbf{n}$  by rotating the polar angle of  $\mathbf{n}$  by  $90^\circ$  and taking the cross product between  $\mathbf{n}$  and  $\mathbf{t}_{\text{Long}}$ . Once the rotated coordinate axes are established the molecular dipole moment is then calculated as

$$(5.7) \quad \boldsymbol{\mu}_{\mathbf{m}} = |\boldsymbol{\mu}_{\mathbf{m}}| (\cos \theta \mathbf{n} + \sin \theta \cos \phi \mathbf{t}_{\text{Long}} + \sin \theta \sin \phi \mathbf{t}_{\text{Lat}}),$$

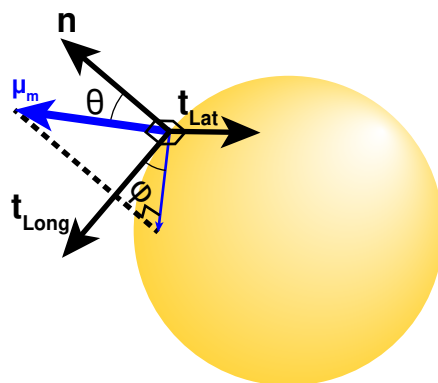


Figure 5.2. Schematic showing how  $\mu_1$  is calculated from the surface normal of a nanoparticle.

where  $\theta$  and  $\phi$  are the polar and azimuthal angles defined in Figure 5.2. For all calculations,  $\phi$ , is assumed to be  $45^\circ$ .

## 5.3 Results

### 5.3.1 Modifying the LSPR of Tetrahedral Nanoparticles with Molecular Coatings

The first system modeled is a set of identical truncated silver tetrahedra coated with a 2 nm molecular layer. Haes, et al. previously demonstrated that the optical coupling between truncated silver tetrahedra and a  $\text{Fe}(\text{bpy})_3^{2+}$  monolayer can be accurately described by only accounting for the 520 nm mode, neglecting the mode at 490 nm.<sup>143</sup> The authors attributed the weak coupling between the 490 nm resonance and the silver tetrahedra to low spatial overlap between the modes transition dipole moment and the plasmonically enhanced fields. To confirm their hypothesis a molecular monolayer was added to a truncated silver tetrahedron with a perpendicular bisector of 90 nm (side length of 103.9 nm) and a height of 55 nm. Then the

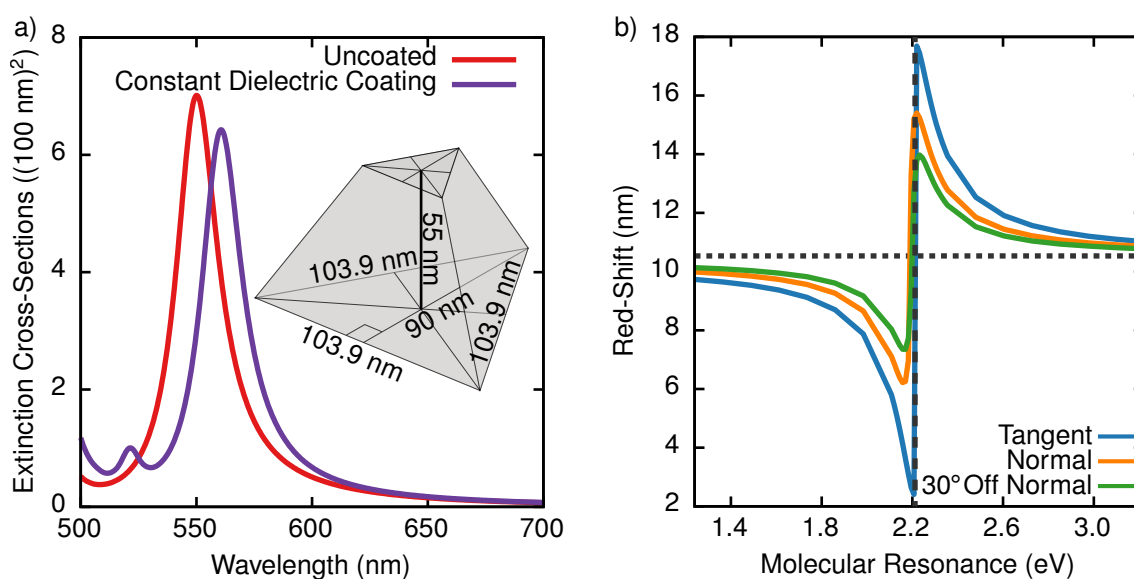


Figure 5.3. a) Extinction spectrum of a silver truncated tetrahedron with a perpendicular bisector of 90 nm and a height of 55 nm, with and without a 2 nm coating of a constant dielectric material with a relative permittivity of 1.2. Inset shows a schematic of the uncoated tetrahedron b) LSPR red-shift caused by the molecular coating vs. the energy of the molecular excitation. The horizontal dashed line is the red-shift caused by the constant dielectric coating and the vertical line is the energy of the plasmon resonance of the tetrahedron, coated with the constant dielectric layer.

LSPR red-shift is tracked against the excitation energy of the molecular mode,  $\omega_0$ , for various dipole orientations. The linewidth, dipole moment, and number density of the monolayer are held at  $1040 \text{ cm}^{-1}$ , 1.1 D, and  $\frac{\omega_0}{2.38 \text{ eV}} 5 \times 10^{26} \frac{\text{molecules}}{\text{m}^3}$  respectively, approximating the 520 nm excitation of  $\text{Fe}(\text{bpy})_3^{2+}$ . The molecular density is scaled by the ratio of the shifted excitation energy and actual excitation to ensure a consistent peak absorption. The number density was chosen to model a full monolayer but can be lowered to model submonolayer surface coverage. The molecular layer is also assumed to have a relative high frequency dielectric constant of 1.2 to model the off-resonance red-shift seen experimentally.

Figure 5.3a displays the calculated extinction spectrum of the tetrahedral particles, with and without a constant dielectric layer. The spectra are in good agreement with their experimental counterparts with the main plasmon resonance centered at 550 nm compared with the 560.2 nm reported by Haes, et al.<sup>143</sup> The small error in describing the LSPR of the tetrahedron is the result of approximations to both the dielectric function and the geometry of the silver nanoparticles. Treating the molecular layer as a constant dielectric material with a relative permittivity of 1.2 results in a 10.5 nm red-shift. We define this shift as the base red-shift induced by the molecular layer. Including the molecular resonance in the calculations produces similar results to the ones shown by Haes, et al., with the LSPR red-shift suddenly increasing as the plasmon moves to the red of the molecular excitation, as seen in Figure 5.3b.<sup>143</sup> The red-shift is controlled by the real part of the molecular layers refractive index, and the dipole orientation modulates the magnitude of the interaction by changing the spatial overlap between the dipoles and the plasmonic field. Tangentially oriented molecules have the highest overlap with the plasmonic fields and therefore the largest variation in the red-shift, over twice the shift caused by molecular dipoles with a  $\theta$  of  $30^\circ$ . The results suggest that the effects from the 490 nm mode are drowned out by the 520 nm mode due to differences in the orientation of their respective transition dipole moments.

### **5.3.2 The Effects of Linker Molecules on the Coupling Between Quantum Dots and Nanoisland Films**

Similar molecular orientation effects can also be seen in randomly generated plasmonic substrates. To understand the effect of the linker molecules on the spectra of gold metal nanoisland films, a symmetric gold nanoellipsoid dimer is used to model the full films. While quantitative agreement is not expected, it has been previously shown that this model can qualitatively probe all relevant physical processes.<sup>103,149</sup> The dimers are coated with a 2.5 nm molecular layer,

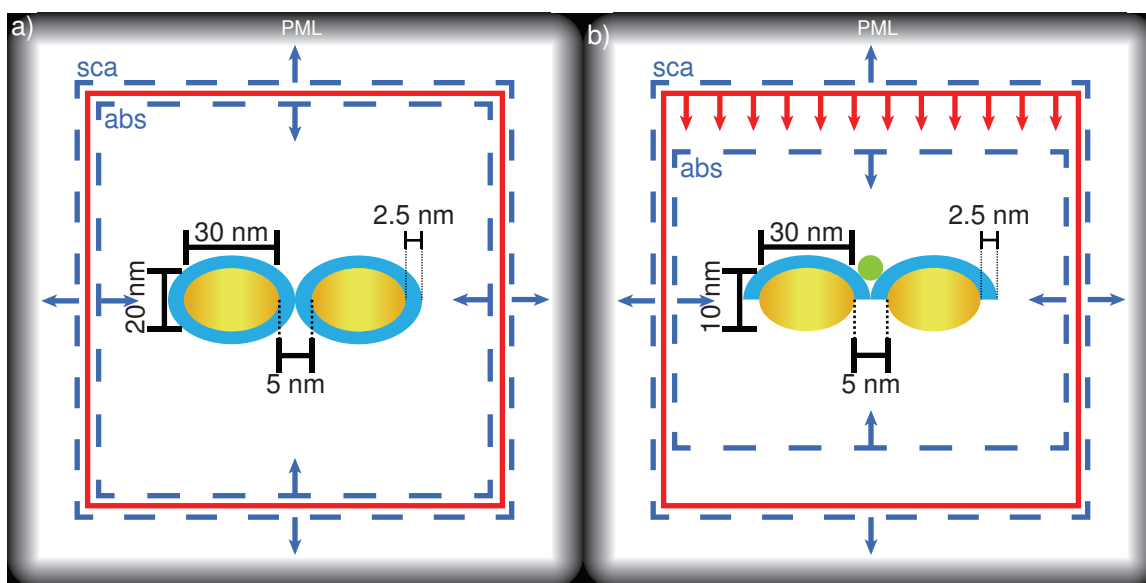


Figure 5.4. Cell diagram for the calculation in the a)  $xy$ - and b)  $xz$ - planes. The green ball represents the quantum dot, the blue arc is the molecular layer, and the gold ellipsoids are the nanoparticles. The system is excited from above by a TF/SF surface (red), and the absorption and scattering fluxes are calculated over a box 6 nm inside and outside the TF/SF surface respectively. The cell has 50 unit cell thick PML regions at the boundary.

whose transition dipole moments are oriented at various angles from the surface normal. The molecules all have a transition dipole moment of 2.5 D, a line width of  $2000 \text{ cm}^{-1}$ , an excitation wavelength of 300 nm or 588 nm, and a varying molecular density. For a 2.5 nm thick film  $10^{26} \frac{\text{molecules}}{\text{m}^3}$  represents a full monolayer for a molecule with a contact area of  $4 \text{ nm}^2$  on the nanoparticle surface. To calculate the molecular density needed to model a complete monolayer of a material, divide Avogadro's number by its molar volume. Figures 5.4a and 5.4b illustrate sample cell maps for the system for the center  $xy$ - and  $xz$ - planes. The cell comprises of two gold nanoellipsoids separated by a gap of 5 nm and  $x$ -,  $y$ -, and  $z$ - axis lengths of 30 nm, 20 nm, and 10 nm respectively. The system is excited from above with a TF/SF surface shown in red with a linearly polarized Gaussian pulse with a polarization angle  $45^\circ$  from the  $x$ -axis and

a center frequency of 480 THz and a width of 1.11 fs. The absorption and scattering fluxes are calculated over surfaces 6 nm inside and outside the TF/SF surface respectively shown in blue. The cell is surrounded by a 50 unit cell thick PML to absorb all outgoing light.

Before looking at the optical properties of the dimer systems, we investigate a coated gold nanoellipsoid monomer system. Figure 5.5 tracks the changes in the plasmon resonance due to alterations in the induced dipole orientation of an off and on-resonant monolayer. The on-resonance molecules have a peak wavelength of 588 nm and a molecular density of  $1.96 \times 10^{26} \frac{\text{molecules}}{\text{m}^3}$ , while the off-resonance molecules are centered at 300 nm with a density of  $10^{26} \frac{\text{molecules}}{\text{m}^3}$ . The layers have a different density to ensure the peak extinction is the same for both layers. The bare ellipsoids have a base plasmon resonance at 559 nm with an extinction cross-section of  $371 \text{ nm}^2$ . Figure 5.5a shows the extinction spectra of the ellipsoids coated with the molecular layer perpendicular (i) and parallel (ii) to the surface. Consistent with the results seen for the tetrahedral particles, the on-resonance molecules have a significantly larger effect on the nanoellipsoid with a larger range for both the peak shift and the change in peak extinction than the off-resonance case. The off-resonance molecules act as a dielectric layer with the spatial overlap between the induced dipoles and the plasmonic fields determining the strength of the interaction and the degree of the shift. Unlike the tetrahedral model, the tangential orientation has the weakest interaction with the nanoparticles as there are no sharp corners or edges to support plasmonically enhanced fields tangential to the nanoparticle surface. In fact, for ellipsoidal particles the tangential molecules partially screen the plasmon resonance leading to a slight decrease in peak extinction. This is confirmed in Figure 5.5b where both the red-shift and the change in peak extinction monotonically decrease to the bare gold nanoellipsoid values.

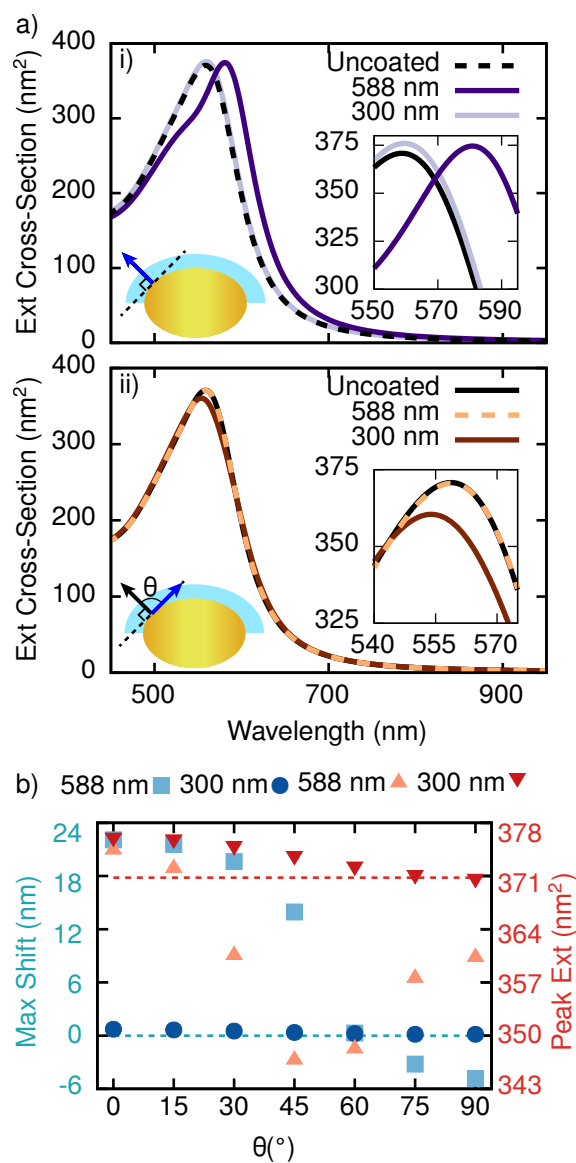


Figure 5.5. a) The absorption spectra of i) normally and ii) tangentially oriented molecules relative to the gold nanoellipsoid surfaces. The molecular resonances are on ( $\lambda_0 = 588$  nm) and off-resonance ( $\lambda_0 = 300$  nm) with the LSPR. b) Peak shifts (blue squares and circles) and maximum extinction cross-sections (red triangles) of the coated nanoellipsoid dimers with varying degrees of alignment to the surface normal. Insets illustrate the orientation of the molecules relative to the nanoparticle surface.

The dipole orientation also appears to determine the coupling regime of the on-resonance molecular layer. Figure 5.5a shows that the plasmon resonance is beginning to split when the molecular layer is perpendicular to the surface, but it is only blue-shifted with a lower peak extinction for tangential dipoles. The change in behavior suggests the plasmonic-molecular coupling moves from the exciton induced transparency regime to the strong-coupling regime as the induced dipoles align to the surface normal. Figure 5.5b further demonstrates the change in interaction as the peak extinction has a local minimum at  $45^\circ$ . The results indicate the need to include molecular orientation when modeling plexcitonic systems, as an isotropic description would fail to reproduce these results.

Figure 5.6a shows the extinction spectra of dimers coated with normally (i) and tangentially (ii) oriented molecules. The extinction spectra have a single peak at approximately 582 nm corresponding to the red-shifted LSPR of the dimers. The normally oriented monolayer induces a maximum red-shift of 1.04 nm and a change in peak extinction of  $15.39 \text{ nm}^2$ , both larger than the monomer calculations because of the intense field enhancement seen inside the gap region of the dimer. The tangential dipoles also have a larger screening effect on the plasmonic interaction, as the peak extinction is further decreased for this orientation. Dimerization does not affect the qualitative trend between the LSPR and the orientation of the dipole moments, with the same monotonic decrease present. Finally, the molecular density acts mostly as a scaler to changes to the LSPR, demonstrating the weak coupling between the plasmonic and molecular modes.

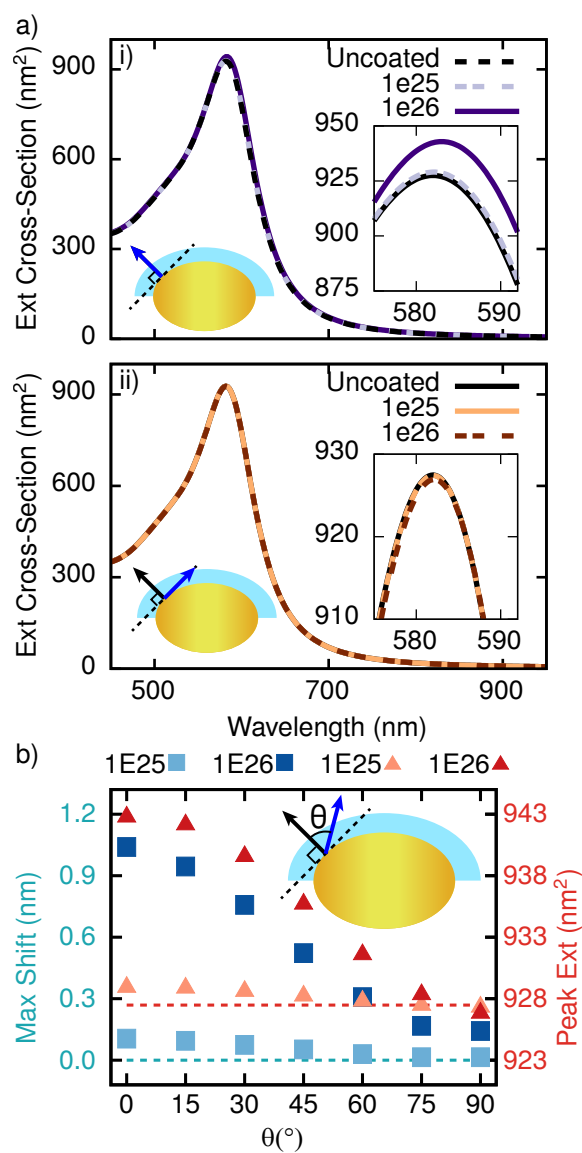


Figure 5.6. a) The extinction cross-section of gold nanoellipsoid dimers ( $x$ -axis is the inter-particle axis) coated with a molecular monolayer with an excitation at 300 nm and a transition dipole moment of 2.5 D oriented i) normally and ii) tangentially with molecular densities  $10^{25}$  and  $10^{26} \frac{\text{molecules}}{\text{m}^3}$ . b) Peak shifts (blue squares) and maximum extinction cross-sections (red triangles) of the coated nanoellipsoid dimers with varying degrees of alignment to the surface normal. Inset schematics demonstrate the dipole orientation (blue arrow) relative to the surface.

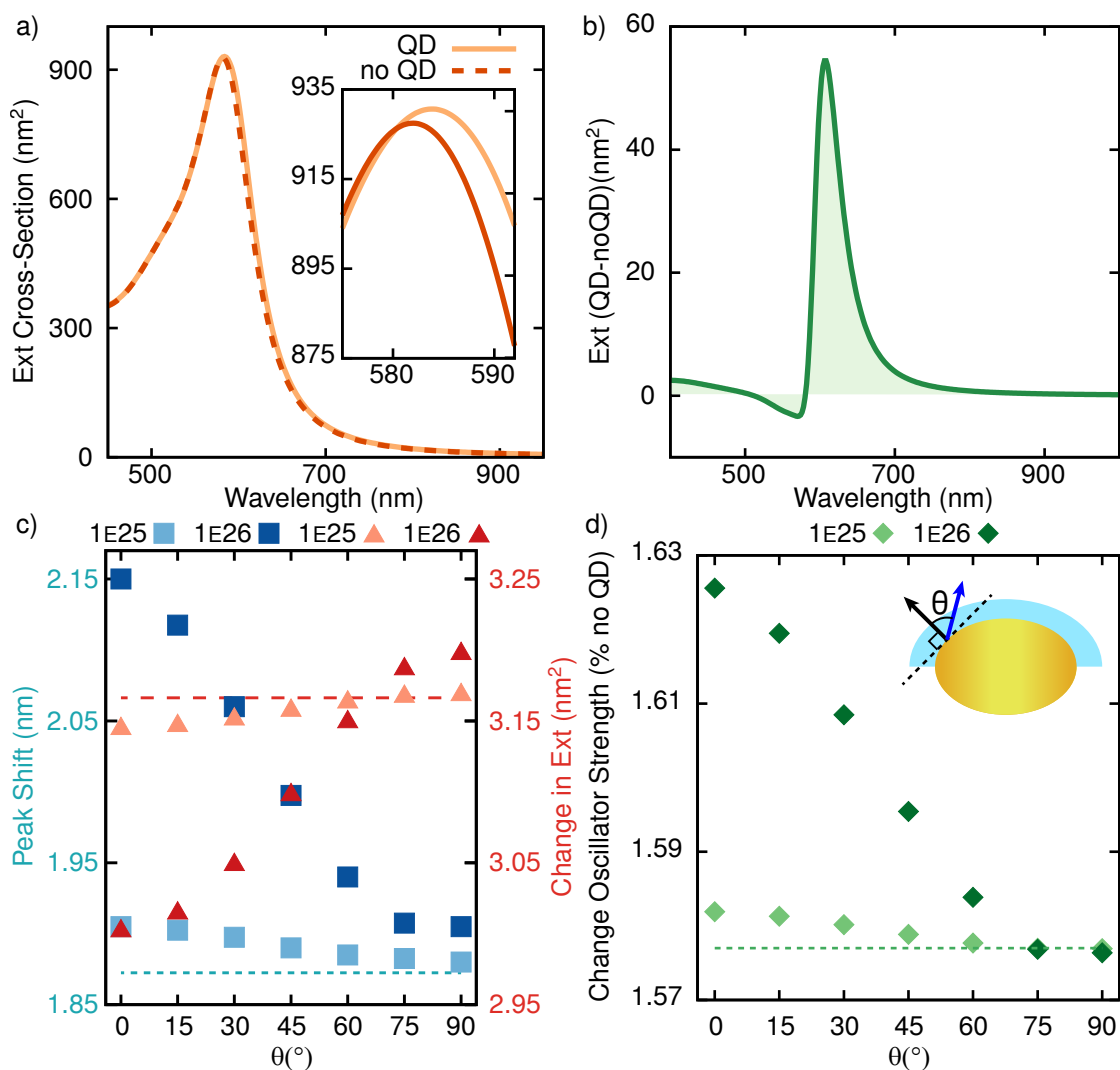


Figure 5.7. a) Extinction cross-section of the bare nanoellipsoid dimers with and without a quantum dot in the hot-spot. b) The difference between the extinction cross-section of the dimers coupled and uncoupled to the quantum dot. c) The peak shift (blue squares) and change in extinction cross-section (red triangles) for dimers coated with a molecular monolayer for different molecular densities reported in  $\frac{\text{molecules}}{\text{m}^3}$ . The dashed lines correspond to the bare gold nanoellipsoid dimers' peak shift (short dashes and blue) and change in peak extinction (long dashes and red) d) The change of oscillator strength for dimers coated with a molecular monolayer for different molecular densities normalized to the integral without coupling to a quantum dot. The dashed line is the change of the integral for the bare gold nanodimer. The inset schematic demonstrates the dipole orientation (blue arrow) relative to the surface.

The molecular coating also significantly affects the coupling between the gold nanoislands and a quantum dot monolayer. The monolayer is approximated by a single CdSe 610 nm quantum dot located inside the dimers hot-spot, which was previously shown to qualitatively represent a full film. The parameters for the quantum dots dielectric function are taken from our previous work.<sup>149</sup> Adding a CdSe 610 nm quantum dot to the bare gold nanoellipsoid dimer red-shifts and increases the intensity of the plasmon resonance by 1.88 nm and 3.16 nm<sup>2</sup> respectively as seen in Figure 5.7a. Both the red-shift and the increase in extinction maximum would increase to experimental values if a full film is included. All molecular orientations lead to small increases in the LSPR red-shift, with a maximum increase of under 0.3 nm for normally oriented dipoles. Interestingly, the change in peak extinction decreases as the molecular dipoles orient along the surface normal, by 0.02 and 0.16 nm<sup>2</sup> for respective molecular densities of 10<sup>25</sup> and 10<sup>26</sup>  $\frac{\text{molecules}}{\text{m}^3}$ . Figure 5.7d shows that the decrease is likely a result of changes in the width of the modes as integrating over the difference in total extinction with and without coupling to the quantum dot is maximized by the normally oriented molecules. The integral measures the effect of the quantum dots over a larger wavelength range, acting as a pseudo-oscillator strength encompassing all the modes in the region. We expect the change in oscillator strength to more accurately approximate the changes seen for the complete nanoisland films, as they have a broad range of LSPR wavelengths.

Tuning the molecular excitation to the dimers LSPR qualitatively modifies their coupling to both the dimer and the quantum dot. Figures 5.8a i, 5.8a ii, and 5.8b provide the same information as Figures 5.6b, 5.7c, and 5.7d respectively, but for a molecular layer with an excitation centered at 588 nm instead of 300 nm. Similar to the monomer case, the on-resonance

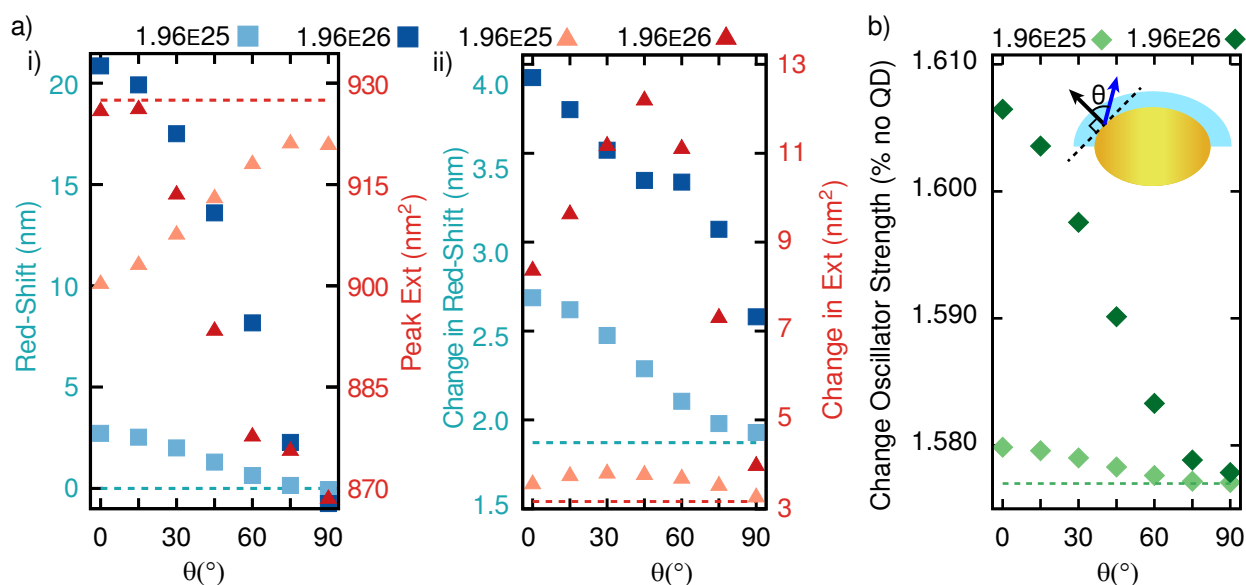


Figure 5.8. Effects of coating gold nanoellipsoids with a molecular layer that has an excitation wavelength of 588 nm and a transition dipole moment of 2.5 D oriented at different angles,  $\theta$ , from the surface normal. a) i) Peak shift (blue squares) and maximum extinction cross-section (red triangles) of the coated nanoellipsoid dimers. ii) The peak shift (blue squares) and change in extinction cross-section (red triangles) caused by coupling to a CdSe 610 nm quantum dot. The dashed lines correspond to the bare gold nanoellipsoid dimer's peak shift (short dashes and blue) and change in peak extinction (long dashes and red) b) The change of oscillator strength upon the addition of the quantum dot for dimers. The values are normalized to the integral without coupling to a quantum dot. The dashed line is the change of the integral for the bare gold nanodimer. Inset schematic demonstrates the dipole orientation (blue arrow) relative to the surface.

molecules have a larger effect on the plasmon resonance of the dimers. Changing the molecular density further supports the claim that the induced dipole orientation dictates the coupling regime between the nanoparticles and molecular films. The red-shift for both film densities increases as the dipoles align with the surface normal, indicating a stronger interaction. For the low density film, strengthening the interaction between the film and the nanoparticles decreases the peak extinction, representing a stronger exciton induced transparency response. At a higher

molecular density, the opposite trend is seen where increasing the interaction strength increases the peak extinction. The increase suggests the system is entering the strong coupling regime.

The on-resonance molecules also have a larger impact on the coupling of the dimers with the quantum dot. Qualitatively, the molecules increase the red-shift caused by the quantum dots in a similar manner as the off-resonant molecules, but with dramatically higher values. However, the change in peak extinction is different, as all coatings increase the change in peak extinction induced by the quantum dot. It appears that the orientation that leads to a maximal change in peak extinction is a function of the molecular density, but more tests are needed to confirm this relationship. The changes in the pseudo-oscillator strength do not reflect those of the peak values, as it largely mimics the off-resonance case but with smaller changes. This suggests that the molecular layer affects the coupling between the quantum dot and the film in a similar manner throughout different coupling regimes. Characterizing an on-resonance response with a full nanoisland film experimentally would be challenging as a large variety of LSPRs are present.

## 5.4 Conclusions

The methodology developed in the previous sections provides a new way of incorporating the orientation of induced dipole moments for study of the coupling between molecular coatings and plasmonic systems. The methodology is limited to treating the layer continuously, and hence effects of single molecular dipoles cannot be included. Currently the model is applicable only to magnetically inactive and achiral molecules, but magnetic transition dipole moments can be treated in a similar manner, allowing for an expansion of the methodology to both types of materials.<sup>54</sup> The model can also be extended to include any analytically Fourier transformable dielectric function, potentially increasing the accuracy of the molecular and metallic

optical responses. Quantum mechanical effects from the molecular layers can also be included if the dipolar orientation scheme is incorporated within a ML framework,<sup>58,61</sup> but quantum field effects are inaccessible. Overall, the method provides a means of including the molecular orientation for general nanoplasmonic systems.

To summarize, we presented a methodology to classically study the effects of ordered molecular monolayers using plasmonic nanostructures. The orientation of the molecular monolayer can dictate the magnitude of the LSPR red-shift induced by on-resonant molecules, hence the significance of this result. The chapter describes how the molecular orientation impacts the coupling between a molecular monolayer and plasmonic nanoparticles for the case of ellipsoidal nanoparticles. Finally, we studied how the molecular layers affect the coupling between colloidal quantum dots and ellipsoidal nanoparticles. Utilizing this methodology will allow for better modeling of molecular plasmonic systems for a variety of applications.

## CHAPTER 6

**A Study of Chiral Imprinting**

Chiral plasmonics is a growing field because of its potential to produce high performance biomolecule sensors and negative refractive index materials. Understanding and controlling molecular properties and their effect on the chiroptical coupling between chiral molecular films and metal nanostructures is thus vital for the future design of devices. Here we develop and apply a theoretical method to study that coupling. We first extend the three-dimensional finite-difference time-domain method to include chiral molecular layers with arbitrarily oriented induced dipole moments relative to the nanostructures surface. We then use the methodology to investigate the chiral imprinting response from nanospheres and a nanocross array as a test of the method. Finally, we explore the effect of chiral molecules on the coupling between ellipsoidal nanoparticles and a colloidal quantum dot.

Manuscript submitted to ACS Photonics

## 6.1 Introduction

The focus on chiral plasmonic materials has intensified because of their potential as high performance biomolecule sensors,<sup>152–155</sup> negative refractive index materials,<sup>156–159</sup> circular polarizers,<sup>160–162</sup> chiroptical switches,<sup>163,164</sup> and optical force generators.<sup>165–167</sup> Traditionally chiral plasmonics has focused on fabricating new chiral nanostructures,<sup>168–172</sup> but it has recently been shown that coupling chiral molecules to achiral nanostructures can lead to a transfer of the molecule’s chirality onto the nanostructures.<sup>54,56,140,151,173,174</sup> Various mechanisms have been proposed ranging from structural effects,<sup>56,175,176</sup> to electrodynamic coupling between the molecular dipoles and the nanoparticles.<sup>140,152,177,178</sup> Recent experimental evidence also demonstrated the importance of the dipole orientation on the plasmonic circular dichroism (CD) spectra of silver nanocubes.<sup>57</sup> The ability to computationally model all of these interactions is necessary in order to design new chiral plasmonic systems.

In this work we extend the finite-difference time-domain method (FDTD) to include anisotropic chiral materials. Previously developed methods, such as Bi-Isotropic-FDTD, include isotropic chiral media within FDTD using a wave field decomposition,<sup>179,180</sup> Mobius transformation,<sup>181</sup> or other techniques,<sup>182</sup> and provide useful insights, but these approaches have not been adapted for anisotropic materials. Other analytical techniques can include oriented molecular dipoles, but only apply to a specific class of nanoparticles and only examine single chiral dipole moments.<sup>54,140,177,178</sup> Work with both of these techniques demonstrate the need to accurately model both the system’s geometry and the orientation of the chiral layer.

Here we fully develop the new FDTD based method for including anisotropic chiral molecular layers as a continuous material. We next calculate the optical activity of gold nanospheres coated with a chiral medium with different induced dipole orientations relative to the surface,

and compare the results with previously published analytical results. A gold nanocross array is then investigated and we demonstrate the need to treat molecular layers as both an isotropic and an anisotropic material when considering high surface density films. Finally, we study how the chiral molecules impact the coupling between a gold nanoisland dimer and a quantum dot.

## 6.2 Methodology

In this section we extend a previously developed method for modeling oriented dipole moments to include chiral materials within FDTD.<sup>183</sup> For chiral materials the constitutive relations are altered using a modified Condon model to include chiral media,

$$(6.1a) \quad \mathbf{B} = \overline{\overline{\boldsymbol{\mu}}}\mathbf{H} + \left( \overline{\overline{\boldsymbol{\chi}}} + i\overline{\overline{\boldsymbol{\kappa}}}^T \right) \sqrt{\mu_0 \epsilon_0} \mathbf{E}$$

$$(6.1b) \quad \mathbf{D} = \overline{\overline{\boldsymbol{\epsilon}}}\mathbf{E} + \left( \overline{\overline{\boldsymbol{\chi}}} - i\overline{\overline{\boldsymbol{\kappa}}} \right) \sqrt{\mu_0 \epsilon_0} \mathbf{H}$$

where  $\overline{\overline{\boldsymbol{\epsilon}}}$  is the permittivity tensor,  $\overline{\overline{\boldsymbol{\mu}}}$  is the permeability tensor,  $\overline{\overline{\boldsymbol{\kappa}}}$  is the chirality parameter, and  $\overline{\overline{\boldsymbol{\chi}}}$  is the Tellegen parameter of the media.<sup>184</sup> Since all materials in this work are reciprocal,  $\overline{\overline{\boldsymbol{\chi}}}$  is set to zero.<sup>184</sup> The chirality parameter is approximated as

$$(6.2) \quad \overline{\overline{\boldsymbol{\kappa}}} = \frac{8\pi}{\hbar} n_m \sum_{c=1}^{n_{chi}} (\boldsymbol{\mu}_c \otimes \mathbf{m}_c) \frac{-i\omega}{\omega_c^2 + \Gamma_c^2 - \omega^2 + 2i\omega\Gamma_c},$$

where  $\hbar$  is the reduced Planck's constant;  $n_m$  is the molecular density;  $n_{chi}$  is the number of chiral modes;  $\omega$  is the angular frequency of light; and  $\omega_c$  is the resonant frequency,  $\boldsymbol{\mu}_c$  is the electric transition dipole moment,  $\mathbf{m}_c$  is the magnetic transition dipole moment, and  $\Gamma_c$  is a damping factor of the  $c^{th}$  chiral resonance.<sup>54</sup> The permittivity and permeability tensors of the

molecular layer are respectively defined as

$$(6.3a) \quad \bar{\bar{\epsilon}} = \bar{\bar{\epsilon}}_\infty + \frac{8\pi}{\hbar} n_m \sum_{l=1}^{n_{el}} (\boldsymbol{\mu}_l \otimes \boldsymbol{\mu}_l) \frac{\omega_l}{\omega_l^2 + \Gamma_l^2 - \omega^2 + 2i\omega\Gamma_l},$$

$$(6.3b) \quad \bar{\bar{\mu}} = \bar{\bar{\mu}}_\infty + \frac{8\pi}{\hbar} n_m \sum_{l=1}^{n_{mag}} (\mathbf{m}_l \otimes \mathbf{m}_l) \frac{\omega_l}{\omega_l^2 + \Gamma_l^2 - \omega^2 + 2i\omega\Gamma_l},$$

where  $\bar{\bar{\epsilon}}_\infty$  is the high frequency dielectric constant,  $\bar{\bar{\mu}}_\infty$  is the high frequency permeability,  $n_{el}$  is the number of polarizations, and  $n_{mag}$  is the number of magnetizations for the material.<sup>54</sup>

To make the material isotropic,  $\bar{\bar{\kappa}}$ ,  $\bar{\bar{\epsilon}}$ , and  $\bar{\bar{\mu}}$  are converted into scalars by replacing the outer product of the dipole moments with their respective dot products scaled by  $\frac{1}{3}$ .<sup>54</sup> For metallic materials  $\bar{\bar{\mu}}$  and  $\bar{\bar{\kappa}}$  are assumed to be the identity and zero matrices respectively and  $\bar{\bar{\epsilon}}$  is treated isotropically in the Lorentz-Drude model<sup>185</sup>

$$(6.4) \quad \epsilon = \epsilon_\infty - \frac{\sigma_D \omega_p^2}{\omega(\omega - i\Gamma_D)} + \sum_{l=1}^n \frac{\sigma_l \omega_p^2}{\omega_l^2 - \omega^2 + i\gamma_l \omega},$$

where  $\epsilon$  is the dielectric function of the metal;  $\epsilon_\infty$  is the high frequency dielectric constant of the material;  $\omega_p$  is the plasma frequency;  $\sigma_D$  and  $\Gamma_D$  are the oscillator strength and linewidth of the Drude pole, respectively;  $n$  is the number of Lorentz poles in the material; and  $\omega_l$  is the transition frequency,  $\sigma_l$  is the oscillator strength and  $\gamma_l$  is the linewidth of the  $l^{th}$  pole.<sup>185</sup>

The Auxiliary Differential Equation (ADE) method is used to include a dispersive material's response in FDTD. ADE recasts the constitutive relations as

$$(6.5a) \quad \mathbf{D} = \epsilon_0 \bar{\bar{\epsilon}}_\infty \mathbf{E} + \mathbf{P}_{\text{Metal}} + \mathbf{P}_{\text{Molecule}},$$

$$(6.5b) \quad \mathbf{B} = \mu_0 \bar{\bar{\mu}}_\infty \mathbf{H} + \mathbf{M}_{\text{Molecule}},$$

where in the frequency domain  $\mathbf{P}_{\text{Metal}}$ ,  $\mathbf{P}_{\text{Molecule}}$ , and  $\mathbf{M}_{\text{Molecule}}$  are defined as

$$(6.6a) \quad \check{\mathbf{P}}_{\text{Metal}} = \varepsilon \check{\mathbf{E}},$$

$$(6.6b) \quad \check{\mathbf{P}}_{\text{Molecule}} = \bar{\varepsilon} \check{\mathbf{E}} - i \bar{\kappa} \check{\mathbf{H}},$$

$$(6.6c) \quad \check{\mathbf{M}}_{\text{Molecule}} = \bar{\mu} \check{\mathbf{H}} + i \bar{\kappa}^T \check{\mathbf{E}}.$$

The polarization and magnetization fields are then inverse Fourier transformed and all of the resulting derivatives are expanded with a central-difference approximation to generate the update equations, defined for chiral polarizations and chiral and achiral magnetizations as

$$(6.7a) \quad \mathbf{P}_{\text{Chi}}^{n+1} = \frac{2 - (\omega_c^2 + \Gamma_c^2) \Delta_t^2}{\Gamma_c \Delta_t + 1} \mathbf{P}_{\text{Chi}}^n + \frac{\Gamma_c \Delta_t - 1}{\Gamma_c \Delta_t + 1} \mathbf{P}_{\text{Chi}}^{n-1} + \frac{8\pi n_m \Delta_t^2}{\hbar (\Gamma_c \Delta_t + 1)} \boldsymbol{\mu}_c \left[ \frac{\mathbf{m}_c}{\Delta_t} \cdot \left( \mathbf{H}_{i,j,k}^{n+\frac{1}{2}} - \mathbf{H}_{i,j,k}^{n-\frac{1}{2}} \right) \right]$$

$$(6.7b) \quad \mathbf{M}_{\text{Chi}}^{n+\frac{1}{2}} = \frac{2 - (\omega_c^2 + \Gamma_c^2) \Delta_t^2}{\Gamma_c \Delta_t + 1} \mathbf{M}_{\text{Chi}}^{n-\frac{1}{2}} + \frac{\Gamma_c \Delta_t - 1}{\Gamma_c \Delta_t + 1} \mathbf{M}_{\text{Chi}}^{n-\frac{3}{2}} + \frac{8\pi n_m \Delta_t^2}{\hbar (\Gamma_c \Delta_t + 1)} \mathbf{m}_c \left[ \frac{\boldsymbol{\mu}_c}{\Delta_t} \cdot \left( \mathbf{E}_{i+\frac{1}{2},j+\frac{1}{2},k+\frac{1}{2}}^n - \mathbf{E}_{i+\frac{1}{2},j+\frac{1}{2},k+\frac{1}{2}}^{n-1} \right) \right],$$

$$(6.7c) \quad \mathbf{M}_{\text{Achi}}^{n+\frac{1}{2}} = \frac{2 - (\omega_l^2 + \Gamma_l^2) \Delta_t^2}{\Gamma_l \Delta_t + 1} \mathbf{M}_{\text{Achi}}^{n-\frac{1}{2}} + \frac{\Gamma_l \Delta_t - 1}{\Gamma_l \Delta_t + 1} \mathbf{M}_{\text{Achi}}^{n-\frac{3}{2}} + \frac{8\pi n_c \omega_l \Delta_t^2}{\hbar (\Gamma_l \Delta_t + 1)} \mathbf{m}_l (\mathbf{m}_l \cdot \mathbf{H}_{i+\frac{1}{2},j+\frac{1}{2},k+\frac{1}{2}}^{n+\frac{1}{2}})$$

where  $\Delta_t$  is the time step size;  $n$  is the current time step;  $i$ ,  $j$ , and  $k$  are grid point coordinates in the  $x$ ,  $y$ , and  $z$  directions; and  $\mathbf{E}_{i+\frac{1}{2},j+\frac{1}{2},k+\frac{1}{2}}^n$ ,  $\mathbf{H}_{i,j,k}^{n-\frac{1}{2}}$ , and  $\mathbf{H}_{i+\frac{1}{2},j+\frac{1}{2},k+\frac{1}{2}}^{n-\frac{1}{2}}$  are found through spatially averaging the field components. The update equations for the non-chiral components of  $\check{\mathbf{P}}_{\text{Metal}}$  and  $\check{\mathbf{P}}_{\text{Molecule}}$  were previously defined in References 38 and 39, respectively. <sup>183, 185</sup>

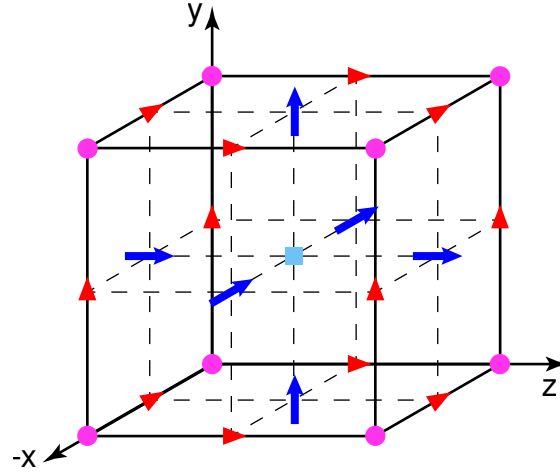


Figure 6.1. Schematic illustration of the FDTD unit cell for chiral materials. The blue arrows represent the magnetic field components, the red triangles represent the electric field components, the pink circles are the location of the dipole moments needed to calculate  $\mathbf{P}_{\text{Molecule}}$ , and the light blue square represent the locations of the dipole moments needed to calculate  $\mathbf{M}_{\text{Molecule}}$ .

Figure 6.1 displays the modified Yee Cell for anisotropic chiral material. For isotropic materials the chiral polarization and magnetization terms are calculated at their respective electric and magnetic field component locations represented by the red triangles and blue arrows, respectively. For anisotropic materials  $\mathbf{P}_{\text{Molecule}}$ ,  $\mathbf{M}_{\text{Molecule}}$ , and the dipole moments needed to calculate them are stored at points illustrated by the pink circles and light blue squares, respectively. The molecular layer is treated as a set of transition magnetic and electric dipole moments oriented at a polar angle,  $\theta$ , and azimuthal angle,  $\phi$ , relative to the surface normal,  $\mathbf{n}$ , of a nanoparticle. Because the typical value of  $|\mathbf{m}|$  is considerably smaller than  $|\boldsymbol{\mu}|$ , we assume that the magnetic and electric dipole moments are parallel to each other and that  $|\mathbf{m}| = |\mathbf{m}_{\text{exp}}| \cos \psi$ , where  $\mathbf{m}_{\text{exp}}$  is the experimental transition magnetic dipole moment and  $\psi$  is the angle between

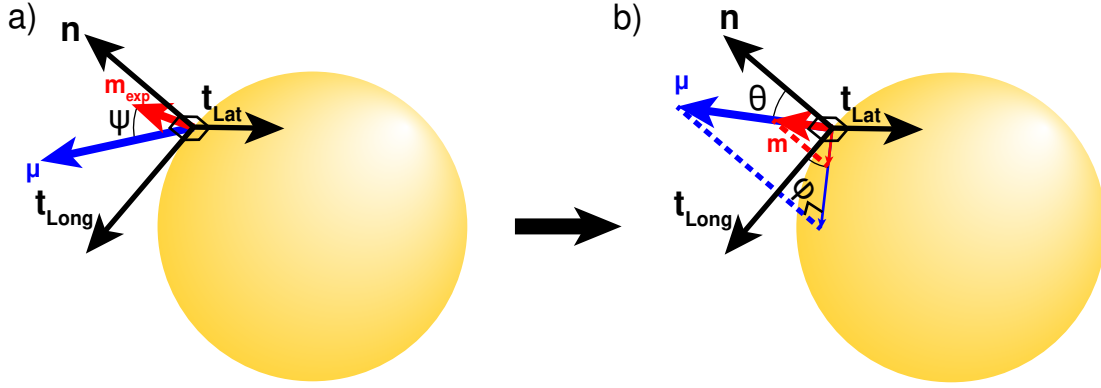


Figure 6.2. Schematic showing how  $\mu_c$  (blue) and  $m_c$  (red) are calculated from the surface normal of the nanoparticle. a) The real system and b) the approximated molecular resonance

$\mu$  and  $m_{\text{exp}}$ . At all grid points within the molecular layer the surface normal of the nanostructures is calculated by

$$(6.8) \quad \mathbf{n} = \frac{\nabla \mathcal{F}(x, y, z)}{|\nabla \mathcal{F}(x, y, z)|},$$

where  $\mathcal{F}(x, y, z)$  describes the surface of the nanoparticles. The longitudinal and latitudinal tangent vectors,  $\mathbf{t}_{\text{Long}}$  and  $\mathbf{t}_{\text{Lat}}$ , are calculated from the normal vector by rotating the polar angle of  $\mathbf{n}$  by  $90^\circ$  and taking the cross product between  $\mathbf{n}$  and  $\mathbf{T}_{\text{Long}}$ . Once the rotated coordinate frame is established, the molecular dipole moments are calculated by

$$(6.9) \quad \boldsymbol{\mu}_m = |\boldsymbol{\mu}_m| (\cos \theta \mathbf{n} + \sin \theta \cos \phi \mathbf{t}_{\text{Long}} + \sin \theta \sin \phi \mathbf{t}_{\text{Lat}}),$$

where  $\theta$  and  $\phi$  are the polar and azimuthal angles defined in Figure 6.2b.

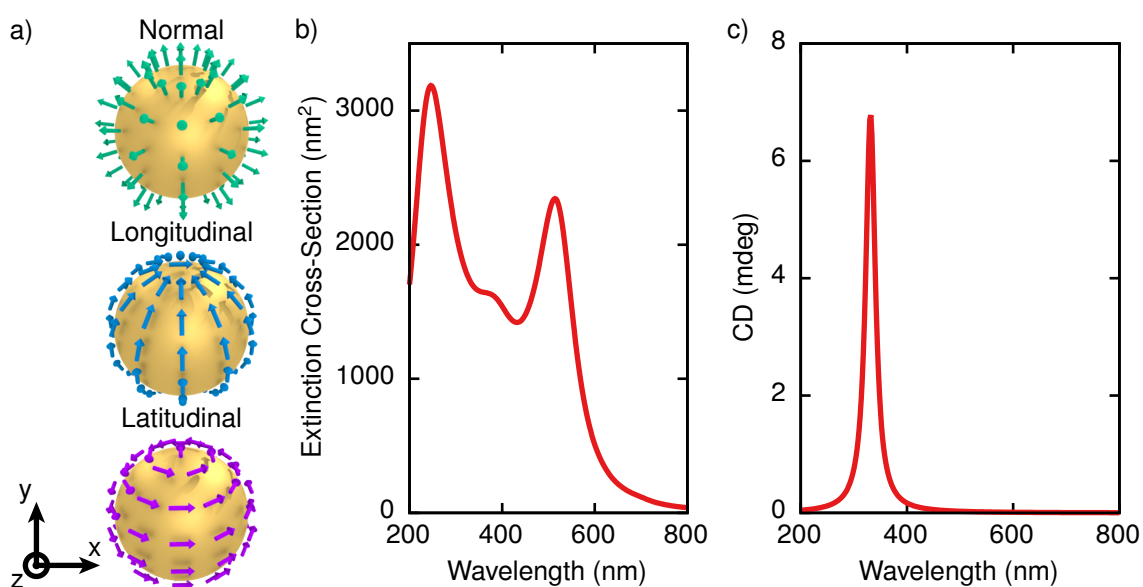


Figure 6.3. a) Illustration of normally, longitudinally, and latitudinally oriented dipoles on a gold sphere. b) The extinction cross-section of a 40 nm gold sphere. c) The CD spectrum for the 5 nm chiral shell coating the spheres.

## 6.3 Results

### 6.3.1 Chiral Imprinting For Gold Nanospheres

To gain a more detailed perspective on how the induced dipole orientation affects the chiral imprinting on metal nanoparticles, a previously studied gold nanosphere system is investigated. While the previous studies explored the coupling between a single chiral dipole and a nanoparticle, a complete film including intermolecular interactions has not been investigated.<sup>54,140</sup> The system comprises of a 40 nm gold nanosphere coated with a 5 nm chiral molecular layer. The chiral molecules have a single mode centered at 333 nm, a width of  $2,000\text{ cm}^{-1}$ , an electric transition dipole moment of 2.5 D, and a magnetic transition dipole moment of  $2.5 \times 10^{-6}$  Bohr magnetons ( $\mu_B$ ). The molecular layer is treated isotropically or as a set of induced dipole moments oriented normally, latitudinally, and longitudinally to the spherical surface, as illustrated in Figure 6.3a. The extinction cross-section of the gold spheres and the CD spectrum of the

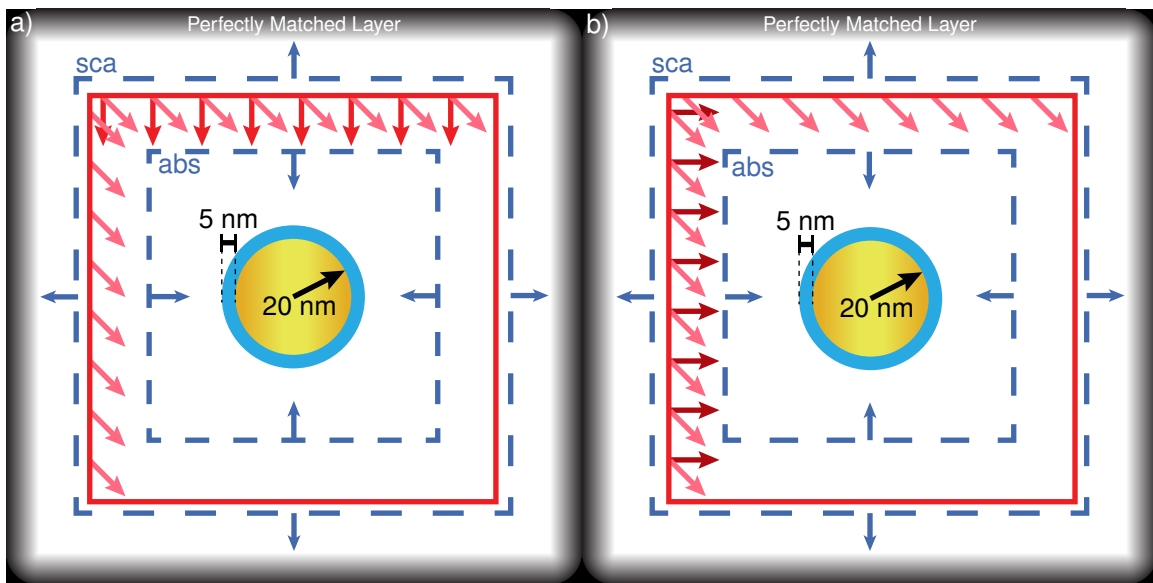


Figure 6.4. Cell map for the sphere in the a)  $yz$ - and b)  $xy$ - planes. The gold circle represents the gold nanospheres. The blue shell is the 5 nm chiral shell. The blue boxes represent the absorption and scattering flux regions. The system is excited from a TF/SF surface (red box) along either the longitudinal axis (dark red arrows), latitudinal axis (red arrows), or the diagonal (pink arrows) with a pulse centered at 333 nm, and a width of 1.67 fs. The cell has 20 unit cell thick CPML regions at the boundary.

5 nm isotropic molecular layer are shown in Figure 6.3b and 6.3c, respectively. The isotropic tangential orientation splits the single molecular dipole moment into separate latitudinal and longitudinal dipoles scaled by a factor of  $\frac{1}{\sqrt{2}}$ .

A map of the FDTD cell for the system is illustrated in Figure 6.4. The molecularly coated spheres are placed in the center of the FDTD cell with an absorption and scattering flux region surrounding the nanoparticles. The dielectric parameters for gold are taken from the work of Rakic, et al.<sup>4</sup> A total field/scattered field (TF/SF) surface is placed in between the two flux surfaces and used to generate a plane wave of wavelength,  $\lambda$ , with a wavevector,  $\mathbf{k}$ , of  $[\frac{2\pi}{\lambda}, 0, 0]$  (dark red arrows),  $[0, 0, \frac{2\pi}{\lambda}]$  (red arrows) and  $[\frac{2\pi}{\lambda\sqrt{3}}, \frac{2\pi}{\lambda\sqrt{3}}, \frac{2\pi}{\lambda\sqrt{3}}]$  (pink arrows), respectively representing the latitudinal, longitudinal, and diagonal axes. The system is excited by a Gaussian

pulse centered at 333 nm with a width of 1.67 fs to span the relevant frequency range. The cell is surrounded by a 20 unit cell convolution perfectly matched layer (CPML) to absorb all the outgoing waves.

Figures 6.5a, 6.5b, and 6.5c show the CD spectra of the coated gold spheres excited by a plane wave with different wavevectors. The results agree with those of Govorov and Fan's analytical quantum mechanical model of single molecular dipoles coupled to plasmonic spheres,<sup>140</sup> confirming that the implementation and the classical approximations are valid for these systems. Treating the molecules isotropically results in the weakest chiral plasmonic response because it closely resembles a random orientation, which does not exhibit chiral imprinting behavior. For the rest of the configurations the strength of the plasmonic CD response is proportional to the overlap between the plasmonic fields and the induced molecular dipoles. The direction of  $\mathbf{k}$  affects only the tangential orientations because they do not have spherical symmetry. If spherical symmetry is preserved by treating the induced dipoles isotropically in the tangential plane, then the angle of incidence of light has no effect. The response can be equilibrated by equally exciting all modes along the diagonal axis.

Orienting the induced dipoles along a non-axial tangential vector significantly increases the magnitude of the CD spectra because of the chiral arrangement of the dipole moments. Figure 6.6a illustrates the two enantiomers made by setting  $\phi$  to  $45^\circ$  and  $135^\circ$ . Figure 6.6b shows that the CD response for these systems is dominated by the chiral configuration of the induced dipoles, with the molecular chirality only mildly perturbing the response. The handedness of the system depends on whether the system is being excited predominantly along the latitudinal or longitudinal axis, with a canceling out point at  $\pm 45^\circ$  from either axis. The difference in CD magnitude of the system excited along a longitudinal and latitudinal axes is a result of

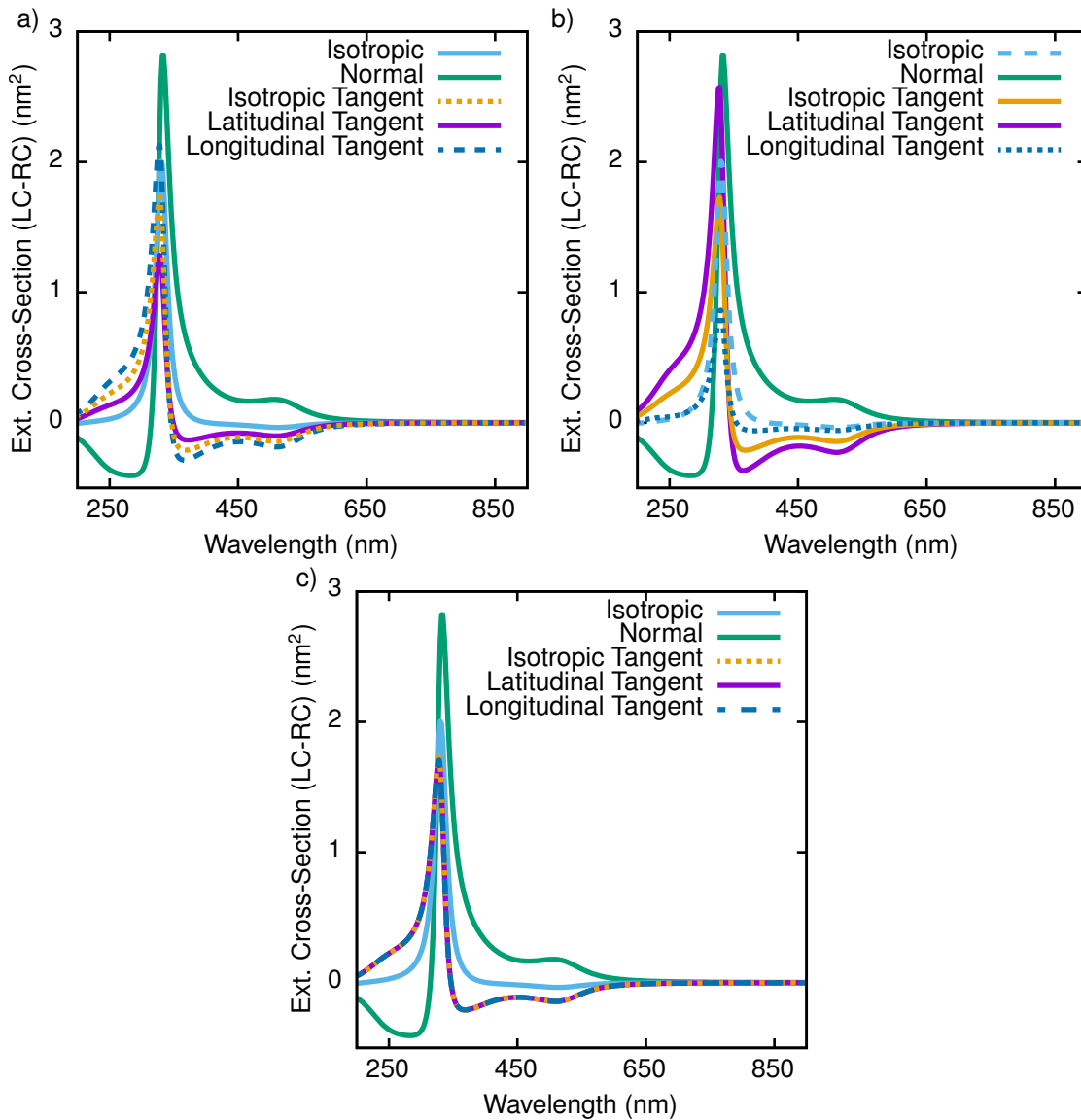


Figure 6.5. CD spectra of gold spheres coated with a 5 nm layer of chiral molecules treated isotropically, oriented along the surface normal, and oriented along the tangential vectors excited by a plane wave with a  $\mathbf{k}$  of a)  $\mathbf{k} = [\frac{2\pi}{\lambda}, 0, 0]$ , b)  $\mathbf{k} = [0, 0, \frac{2\pi}{\lambda}]$ , c)  $\mathbf{k} = [\frac{2\pi}{\lambda\sqrt{3}}, \frac{2\pi}{\lambda\sqrt{3}}, \frac{2\pi}{\lambda\sqrt{3}}]$ .

the overlap between the induced dipoles and the incident light. Removing the chirality of the molecules by setting  $|\mathbf{m}|$  to zero better illustrates the effects of the arrangement. Figure 6.6c

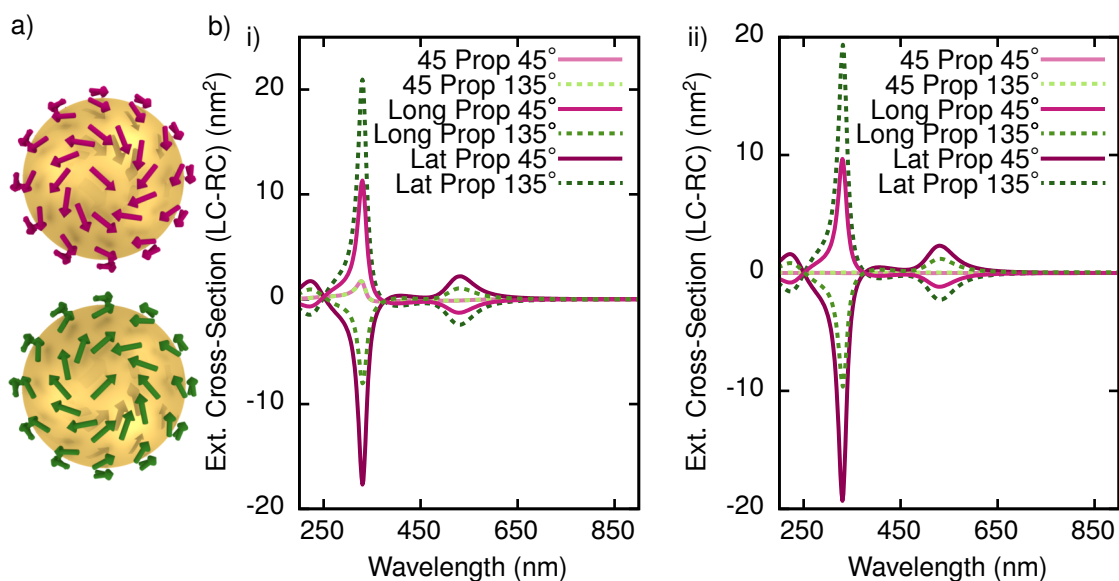


Figure 6.6. a) Illustration of the tangential dipole moments oriented at an azimuthal angle of 45° (red) and 135° (green) relative to the surface normal (perspective down the latitudinal axis). b) CD spectra of the gold sphere coated with a i) chiral and an ii) achiral molecular monolayer with a tangential orientation and an azimuthal angle of 45° (red, solid) and 135° (green, dashed) propagated along the latitudinal, longitudinal, and diagonal axes

shows that the enantiomers have the same CD spectra, but with the opposite sign, and an achiral response for the system excited along the diagonal.

### 6.3.2 Mixed Orientational and Isotropic Coupling Between Chiral Molecules and a Gold Nanocross Array

The second system used to test the generality of the methodology is the gold nanocross array first investigated by Abdulrahman, et al.<sup>151</sup> The array consists of gold nanocrosses with a length of 400 nm, a width of 80 nm, a thickness of 50 nm, and a periodicity of 800 nm, as illustrated in Figure 6.7a and 6.7b. It is coated with a thin film of Flavin mononucleotide (FMN), a biomolecule with strong chiroptical resonance in the near UV.<sup>151</sup> Figures 6.7c and 6.7d show the computational absorbance and CD spectra for a 875 nm thick layer of FMN molecules

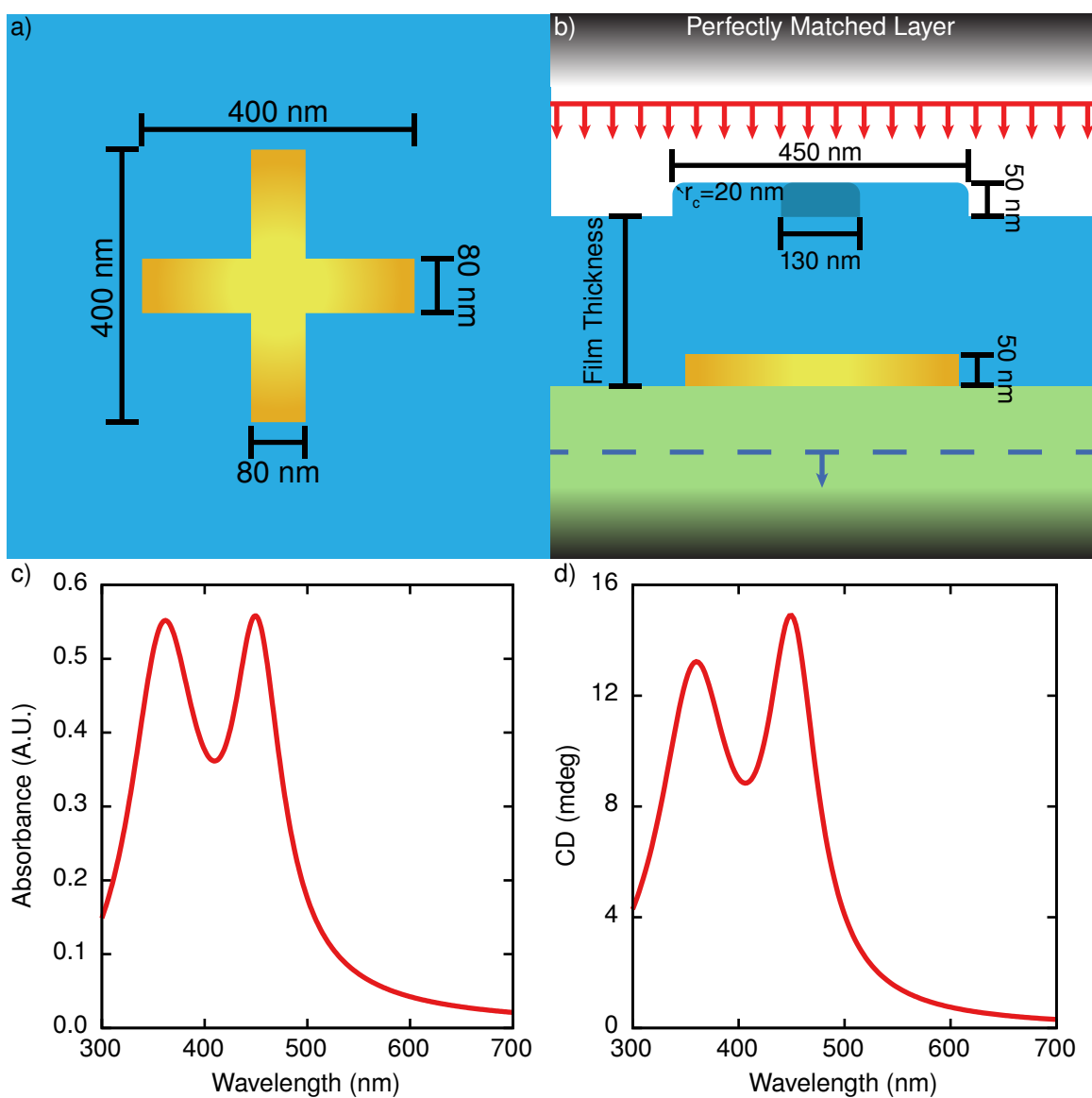


Figure 6.7. Cell map of the FDTD cell used to model the nanocross array in the a)  $xz$ - and b)  $xy$ - planes. The c) absorbance and d) CD spectra of an 875 nm thick film of FMN molecules.

corresponding to an estimated surface density of  $70 \frac{\mu\text{g}}{\text{cm}^2}$ .<sup>151</sup> The molecular density of the FMN films is  $n_m = 1.05 \times 10^{27} \frac{\text{molecules}}{\text{m}^3}$  and the molecules have two resonances with the parameters:  $\omega_1 = 385.5 \text{ nm}$ ,  $\gamma_1 = 620 \text{ cm}^{-1}$ ,  $|\mu_1| = 0.635 \text{ D}$ ,  $|\mathbf{m}_1| = 3.28 \times 10^{-8} \mu_B$ ,  $\omega_2 = 460.4 \text{ nm}$ ,  $\gamma_2 =$

$280 \text{ cm}^{-1}$ ,  $|\boldsymbol{\mu}_2| = 0.44 \text{ D}$ , and  $|\mathbf{m}_2| = 2.87 \times 10^{-8} \mu_B$ . Both spectra are in good agreement with their experimental counterparts published by Abdulrahman et al, but with longer low frequency tails.

The experimental system is replicated in the FDTD cell shown in Figures 6.7a and 6.7b. The cell is periodic in the  $x$ - and  $z$ -directions and bounded by a 48 unit cell thick CPML in the  $y$ -direction. In order to accommodate the oblique scattered fields from the nanoarray, stabilized CPML parameters of  $\sigma_{max} = 1.5\sigma_{opt}$ ,  $\alpha_{max} = 0.9$ , and  $\kappa_{max} = 3.0$  are used. The gold nanocrosses have dielectric parameters taken from McMahon et al.,<sup>5</sup> and are placed on a semi-infinite borosilicate glass substrate with an index of refraction of 1.603. The conversion factor between the thickness of the molecular layer and its estimated surface density is  $80 \frac{\text{ng}}{\text{cm}^2 \text{nm}_{\text{thickness}}}$ .<sup>151</sup> The array is excited from above by left and right handed circularly polarized, Gaussian pulses from a TF/SF surface, with a center wavelength of 588 nm and a width of 1.67 fs. The simulations are performed on a grid with a spacing and time step of 5 nm and 8.34 as, respectively, and run for a total of 5.00 ps. While the fields are not fully converged at 5.00 ps, they are sufficiently decayed to be a good approximation to the total optical response. The transmission flux is calculated inside the borosilicate substrate at the blue dashed line in Figure 6.7b and converted to absorbance with,

$$(6.10) \quad A = \log \frac{\mathbf{S}_0}{\mathbf{S}_{\text{Transmitted}}},$$

where  $\mathbf{S}_0$  and  $\mathbf{S}_{\text{Transmitted}}$  are the poynting vector of the incident and transmitted fields across the entire surface, respectively. From here the CD response is calculated and normalized using

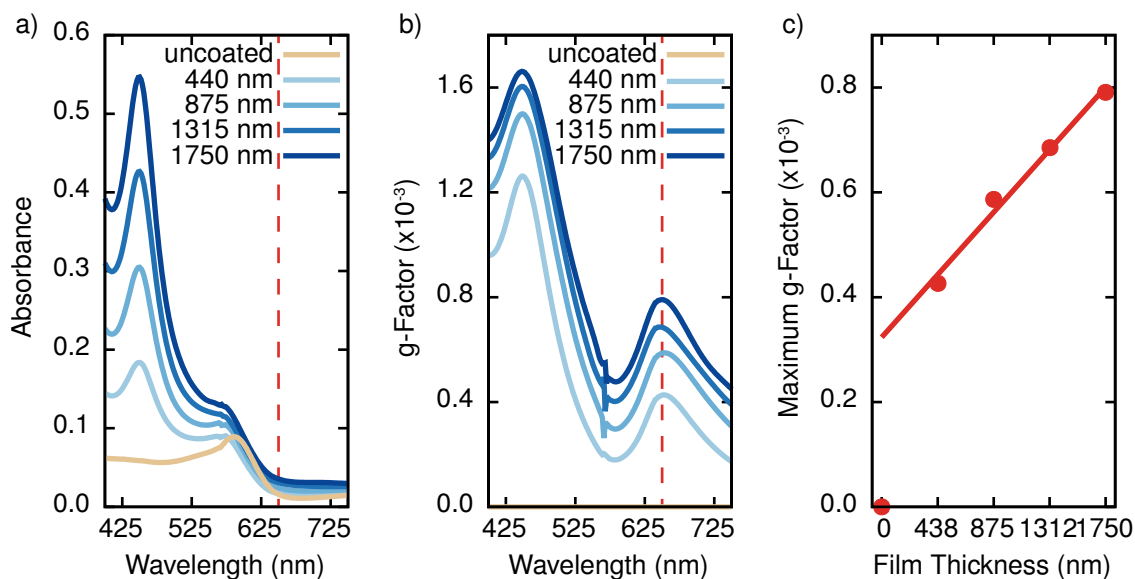


Figure 6.8. a) Absorbance spectra for the gold nanocross array coated with a layer of FMN molecules of different thicknesses b) Anisotropy factor spectra for the gold nanocross array coated with a layer of FMN molecules of different thicknesses c) Anisotropy factor at 650 nm against the thickness of the FMN films.

the anisotropy factor,  $g$ ,

$$(6.11) \quad g = \frac{A_+ - A_-}{\bar{A}},$$

where  $A_+$  and  $A_-$  are the absorbance of left and right handed circularly polarized light and  $\bar{A}$  is the average absorbance.

Figure 6.8 shows the chiroptical response of the gold nanoarrays. The absorbance spectra for the uncoated nanocrosses has a plasmon resonance at 586 nm, which is blue-shifted to 575 nm once coated. The apparent blue-shift is the result of the overlap between the FMN resonance and the plasmon resonance, but the plasmon resonance is likely red-shifted from its uncoated position. The relatively small numerical artifacts at 575 nm are due to the incomplete convergence of the fields from inter-cross scattering. Significantly increasing the run time would

remove the artifacts, but not affect the overall absorbance. While the calculated absorbance of the uncoated 50 nm gold films is significantly larger than what was reported by Abdulrahman et al., it is within the expected range for gold nanostructures of this size.<sup>151</sup>

The trend in the peak intensity of the plasmonic modes in the CD spectra qualitatively matches the experiments. Figure 6.8b shows the anisotropy factor spectra for the calculated films, which have two peaks associated with a molecular and a plasmon resonance at 450 nm and 652 nm, respectively. The plasmon resonance is red-shifted from its locations in the absorbance spectra because of the way  $g$  is calculated and the location of the actual resonant frequency. The magnitude of  $g$  is smaller than its experimental value because of the larger calculated absorbance of the nanocrosses, but grows almost linearly with film thickness at the plasmon resonance. The agreement between the experimental and calculated results shows that we are correctly modeling the changes in the system as the film density increases; however, the model is incomplete because treating the films isotropically does not reproduce the negative features seen experimentally for the  $35 \frac{\mu\text{g}}{\text{cm}^2}$  films.<sup>151</sup>

A potential cause for the negative CD response at the plasmon resonance is the orientation of the induced dipoles near the nanoparticle's surface. As shown previously, a tangential molecular layer induces a chiral plasmonic response with the opposite handedness to that of the molecules. To understand the effects of the molecular orientation on the nanoarray's optical activity, the arrays are coated with a 220 nm thick partially oriented FMN film. The crosses are initially coated with a 50 nm oriented layer, with the rest of the 220 nm film treated isotropically as illustrated in Figures 6.9a and 6.9b. Figure 6.9c shows the anisotropy factor for the nanocrosses coated with only the oriented 50 nm layer included. The oriented layers further red-shift the plasmon CD response to approximately 672 nm for all dipole orientations. The

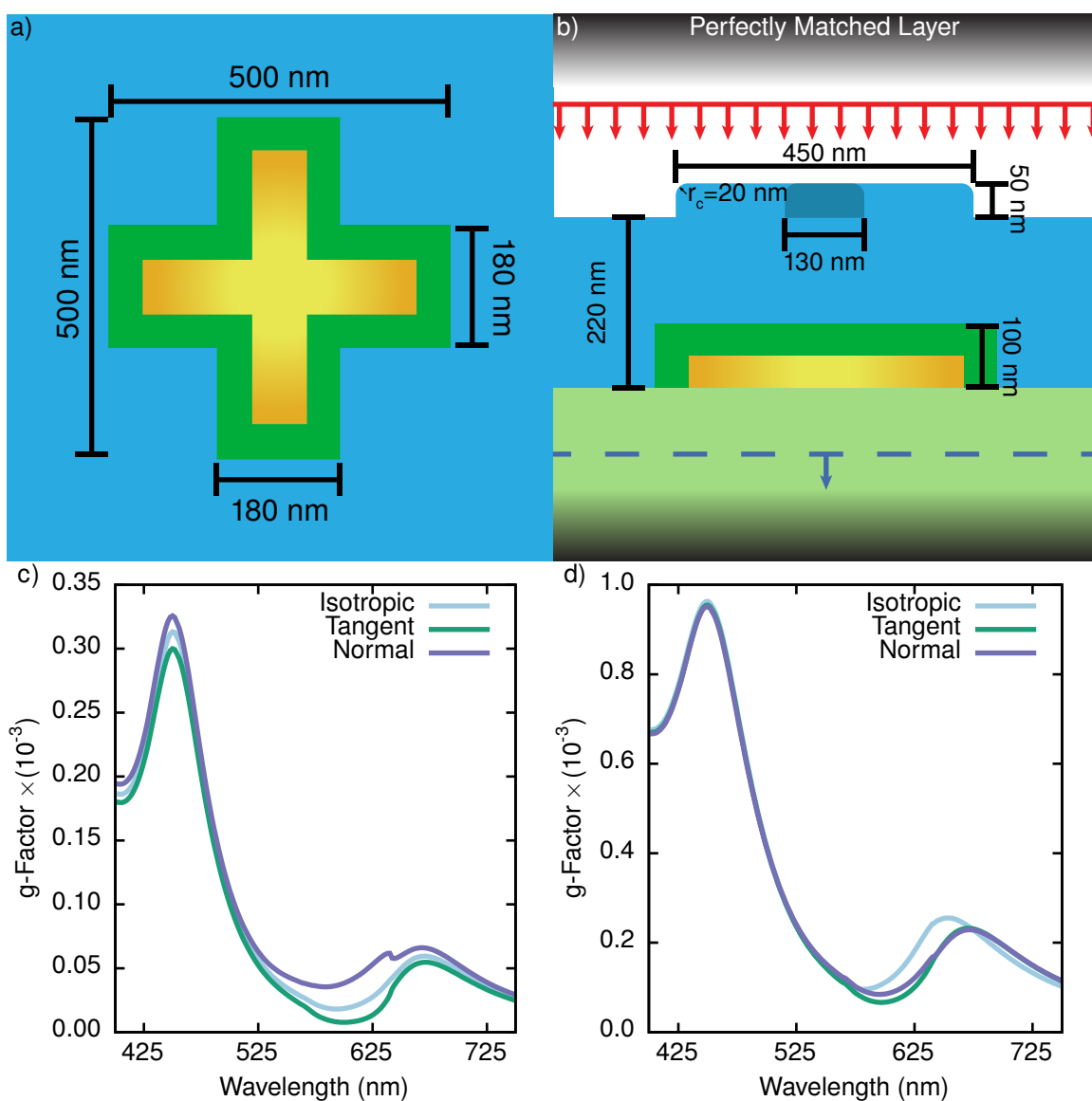


Figure 6.9. a-b) Cell map of the partially oriented molecular films in the a)  $xz$ - and b)  $xy$ - planes. The dark green crosses represent the oriented dipole regions. c-d) Anisotropy factor spectra for the gold nanocross array coated with a 50 nm oriented dipole FMN film: c) without and d) with a 220 nm isotropic layer above it.

largest difference between the spectra occur at 600 nm, where the tangential dipoles induce a slight dip. The decrease does not cause a change in handedness of the resonance because of

the FMN mode's tail. We expect that given a better FMN model and a better description of the molecular orientation near the gold nanoisland surfaces,<sup>58,61,186</sup> the method would reproduce the experimental results quantitatively.

Adding an isotropic layer to the system reduces the effect of the oriented induced dipoles. Figure 6.9d shows that incorporating the rest of the film as an isotropic layer qualitatively replicates the experimental spectra. Both the normal and the tangential dipole moments preserve the increased red-shift of the plasmon resonance, while the isotropic treatment is more in line with the previous examples. Preserving the peak location suggests that the local order surrounding the crosses primarily dictates the interactions between the film and the nanoparticles. However, the increased molecular density does increase the lowest point in  $g$ , which explains why only the  $35 \frac{\text{molecules}}{\text{m}^3}$  film has a negative feature in the experiments. These results indicate that the coupling between gold nanocross arrays and the FMN layers can not be explained solely by long range electrodynamic interactions, but they must be considered in combination with short-range dipole-dipole interactions.

### 6.3.3 How Chiral Molecules Affect the Coupling Between Nanoparticles and Quantum Dots

A recent study investigated the effects of a chiral molecular layer on the coupling between a gold metal nanoisland film and a colloidal quantum dot monolayer.<sup>150</sup> The authors found a consistent doubling of the total quantum dot absorption enhancement when a chiral ( $\alpha$ -helix L-polyalanine) organic linker layer was used instead of an achiral ((3-mercaptopropyl)trimethoxysilane) linker.<sup>150</sup> Bezen et al. attributed the increased extinction to a symmetry breaking within the quantum dots arising from interactions with the chiral molecules, which was supported by the decreases in peak extinction once a second layer of molecules is adsorbed onto the quantum

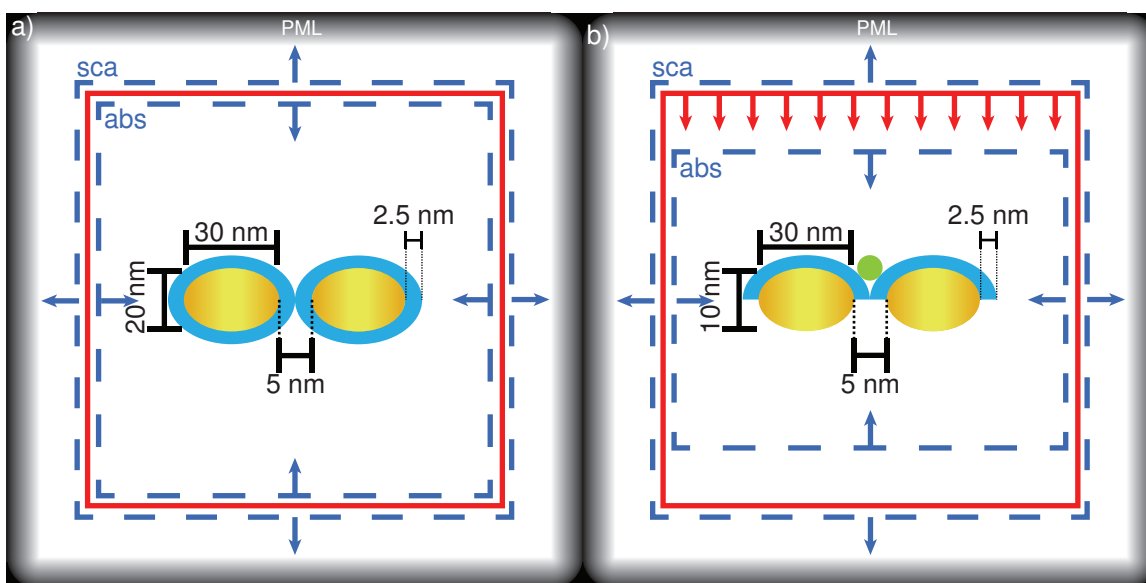


Figure 6.10. Cell diagram for the calculation in the a)  $xy$ - and b)  $xz$ - planes. The green ball represents the quantum dot, the blue arc is the molecular layer, and the gold ellipses are the nanoparticles. The system is excited from above by a TF/SF surface (red), and the absorption and scattering fluxes are calculated over a box 6 nm inside and outside the TF/SF surface, respectively. The cell has 20 unit cells thick PML regions at the boundary.

dots.<sup>150</sup> Nonetheless, a more in depth study of the mechanism is needed to confirm the proposed cause.

The full nanoisland films are approximated as a single gold nanoellipsoid dimer with  $x$ -,  $y$ -, and  $z$ -, axis lengths of 30 nm, 20 nm, and 10 nm respectively that are separated by a 5 nm gap. The dielectric parameters for gold are taken from the work of Rakic, et al.<sup>4</sup> The dimers are then coated with a 2.5 nm molecular monolayer, where the molecules have a single resonance centered around 300 nm with a width of  $2,000 \text{ cm}^{-1}$ , a transition electric dipole moment of 2.5 D, and a magnetic transition dipole moment magnitude of  $2.5 \times 10^{-5} \mu_B$ . This model has been previously shown to qualitatively describe the full metal nanoisland dimers.<sup>103,149,183</sup> The handedness of the molecules is controlled by the sign of  $\mathbf{m}$ , where a positive sign corresponds

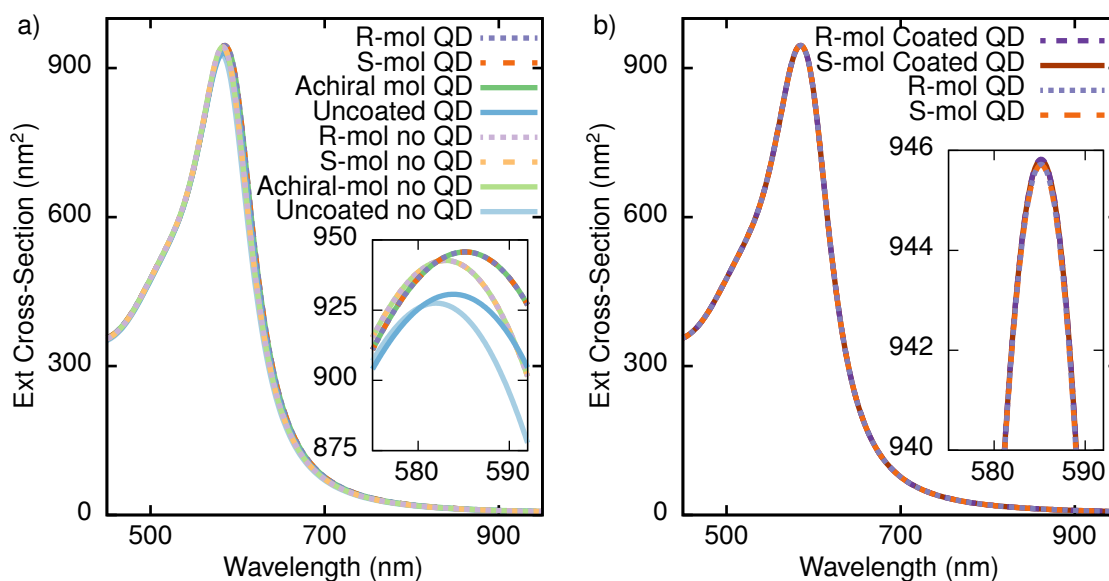


Figure 6.11. a) Extinction cross-section of the molecularly coated nanoellipsoid dimers coupled and uncoupled to a quantum dot in the center of the gap b) The extinction cross-section of the dimers coated with chiral molecules coupled to a quantum dot with and without the quantum dot also coated with the molecular layer.

to left-handed molecules and negative sign corresponds to a right handed enantiomer. Based on the results of our previous calculations, the molecular layer will always be oriented along the surface normal of the nanoparticles to maximize the response.<sup>183</sup> Figure 6.10 illustrates the cell map for the ellipsoid dimers. A single quantum dot is placed in the center of the gap resting on top of the molecular dipole layer. The FDTD cell is bounded by a 20 unit cell CPML layer in all directions and is excited with a linearly polarized pulse from a TF/SF surface with a center wavelength of 588 nm and a width of 1.667 fs. The absorption and scattering flux are calculated on a surface 6 nm inside and outside the TF/SF surface, respectively. The calculations use a grid spacing of 5 Å and a time step of 1.67 as, and run for 166.78 fs.

Figure 6.11 shows the effects of the chiral molecules on the optical response of the bare gold nanoislands with and without coupling to the quantum dot. To isolate the effects of chirality on the dimers an achiral version of the molecular layer is also calculated, by setting  $\mathbf{m}$  to zero. For all calculations the chiral and achiral molecules have nearly identical responses with minor differences resulting from the weak magnetic and chiral polarizations. These results suggest that the primary cause for the increased absorption from the chiral films seen in the experiments are due to either a more normally oriented dipole moment or a stronger transition dipole moment. The enantiomers also show the same optical response when coupled to the quantum dots, supporting the hypothesis that differences in the quantum dot's optical response between the two linker enantiomers is from changes in the quantum dot binding.<sup>150</sup> Figure 6.11b shows that this model predicts a further enhancement from adsorbing a second molecular layer over the quantum dot, which is qualitatively different from the experimental spectra. The dipole moments for the top molecular layer are flipped to match the change in linking geometry, but those changes should not affect the final coupling as the sign changes for the dipole moments cancel out. The discrepancy suggests that either a classical description does not fully encapsulate the coupling between the chiral molecules and the quantum dots or their coupling changes the molecular or quantum dot dielectric properties. Further investigation is needed to account for all experimental observations.

## 6.4 Conclusions

In the previous sections we presented a methodology to classically model the chiroptical coupling between molecular films and plasmonic nanostructures. The methodology can describe, within the classical framework, any chiral or achiral molecular layer with electrically or magnetically active modes oriented in any direction relative to a metal nanosurface. Our

approach assumes that the material can be treated continuously, hence single molecular dipoles can not be included. Incorporating the dipole moment schemes within a ML algorithm would extend the model to the semiclassical regime,<sup>58,61</sup> where the molecular modes would be treated quantum mechanically, but a fully quantum mechanical treatment of the system is outside the scope of the method.

Within this approach we showed how the orientation of the induced dipole moments dictates the handedness of the chiral plasmon. We illustrated that incorporating both dipole-dipole and long range electrodynamic coupling is necessary in order to replicate the CD spectra of a FMN coated nanocross array. Finally, we described how the molecular chirality affects the coupling between colloidal quantum dots and ellipsoidal nanoparticles, and noted a potential limitation of the classical approximation. Utilizing this methodology will allow for better modeling of chiral plasmonic systems for a variety of applications.

## CHAPTER 7

**Optimizing Nanoparticles for Dye-Sensitized Solar Cells**

Solar energy can provide clean and sustainable energy for the world. Dye-sensitized solar cells are a promising technology for low cost solar energy production, but they require higher efficiencies to compete with commercial solar cells. The current research uses a genetic algorithm to optimize the composition and structure of metal nanoparticles, for maximal light absorption in a dye-sensitized solar cell's photoanode. The genetic algorithm finds the global optimum for a reduced parameter space problem, without including the dye molecule's effect on the electromagnetic field. Simple tests including dye molecules demonstrate that small metal nanoparticles are best for dye-sensitized solar cells.

## 7.1 Introduction

To limit the damaging impacts of global climate change and to meet the accelerating demand for energy resources, new forms of clean energy are needed. Because of the abundance and reliability of energy provided by the sun, solar energy conversion is an attractive alternative to fossil fuels. Research related to the design and development of photovoltaic technologies is a topic of active interest. An efficient, cost-effective means to achieve solar energy conversion would help stem the impact of climate change, and increase the overall proportion of our domestic renewable energy production.

Commercially viable solar cells require higher efficiencies and lower unit costs. Despite recent reports of solar cells reaching a total efficiency above 25%,<sup>187</sup> their current total cost makes them unattractive for large scale application. According to the US Energy Information Administration, photovoltaics are going to be more expensive than other forms of power generation per megawatt hour for at least the next five years.<sup>188</sup> The greatest contributor to the cost of silicon solar cells is the pristine silicon wafer needed to absorb light, representing 40% of total costs.<sup>189</sup> For solar energy to become market competitive, both the fabrication and materials cost must be lowered.

Dye-sensitized solar cells (DSSCs) are a promising technology for low cost solar energy production. DSSCs function by using dye molecules adsorbed to a mesoporous semiconducting film to absorb light, and transfer the excited state electrons to the semiconductor. Because dye molecules are the light harvesting element in DSSCs, lower cost materials can be used for device fabrication.<sup>190</sup>

One of the largest obstacles facing DSSCs is their relatively low power conversion efficiencies (PCE). Kakiage et al. hold the current record for DSSC efficiency with a PCE of over

14%,<sup>191</sup> compared with a record PCE of over 26% for silicon solar cells.<sup>192</sup> Extending the light harvesting region of the dye molecules into the near infrared is one way to increase the efficiency of DSSCs.<sup>193</sup> While porphyrin dye molecules extend the light harvesting region to approximately 700 nm,<sup>18,194,195</sup> they are still short of the 940 nm absorption onset needed for optimal DSSC performance.<sup>196</sup>

Zhao and co-workers were the first to demonstrate that metal nanoparticles (MNPs) improve the efficiency of DSSCs in 1997,<sup>197</sup> but they became more popular once Standridge et al. showed metal oxide layers protected them from the corrosive electrolyte.<sup>130,198</sup> MNPs primarily improve the efficiency of DSSCs by supporting LSPRs, which increase the amount of light seen by the dye.<sup>19,198</sup> Many different structures increase the PCE of DSSCs including trimer geometries,<sup>199</sup> hollow TiO<sub>2</sub> nanoparticles,<sup>200</sup> multiple core-shell oxide@metal@oxide nanoparticles,<sup>20</sup> and silver-encapsulated gold nanorods.<sup>201</sup>

Because of the large variety of possible MNP configurations and the high cost for testing them, an exhaustive experimental search is impossible. Computationally optimizing the system can limit the number of experiments that need to be performed, by guiding experimentalists to the most promising candidates. While traditional optimization techniques are efficient, they easily get trapped in local optima on rugged fitness landscapes. Trajectory-based optimization algorithms are too inefficient because evaluating the objective function is the most time consuming step. Population-based methods such as genetic algorithms (GAs) are well suited for such a global optimization problem.

## 7.2 Methodology

Optimization with GAs is done in a manner similar to evolution by natural selection.<sup>202</sup> A random initial population of solutions is generated, and each individual's fitness is calculated.

The best solutions are then selected and mated to populate the next generation. The mating procedure is varied across different implementations, but involves genetic operations like crossover, an exchange of parameters between two individuals, and mutation, a modification of an individual's parameters.<sup>203</sup> The cycle is repeated until the optimal structure within the parameter space is found.

The genetic algorithm's fitness function is an approximation to the incident photon to current efficiency (IPCE)<sup>204</sup>

$$(7.1) \quad IPCE(\lambda) = \frac{J_{sc}(\lambda)}{e\Phi(\lambda)} = 1240 \frac{J_{sc}(\lambda)}{\lambda P_{in}(\lambda)},$$

where  $J_{sc}$  is the short circuit or the photocurrent,  $e$  is the charge of the electron,  $\Phi$  is the incident flux,  $\lambda$  is the incident wavelength, and  $P_{in}$  is the incident power. Because  $J_{sc}$  cannot be directly calculated from optical properties, it is assumed to be proportional to the absorption of the photoanode. The absorption spectrum is then normalized to the solar spectrum and integrated to get

$$(7.2) \quad fitness = \frac{\int A_{anode}(\lambda) I_{AM1.5}(\lambda) \lambda d\lambda}{\int \lambda I_{AM1.5}(\lambda) d\lambda},$$

where  $A_{anode}$  is the calculated absorption spectrum of the photoanode and  $I_{AM1.5}$  is the solar spectrum.<sup>205</sup>

The photoanode absorption can be calculated using various electrodynamic and electronic structure methods. Classical methods such as FDTD<sup>62</sup> can be used to optimize nanoplasmonic systems,<sup>206,207</sup> but can only model the dye molecules classically.<sup>120</sup> While density functional methods can be used to describe the absorption spectrum of dye molecules, MNPs cannot be modeled by them.<sup>122,208,209</sup> FDTD is used to calculate the optical response of the system.

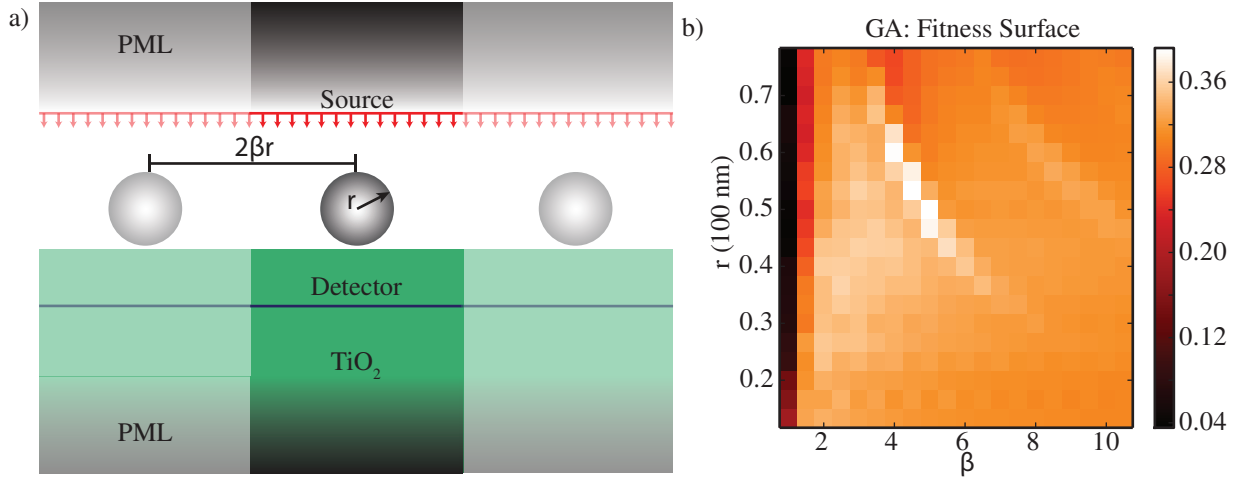


Figure 7.1. (a) Schematic of the computational cell, (b) Fitness surface as generated by a grid search

For the FDTD calculations, it is further assumed that the absorption of the photoanode is well approximated by weighting the transmission spectrum inside the TiO<sub>2</sub> substrate to the normalized absorption of the dye molecule (N719)

$$(7.3) \quad fitness = \frac{\int T_{FDTD}(\lambda) \alpha_{molecule}(\lambda) I_{AM1.5}(\lambda) \lambda d\lambda}{\int \lambda I_{AM1.5}(\lambda) d\lambda},$$

where  $T_{FDTD}$  is the transmission spectra from the FDTD calculation and  $\alpha$  is the normalized absorption spectra of the molecule.<sup>210</sup>

## 7.3 Results

### 7.3.1 Initial Optimization

To test the genetic algorithm against a known fitness surface, a grid search is performed on a reduced parameter space corresponding to the radius of the particle,  $r$ , and a periodicity factor,  $\beta$ , which sets the cell width to  $2\beta r$ . The periodicity is chosen as a measure of the particle density. The test cell and fitness surface are shown in Figure 7.1a and 7.1b respectively. The

MNP is placed 5 nm above a semi-infinite TiO<sub>2</sub> substrate with periodic boundary conditions in the transverse direction, to model inter-particle interactions. Three main optimal regions are seen in the fitness surface with a band in the upper right hand corner, a band in the center, and a region in the lower left with many local optimum; confirming the parameter space is too rugged for traditional optimization.

The initial GA parameters are a population size of 100, a crossover rate of 60% and a mutation rate of 30%. The selection method is a three individual tournament operator. Tournament operators populate the next generation by randomly selecting  $n$  individuals, where  $n$  is the number of individuals in the tournament, from the previous generation and adding the fittest individual to the breeding population. Genetic operators act directly on the breeding population to generate the next generation of solutions. The crossover method is single point crossover, which takes two solutions and swaps their genomes at a random point. The mutation operator changes a single gene of an individual to a random value on a uniform distribution to allow the population to explore new areas.

To better determine the GA's performance, the initial grid search fitness surface is linearly interpolated in both directions and used to determine the fitness of individuals in the genetic algorithm. A large deviation between the best and average solutions is seen in Figure 7.2a, which is a result of the mutation rate being too high. When the solutions are mapped onto the fitness surface tight clustering is seen around both global and local optima, suggesting premature convergence is occurring. The deviations between the best and average solutions are decreased upon lowering the mutation rate to 5% as can be seen in Figure 7.2c. To avoid premature convergence the mutation operator is changed to use a normal distribution instead of a uniform

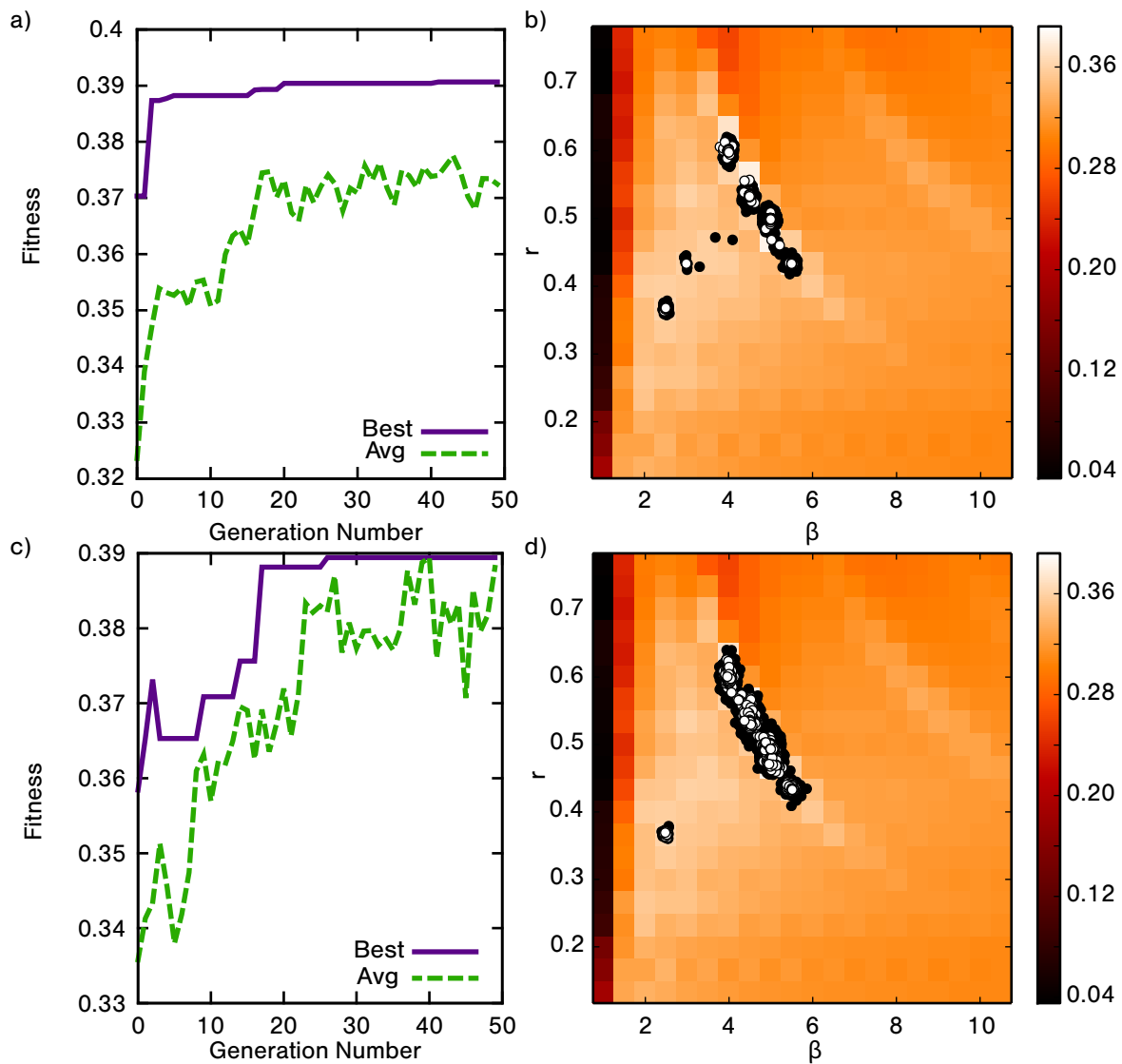


Figure 7.2. The results of applying the GA to an interpolated fitness surface for the a) the convergence of a representative run for the GA with the uniform distribution mutation operator, where best is the best individual in a generation and Avg is the average individual in the population b) The best (white circles) and average (black circles) solutions plotted on the fitness surface for GA with the uniform distribution mutation operator c) the convergence of a representative run of the GA with the normal distribution mutation operator, where best is the best individual in a generation and Avg is the average individual in the population d) The best (white circles) and average (black circles) solutions plotted on the fitness surface for GA with the normal distribution mutation operator

distribution to reset the genes. While the population in the local optima regions is lowered by the new mutation operator, the amount of solutions finding the global optimum is also decreased.

### 7.3.2 Developing a Better Objective Function

Optimizing silver nanoparticles for DSSCs require a reworking of the objective function to better match actual systems. The largest drawback with the previous model was the exclusion of the  $\text{TiO}_2$  nanoparticles coated with the dye molecules. The inter-particle spacing is removed as a parameter as the particles are typically at too low of a concentration in the photoanodes for it to be significant. To address these issues the FDTD cell is modified and shown in Figure 7.3a.

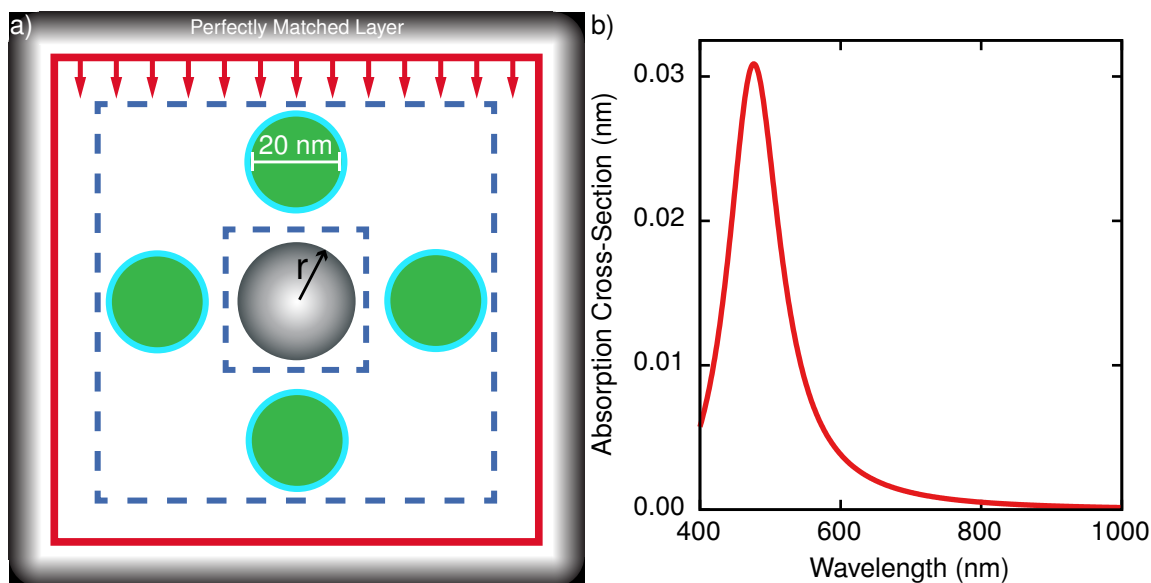


Figure 7.3. a) Diagram of the new FDTD cell for the objective function. The silver sphere in the center is the silver nanoparticle with a variable radius. The green circles with a blue border represent the coated  $\text{TiO}_2$  nanoparticles separated by 5 nm from the silver nanoparticle. The absorption of the photoanode is approximated by adding the two flux regions (blue dashed line) with positive flux pointing towards the coated nanoparticles. The cell is excited from a plane wave generated from the TF/SF surface and the cell uses CPMLs as the boundary conditions. b) Absorption cross-section for the molecularly coated  $\text{TiO}_2$  nanoparticle.

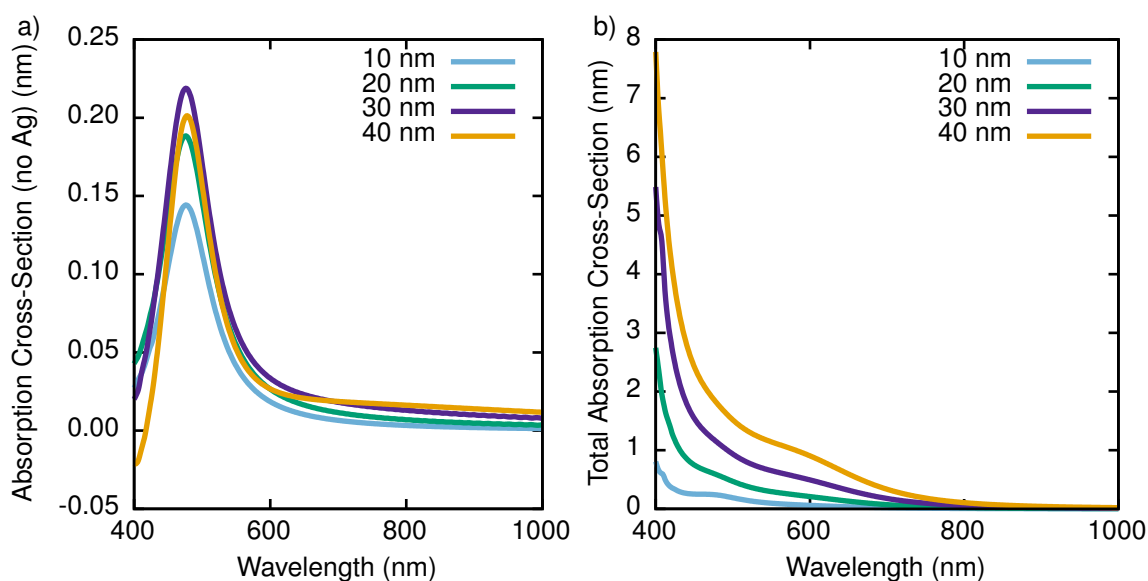


Figure 7.4. a) Absorption cross-section of the total system subtracted by the absorption cross-section of the silver nanoparticle. b) Absorption cross-section of the total system for silver nanoparticles with a radius of 10, 20, 30, and 40 nm.

In this geometry the plasmonic particles are surrounded by molecularly coated  $\text{TiO}_2$  particles and separated from the silver nanoparticle by 5 nm. The absorption cross-section for the total system and only the silver nanoparticle are calculated along the blue boxes to decouple the molecular and silver nanoparticles' absorption. Figure 7.3b shows the absorption cross-section of the molecularly coated  $\text{TiO}_2$  nanoparticles. For the initial test the dye molecules are treated as a 2.5 nm thick isotropic monolayer with a single resonance centered at 500 nm, a transition dipole moment of 2.5 D, molecular density of  $1.5 \times 10^{26} \frac{\text{molecules}}{\text{m}^3}$  and a spectral width of  $10,000 \text{ cm}^{-1}$ , but can be modified to match the absorption of any dye molecule.

Figure 7.4 displays the total absorption cross-section of only the molecularly coated  $\text{TiO}_2$  nanoparticles and the total system. The total system absorption increases with the nanoparticle radius as the nanoparticle dominates the total absorption. This trend does not continue for the

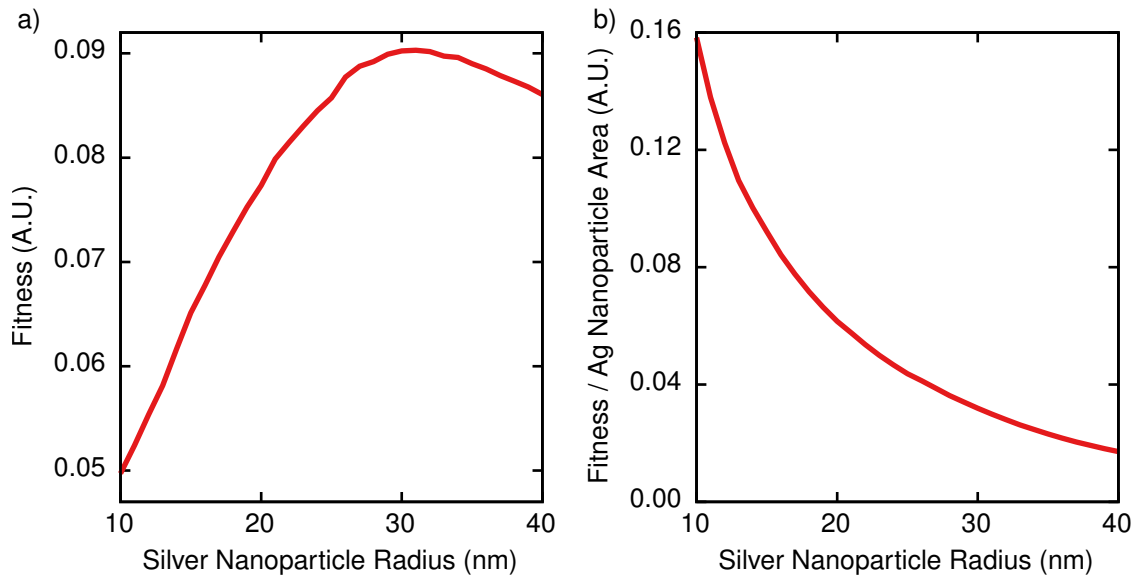


Figure 7.5. a) Fitness of the nanoparticles against the radius. b) The fitness of the nanoparticles divided by the area of the circles.

molecular absorption, which begins to decrease after the nanoparticle's radius get above 30 nm. Subtracting out the silver nanoparticle's absorption does not completely decouple the molecular and plasmonic modes as the molecular absorption becomes negative for some of the systems and there is a non-zero positive tail at longer wavelengths. Despite these issues the model does replicate the molecular response fairly well.

Utilizing this system requires the fitness function to be slightly modified to

$$(7.4) \quad fitness = \frac{\int A_{TiO_2}(\omega) I_{AM1.5}(\omega) d\omega}{\int I_{AM1.5}(\omega) d\omega},$$

where  $A_{TiO_2}$  is the absorption cross-section of the molecularly coated  $TiO_2$  nanoparticles. The fitness function is no longer unitless as  $A_{TiO_2}$  has units of distance. Figure 7.5 shows the relationship between the fitness function and the nanoparticle radius. The fitness of the nanoparticles

largely match the molecular absorption with a maximum occurring for nanoparticle with a radius of 31 nm. However once the nanoparticles volume is included (in two dimensions the area of the circular cross-section) the smaller nanoparticles significantly out perform the larger ones. Normalizing the fitness function to the nanoparticle volume should give a better approximation to the DSSC performance as the nanoparticles do not contribute to the photo-current.

#### **7.4 Conclusions**

A genetic algorithm could provide a useful way for optimizing the use of metal nanoparticles for dye-sensitized solar cells. Utilizing the initial fitness function and set of parameters the genetic algorithm is able to find the most promising region of the objective space. Utilizing the new fitness function should provide a way to optimize the particles for all restraints on the system, and be generalizable enough to match any system.

## References

- [1] Bohren, C. F.; Huffman, D. R. *Absorption and Scattering of Light by Small Particles*; Wiley-VCH Verlag GmbH: Weinheim, Germany, 1998.
- [2] Maier, S. *Plasmonics: Fundamentals and Applications*; Springer: New York, NY, 1st ed., 2007.
- [3] Jackson, J. D. *Classical Electrodynamics*; Wiley, 1975.
- [4] Rakic, A. D.; Djurisic, A. B.; Elazar, J. M.; Majewski, M. L. *Appl. Opt.* **1998**, 37(22), 5271–5283.
- [5] McMahon, J. M.; Schatz, G. C.; Gray, S. K. *Phys. Chem. Chem. Phys.* **2013**, 15, 5414.
- [6] Guler, U.; Suslov, S.; Kildishev, A. V.; Boltasseva, A.; Shalaev, V. M. *Nanophotonics* **2015**, 4(1), 269–276.
- [7] Guler, U.; Naik, G. V.; Boltasseva, A.; Shalaev, V. M.; Kildishev, A. V. *Appl. Phys. B Lasers Opt.* **2012**, 107(2), 285–291.
- [8] Kuwata, H.; Tamaru, H.; Esumi, K.; Miyano, K. *Appl. Phys. Lett.* **2003**, 83(22), 4625–4627.
- [9] Kelly, K. L.; Coronado, E.; Zhao, L. L.; Schatz, G. C. *J. Phys. Chem. B* **2003**, 107(3), 668–677.
- [10] Guo, X.; Ma, Y.; Wang, Y.; Tong, L. *Laser Photonics Rev.* **2013**, 7(6), 855–881.
- [11] Hu, H.; Ji, D.; Zeng, X.; Liu, K.; Gan, Q. *Sci. Rep.* **2013**, 3(1), 1249.
- [12] Krasavin, A. V.; Zayats, A. V. *Adv. Opt. Mater.* **2015**, 3(12), 1662–1690.
- [13] Yao, K.; Liu, Y. *Nanotechnol. Rev.* **2014**, 3(2), 177–210.
- [14] Pu, M.; Ma, X.; Li, X.; Guo, Y.; Luo, X. *J. Mater. Chem. C* **2017**, 5(18), 4361–4378.
- [15] Monticone, F.; Alù, A. *Chinese Phys. B* **2014**, 23(4), 047809.

- [16] Wang, Z.; Cheng, F.; Winsor, T.; Liu, Y. *Nanotechnology* **2016**, 27(41), 412001.
- [17] Lee, Y. K.; Lee, H.; Lee, C.; Hwang, E.; Park, J. Y. *J. Phys. Condens. Matter* **2016**, 28(25), 254006.
- [18] Mathew, S.; Yella, A.; Gao, P.; Humphry-Baker, R.; Curchod, B. F. E.; Ashari-Astani, N.; Tavernelli, I.; Rothlisberger, U.; Nazeeruddin, M. K.; Grätzel, M. *Nat. Chem.* **2014**, 6(3), 242–247.
- [19] Qi, J.; Dang, X.; Hammond, P. T.; Belcher, A. M. *ACS Nano*. **2011**, 5(9), 7108–7116.
- [20] Dang, X.; Qi, J.; Klug, M. T.; Chen, P. Y.; Yun, D. S.; Fang, N. X.; Hammond, P. T.; Belcher, A. M. *Nano Lett.* **2013**, 13, 637–642.
- [21] Kuo, Y.; Ting, S.-Y.; Liao, C.-H.; Huang, J.-J.; Chen, C.-Y. C.-Y.; Hsieh, C.; Lu, Y.-C.; Chen, C.-Y. C.-Y.; Shen, K.-C.; Lu, C.-F.; Yeh, D.-M.; Wang, J.-Y.; Chuang, W.-H.; Kiang, Y.-W.; Yang, C. C. *Opt. Express* **2011**, 19 Suppl 4(July), A914—29.
- [22] Kuo, Y.; Su, C.-Y.; Hsieh, C.; Chang, W.-Y.; Huang, C.-A.; Kiang, Y.-W.; Yang, C. C. *Opt. Lett.* **2015**, 40(18), 4229–4232.
- [23] Wang, J.; Yang, G.; Zhang, Q.; Gao, S.; Zhang, R.; Zheng, Y. *Plasmonics* **2017**, 12(3), 843–848.
- [24] Huang, L.; Tu, C.-C. C.; Lin, L. Y. *Appl. Phys. Lett.* **2011**, 98(11), 113110.
- [25] García De Arquer, F. P.; Beck, F. J.; Bernechea, M.; Konstantatos, G. *Appl. Phys. Lett.* **2012**, 100, 1–5.
- [26] Chang, C.-C.; Sharma, Y. D.; Kim, Y.-S.; Bur, J. A.; Sheno, R. V.; Krishna, S.; Huang, D.; Lin, S.-Y. *Nano Lett.* **2010**, 10(5), 1704–1709.
- [27] Mayer, K. M.; Hafner, J. H. *Chem. Rev.* **2011**, 111(6), 3828–3857.
- [28] Dabirian, A.; Taghavinia, N. *RSC Adv.* **2013**, 3(47), 25417–25422.
- [29] Grote, R. R.; Brown, S. J.; Driscoll, J. B.; Osgood, R. M.; Schuller, J. A. *Opt. Express* **2013**, 21(S5), A847.
- [30] Choi, H.; Chen, W. T.; Kamat, P. V. *ACS Nano*. **2012**, 6(5), 4418–4427.
- [31] Zhou, W.; Dridi, M.; Suh, J. Y.; Kim, C. H.; Co, D. T.; Wasielewski, M. R.; Schatz, G. C.; Odom, T. W. *Nat. Nanotechnol.* **2013**, 8(7), 506–511.

- [32] Yang, A.; Hoang, T. B.; Dridi, M.; Deeb, C.; Mikkelsen, M. H.; Schatz, G. C.; Odom, T. W. *Nat. Commun.* **2015**, *6*, 6939.
- [33] Anker, J. N.; Hall, W. P.; Lyandres, O.; Shah, N. C.; Zhao, J.; Van Duyne, R. P. *Nat. Mater.* **2008**, *7*(6), 442–453.
- [34] Homola, J. *Chem. Rev.* **2008**, *108*(2), 462–493.
- [35] Haes, A. J.; Hall, W. P.; Chang, L.; Klein, W. L.; Van Duyne, R. P. *Nano Lett.* **2004**, *4*(6), 1029–1034.
- [36] Zong, C.; Xu, M.; Xu, L.-J.; Wei, T.; Ma, X.; Zheng, X.-S.; Hu, R.; Ren, B. *Chem. Rev.* **2018**, *118*(10), 4946–4980.
- [37] Metzger, B.; Hentschel, M.; Giessen, H. *ACS Photonics* **2016**, *3*(8), 1336–1350.
- [38] Verma, P. *Chem. Rev.* **2017**, *117*(9), 6447–6466.
- [39] Wang, X.; Huang, S.-C.; Huang, T.-X.; Su, H.-S.; Zhong, J.-H.; Zeng, Z.-C.; Li, M.-H.; Ren, B. *Chem. Soc. Rev.* **2017**, *46*(13), 4020–4041.
- [40] Yeo, B. S.; Stadler, J.; Schmid, T.; Zenobi, R.; Zhang, W. *Chem. Phys. Lett.* **2009**, *472*(1–3), 1–13.
- [41] Sonntag, M. D.; Klingsporn, J. M.; Garibay, L. K.; Roberts, J. M.; Dieringer, J. A.; Seideman, T.; Scheidt, K. A.; Jensen, L.; Schatz, G. C.; Van Duyne, R. P. *J. Phys. Chem. C* **2012**, *116*(1), 478–483.
- [42] Duan, S.; Tian, G.; Ji, Y.; Shao, J.; Dong, Z.; Luo, Y. *J. Am. Chem. Soc.* **2015**, *137*(30), 9515–9518.
- [43] Zhang, R.; Zhang, Y.; Dong, Z. C.; Jiang, S.; Zhang, C.; Chen, L. G.; Zhang, L.; Liao, Y.; Aizpurua, J.; Luo, Y.; Yang, J. L.; Hou, J. G. *Nature* **2013**, *498*(7452), 82–6.
- [44] Wurtz, G. A.; Evans, P. R.; Hendren, W.; Atkinson, R.; Dickson, W.; Pollard, R. J.; Zayats, A. V.; Harrison, W.; Bower, C. *Nano Lett.* **2007**, *7*(5), 1297–1303.
- [45] Antosiewicz, T. J.; Apell, S. P.; Shegai, T. *ACS Photonics* **2014**, *1*(5), 454–463.
- [46] Chen, H.; Shao, L.; Woo, K. C.; Wang, J.; Lin, H.-Q. *J. Phys. Chem. C* **2012**, *116*(26), 14088–14095.

- [47] Ni, W.; Chen, H.; Su, J.; Sun, Z.; Wang, J.; Wu, H. *J. Am. Chem. Soc.* **2010**, *132*(13), 4806–4814.
- [48] Balci, S.; Kucukoz, B.; Balci, O.; Karatay, A.; Kocabas, C.; Yaglioglu, G. *ACS Photonics* **2016**, *3*(11), 2010–2016.
- [49] Dietze, D. R.; Mathies, R. A. *J. Phys. Chem. C* **2015**, *119*(18), 9980–9987.
- [50] Fofang, N. T.; Park, T. H.; Neumann, O.; Mirin, N. A.; Nordlander, P.; Halas, N. J. *Nano Lett.* **2008**, *8*(10), 3481–3487.
- [51] Thomas, R.; Thomas, A.; Pullanchery, S.; Joseph, L.; Somasundaran, S. M.; Swathi, R. S.; Gray, S. K.; Thomas, K. G. *ACS Nano* **2018**, *12*(1), 402–415.
- [52] Chen, H.; Ming, T.; Zhao, L.; Wang, F.; Sun, L.-D.; Wang, J.; Yan, C.-H. *Nano Today* **2010**, *5*(5), 494–505.
- [53] Moilanen, A. J.; Hakala, T. K.; Törmä, P. *ACS Photonics* **2018**, *5*(1), 54–64.
- [54] Govorov, A. O.; Fan, Z. *ChemPhysChem* **2012**, *13*(10), 2551–2560.
- [55] Ambjörnsson, T.; Mukhopadhyay, G.; Apell, S. P.; Käll, M. *Phys. Rev. B* **2006**, *73*(8), 085412.
- [56] Ben-Moshe, A.; Maoz, B. M.; Govorov, A. O.; Markovich, G. *Chem. Soc. Rev.* **2013**, *42*(16), 7028.
- [57] Levi-Belenkova, T.; Govorov, A. O.; Markovich, G. *J. Phys. Chem. C* **2016**, *120*(23), 12751–12756.
- [58] Sukharev, M.; Nitzan, A. *Phys. Rev. A* **2011**, *84*(4), 043802.
- [59] Sukharev, M.; Malinovskaya, S. A. *Mol. Phys.* **2015**, *113*(3-4), 392–396.
- [60] Sukharev, M.; Day, P. N.; Pachter, R. **2015**.
- [61] Sukharev, M.; Seideman, T.; Gordon, R. J.; Salomon, A.; Prior, Y. *ACS Nano*. **2014**, *8*(1), 807–817.
- [62] Taflove, A.; Hagness, S. C. *Computational Electrodynamics: The Finite-difference Time-domain Method*, Artech House antennas and propagation library; Artech House, 2005.
- [63] Yee, K. S. *IEEE Trans. Antennas Propag.* **1966**, *14*(3), 302–307.

- [64] Fujii, M.; Tahara, M.; Sakagami, I.; Freude, W.; Russer, P. *IEEE J. Quantum Electron.* **2004**, *40*(2), 175–182.
- [65] Roden, J. A.; Gedney, S. D. *Microw. Opt. Technol. Lett.* **2000**, *27*(5), 334–339.
- [66] Berenger, J. P. *J. Comput. Phys.* **1994**, *114*(2), 185–200.
- [67] Bérenger, J. P. *IEEE Trans. Antennas Propag.* **1997**, *45*(3), 466–473.
- [68] Chew, W. C.; Weedon, W. H. *Microw. Opt. Technol. Lett.* **1994**, *7*(13), 599–604.
- [69] Rappaport, C. M. *IEEE Microw. Guid. Wave Lett.* **1995**, *5*(3), 90–92.
- [70] Umashankar, K.; Taflove, A. *IEEE Trans. Electromagn. Compat.* **1982**, *EMC-24*(4), 397–405.
- [71] Taflove, A., Oskooi, A., Johnson, S. G., Eds. *Advances in FDTD Computational Electrodynamics: Photonics and Nanotechnology*; Artech House: Boston, MA, 2013.
- [72] Tan, T.; Potter, M. *IEEE Antennas Wirel. Propag. Lett.* **2007**, *6*, 144–148.
- [73] Tan, T.; Potter, M. *IEEE Antennas Wirel. Propag. Lett.* **2009**, *8*, 505–508.
- [74] Tan, T.; Potter, M. *IEEE Trans. Antennas Propag.* **2010**, *58*(8), 2641–2648.
- [75] Tan, T.; Potter, M. *IEEE Trans. Antennas Propag.* **2010**, *58*(3), 824–831.
- [76] Kim, J. Y.; Voznyy, O.; Zhitomirsky, D.; Sargent, E. H. *Adv. Mater.* **2013**, *25*(36), 4986–5010.
- [77] Ureña, E. B.; Kreuzer, M. P.; Itzhakov, S.; Rigneault, H.; Quidant, R.; Oron, D.; Wenger, J. *Adv. Mater.* **2012**, *24*(44), OP314—OP320.
- [78] Brolo, A. G.; Kwok, S. C.; Cooper, M. D.; Moffitt, M. G.; Wang, C.-W.; Gordon, R.; Riordon, J.; Kavanagh, K. L. *J. Phys. Chem. B* **2006**, *110*(16), 8307–8313.
- [79] Zhang, L.; Song, Y.; Fujita, T.; Zhang, Y.; Chen, M.; Wang, T.-H. *Adv. Mater.* **2014**, *26*(8), 1289–1294.
- [80] Song, J.-H.; Atay, T.; Shi, S.; Urabe, H.; Nurmikko, A. V. *Nano Lett.* **2005**, *5*(8), 1557–1561.
- [81] Sun, D.; Tian, Y.; Zhang, Y.; Xu, Z.; Sfeir, M. Y.; Cotlet, M.; Gang, O. *ACS Nano* **2015**.

- [82] Mendes, M. J.; Hernández, E.; López, E.; García-Linares, P.; Ramiro, I.; Artacho, I.; Antolín, E.; Tobías, I.; Martí, A.; Luque, A. *Nanotechnology* **2013**, *24*(34), 345402.
- [83] Nelayah, J.; Kociak, M.; Stéphan, O.; Abajo, F.; Tencé, M.; Henrard, L.; Taverna, D.; Isabel, P.-S.; Luis, L.-M.; Colliex, C. *Nat Phys* **2007**, *3*(5), 348–353.
- [84] Shishodia, M.; Perera, A. *J. Appl. Phys.* **2011**, *109*(4), 43108.
- [85] Atwater, H. A.; Polman, A. *Nat. Mater.* **2010**, *9*(3), 205–213.
- [86] Pillai, S.; Green, M. A. *Sol. Energy Mater. Sol. Cells* **2010**, *94*(9), 1481–1486.
- [87] Gan, Q.; Bartoli, F. J.; Kafafi, Z. H. *Adv. Mater.* **2013**, *25*(17), 2385–2396.
- [88] Gu, X.; Qiu, T.; Zhang, W.; Chu, P. K. *Nanoscale Res. Lett.* **2011**, *6*(1), 199.
- [89] Caruge, J. M.; Halpert, J. E.; Wood, V.; Bulović, V.; Bawendi, M. G. *Nat. Photonics* **2008**, *2*(4), 247–250.
- [90] Kwon, M. K.; Kim, J. Y.; Kim, B. H.; Park, I. K.; Cho, C. Y.; Byeon, C. C.; Park, S. J. *Adv. Mater.* **2008**, *20*(7), 1253–1257.
- [91] Klingsporn, J.; Jiang, N.; Pozzi, E.; Sonntag, M.; Chulhai, D.; Seideman, T.; Jensen, L.; Hersam, M.; Duyne, R. *J. Am. Chem. Soc.* **2014**, *136*(10), 3881–3887.
- [92] Sonntag, M.; Chulhai, D.; Seideman, T.; Jensen, L.; Duyne, R. *J. Am. Chem. Soc.* **2013**, *135*(45), 17187–17192.
- [93] Klingsporn, J.; Sonntag, M.; Seideman, T.; Duyne, R. *J. Phys. Chem. Lett.* **2014**, *5*(1), 106–110.
- [94] Pozzi, E.; Sonntag, M.; Jiang, N.; Chiang, N.; Seideman, T.; Hersam, M.; Duyne, R. *J. Phys. Chem. Lett.* **2014**, *5*(15), 2657–2661.
- [95] Jiang, N.; Chiang, N.; Madison, L.; Pozzi, E.; Wasielewski, M.; Seideman, T.; Ratner, M.; Hersam, M.; Schatz, G.; Duyne, R. *Nano Lett.* **2016**, *16*(6), 3898–3904.
- [96] Sobhani, A.; Knight, M. W.; Wang, Y.; Zheng, B.; King, N. S.; Brown, L. V.; Fang, Z.; Nordlander, P.; Halas, N. J. *Nat. Commun.* **2013**, *4*, 1643.
- [97] Ferri, C. G. L.; Inman, R. H.; Rich, B.; Gopinathan, A.; Khine, M.; Ghosh, S. *Opt. Mater. Express* **2013**, *3*(3), 383.

- [98] Raza, S.; Toscano, G.; Jauho, A.-P.; Wubs, M.; Mortensen, N. *Phys. Rev. B* **2011**, *84*(12), 121412.
- [99] Raza, S.; Stenger, N.; Kadkhodazadeh, S.; Fischer, S.; Kostesha, N.; Jauho, A.-P.; Burrows, A.; Wubs, M.; Mortensen, N. *Nanophotonics* **2013**, *2*(2), 131–138.
- [100] Jeffrey, M.; Gray, S.; Schatz, G. *Phys. Rev. Lett.* **2009**, *103*(9), 97403.
- [101] Wu, X.; K.Gray, S.; Pelton, M. *Opt. Express* **2010**, *18*(23), 23633–23645.
- [102] Salomon, A.; Gordon, R. J.; Prior, Y.; Seideman, T.; Sukharev, M. *Phys. Rev. Lett.* **2012**, *109*(August), 1–5.
- [103] Galanty, M.; Yochelis, S.; Stern, L.; Dujovne, I.; Levy, U.; Paltiel, Y. *J. Phys. Chem. C* **2015**, *119*(44), 24991–24995.
- [104] Gaspar, D.; Pimentel, a. C.; Mateus, T.; Leitão, J. P.; Soares, J.; Falcão, B. P.; Araújo, A.; Vicente, A.; Filonovich, S. a.; Águas, H.; Martins, R.; Ferreira, I. *Sci. Rep.* **2013**, *3*(1), 1469.
- [105] Carretero-Palacios, S.; Jiménez-Solano, A.; Míguez, H. *ACS Energy Lett.* **2016**, *1*(1), 323–331.
- [106] Saliba, M.; Zhang, W.; Burlakov, V. M.; Stranks, S. D.; Sun, Y.; Ball, J. M.; Johnston, M. B.; Goriely, A.; Wiesner, U.; Snaith, H. J. *Adv. Funct. Mater.* **2015**, *25*(31), 5038–5046.
- [107] Dong, H.; Lei, T.; Yuan, F.; Xu, J.; Niu, Y.; Jiao, B.; Zhang, Z.; Ding, D.; Hou, X.; Wu, Z. *Org. Electron.* **2018**, *60*, 1–8.
- [108] Zhou, D.; Liu, D.; Jin, J.; Chen, X.; Xu, W.; Yin, Z.; Pan, G.; Li, D.; Song, H. *J. Mater. Chem. A* **2017**, *5*(32), 16559–16567.
- [109] Dong, Y.; Gu, Y.; Zou, Y.; Song, J.; Xu, L.; Li, J.; Xue, J.; Li, X.; Zeng, H. *Small* **2016**, *12*(40), 5622–5632.
- [110] Willets, K. A.; Van Duyne, R. P. *Annu. Rev. Phys. Chem.* **2007**, *58*(1), 267–297.
- [111] Ciraci, C.; Hill, R. T.; Mock, J. J.; Urzhumov, Y.; Fernández-Domínguez, A. I.; Maier, S. A.; Pendry, J. B.; Chilkoti, A.; Smith, D. R. *Science* **2012**, *337*(6098), 1072–1074.
- [112] Khatua, S.; Paulo, P. M.; Yuan, H.; Gupta, A.; Zijlstra, P.; Orrit, M. *ACS Nano* **2014**, *8*(5), 4440–4449.

- [113] Wu, D. M.; García-Etxarri, A.; Salleo, A.; Dionne, J. A. *J. Phys. Chem. Lett.* **2014**, *5*(22), 4020–4031.
- [114] Le, T. H. H.; Morita, A.; Mawatari, K.; Kitamori, T.; Tanaka, T. *ACS Photonics* **2018**, page acsphotronics.8b00398.
- [115] Chan, Y.-H.; Chen, J.; Liu, Q.; Wark, S. E.; Son, D. H.; Batteas, J. D. *Anal. Chem.* **2010**, *82*(9), 3671–3678.
- [116] Fu, Y.; Zhang, J.; Lakowicz, J. R. *J. Am. Chem. Soc.* **2010**, *132*, 5540–5541.
- [117] Delga, A.; Feist, J.; Bravo-Abad, J.; Garcia-Vidal, F. J. *Phys. Rev. Lett.* **2014**, *112*(25), 253601.
- [118] Andersen, M. L.; Stobbe, S.; Sørensen, A. S.; Lodahl, P. *Nat. Phys.* **2011**, *7*(3), 215–218.
- [119] Yam, C.; Meng, L.; Zhang, Y.; Chen, G. *Chem. Soc. Rev.* **2015**, *44*(7), 1763–1776.
- [120] Chen, H.; Schatz, G. C.; Ratner, M. A. In *Sol. Energy Convers. Dyn. Interfacial Electron Excit. Transf.*; Piotr Piotrowiak., Ed., number 8; The Royal Society of Chemistry: Cambridge, UK, 1 ed., 2013; chapter 4, pages 111–134.
- [121] Chen, H.; McMahon, J. M.; Ratner, M. A.; Schatz, G. C. *J. Phys. Chem. C* **2010**, *114*(34), 14384–14392.
- [122] Megow, J.; May, V. *Chem. Phys.* **2014**, *428*, 6–13.
- [123] Ruggenthaler, M.; Flick, J.; Pellegrini, C.; Appel, H.; Tokatly, I. V.; Rubio, A. *Phys. Rev. A - At. Mol. Opt. Phys.* **2014**, *90*(1), 1–29.
- [124] Sukharev, M. *J. Chem. Phys.* **2014**, *141*, 084712.
- [125] Sukharev, M.; Freifeld, N.; Nitzan, A. *J. Phys. Chem. C* **2014**, *118*, 10545–10551.
- [126] Blake, A.; Sukharev, M. *J. Chem. Phys.* **2016**, *146*(8), 084704.
- [127] Li, T. E.; Nitzan, A.; Sukharev, M.; Martinez, T.; Chen, H. T.; Subotnik, J. E. *Phys. Rev. A* **2018**, *97*(3).
- [128] Poltavtsev, S. V.; Salewski, M.; Kapitonov, Y. V.; Yugova, I. A.; Akimov, I. A.; Schneider, C.; Kamp, M.; Höfling, S.; Yakovlev, D. R.; Kavokin, A. V.; Bayer, M. *Phys. Rev. B* **2016**, *93*(12).

- [129] Breuer, H. P.; Petruccione, F. *The Theory of Open Quantum Systems*; OUP Oxford, 2007.
- [130] Standridge, S. D.; Schatz, G. C.; Hupp, J. T. *J. Am. Chem. Soc.* **2009**, *131*(24), 8407–8409.
- [131] Mandel, L.; Wolf, E. *Optical Coherence and Quantum Optics*; Cambridge University Press: New York, NY, 1995.
- [132] Soto, J.; Fernández, D. J.; Centeno, S. P.; López Tocón, I.; Otero, J. C. *Langmuir* **2002**, *18*(8), 3100–3104.
- [133] Zhang, R.; Zhang, Y.; Dong, Z. C.; Jiang, S.; Zhang, C.; Chen, L. G.; Zhang, L.; Liao, Y.; Aizpurua, J.; Luo, Y.; Yang, J. L.; Hou, J. G. *Nature* **2013**, *498*(7452), 82–86.
- [134] Cecchet, F.; Lis, D.; Guthmuller, J.; Champagne, B.; Caudano, Y.; Silien, C.; Addin Mani, A.; Thiry, P. A.; Peremans, A. *ChemPhysChem* **2010**, *11*(3), 607–615.
- [135] Gehan, H.; Mangeney, C.; Aubard, J.; Levi, G.; Hohenau, A.; Krenn, J. R.; Lacaze, E.; Felidj, N. *J. Phys. Chem. Lett.* **2011**, *2*(8), 926–931.
- [136] Lacroix, J.-C.; Martin, P.; Lacaze, P.-C. *Annu. Rev. Anal. Chem* **2017**, *10*, 201–24.
- [137] Hiep, H. M.; Fujii, M.; Hayashi, S. *Appl. Phys. Lett.* **2007**, *91*(18), 183110.
- [138] Grote, R. R.; Brown, S. J.; Driscoll, J. B.; Osgood, R. M.; Schuller, J. A. *Opt. Express* **2013**, *21*(S5), A847.
- [139] Raziman, T. V.; Martin, O. J. F. *J. Phys. Chem. C* **2016**, *120*(37), 21037–21046.
- [140] Govorov, A. O.; Fan, Z.; Hernandez, P.; Slocik, J. M.; Naik, R. R. *Nano Lett.* **2010**, *10*(4), 1374–1382.
- [141] Trilling, A. K.; Harmsen, M. M.; Ruigrok, V. J.; Zuilhof, H.; Beekwilder, J. *Biosens. Bioelectron.* **2013**, *40*(1), 219–226.
- [142] Dyr, J.; Tichý, I.; Jiroušková, M.; Tobiška, P.; Slavk, R.; Homola, J.; Brynda, E.; Houska, M.; Suttner, J. *Sensors Actuators B Chem.* **1998**, *51*(1-3), 268–272.
- [143] Haes, A. J.; Zou, S.; Zhao, J.; Schatz, G. C.; Van Duyne, R. P. *J. Am. Chem. Soc.* **2006**, *128*(33), 10905–10914.
- [144] Brown, S. J.; DeCrescent, R. A.; Nakazono, D. M.; Willenson, S. H.; Ran, N. A.; Liu, X.; Bazan, G. C.; Nguyen, T.-Q.; Schuller, J. A. *Nano Lett.* **2017**, *17*(10), 6151–6156.

- [145] Gruber, M.; Mayr, M.; Lampe, T.; Gallheber, B.-C.; Scholz, B. J.; Brütting, W. *Appl. Phys. Lett.* **2015**, *106*(8), 083303.
- [146] Petoukhoff, C. E.; Shen, Z.; Jain, M.; Chang, A.; O'Carroll, D. M. *J. Photonics Energy* **2015**, *5*(1), 057002.
- [147] Guo, L.; Jackman, J. A.; Yang, H. H.; Chen, P.; Cho, N. J.; Kim, D. H. *Nano Today* **2015**, *10*(2), 213–239.
- [148] Päivänranta, B.; Merbold, H.; Giannini, R.; Büchi, L.; Gorelick, S.; David, C.; Löffler, J. F.; Feurer, T.; Ekinici, Y. *ACS Nano* **2011**, *5*(8), 6374–6382.
- [149] Purcell, T. A. R.; Galanty, M.; Yochelis, S.; Paltiel, Y.; Seideman, T. *J. Phys. Chem. C* **2016**, *120*(38), 21837–21842.
- [150] Bezen, L.; Yochelis, S.; Jayarathna, D.; Bhunia, D.; Achim, C.; Paltiel, Y. *Langmuir* **2018**, *34*(9), 3076–3081.
- [151] Abdulrahman, N. A.; Fan, Z.; Tonooka, T.; Kelly, S. M.; Gadegaard, N.; Hendry, E.; Govorov, A. O.; Kadodwala, M. *Nano Lett.* **2012**, *12*(2), 977–983.
- [152] Hendry, E.; Carpy, T.; Johnston, J.; Popland, M.; Mikhaylovskiy, R. V.; Laphorn, A. J.; Kelly, S. M.; Barron, L. D.; Gadegaard, N.; Kadodwala, M. *Nat. Nanotechnol.* **2010**, *5*(11), 783–787.
- [153] Wang, R. Y.; Wang, P.; Liu, Y.; Zhao, W.; Zhai, D.; Hong, X.; Ji, Y.; Wu, X.; Wang, F.; Zhang, D.; Zhang, W.; Liu, R.; Zhang, X. *J. Phys. Chem. C* **2014**, *118*(18), 9690–9695.
- [154] Xu, L.; Xu, Z.; Ma, W.; Liu, L.; Wang, L.; Kuang, H.; Xu, C. *J. Mater. Chem. B* **2013**, *1*(35), 4478.
- [155] Wu, T.; Ren, J.; Wang, R.; Zhang, X. *J. Phys. Chem. C* **2014**, *118*(35), 20529–20537.
- [156] Pendry, J. B. *Science* **2004**, *306*(5700), 1353–1355.
- [157] Liu, N.; Guo, H.; Fu, L.; Kaiser, S.; Schweizer, H.; Giessen, H. *Nat. Mater.* **2008**, *7*(1), 31–37.
- [158] Jia, X.; Meng, Q.; Yuan, C.; Zhou, Z.; Wang, X. *Optik (Stuttg.)* **2016**, *127*(14), 5738–5742.
- [159] Abadla, M. M.; Taya, S. A. *Opt. - Int. J. Light Electron Opt.* **2017**, *131*, 562–573.

- [160] Gansel, J. K.; Thiel, M.; Rill, M. S.; Decker, M.; Bade, K.; Saile, V.; Von Freymann, G.; Linden, S.; Wegener, M. *Science* **2009**, *325*(5947), 1513–1515.
- [161] Gansel, J. K.; Latzel, M.; Frölich, A.; Kaschke, J.; Thiel, M.; Wegener, M. *Appl. Phys. Lett.* **2012**, *100*(10), 101109.
- [162] Wang, J.; Shen, Z.; Wu, W. *Appl. Phys. Lett.* **2017**, *111*(11), 113503.
- [163] Zhang, S.; Zhou, J.; Park, Y. S.; Rho, J.; Singh, R.; Nam, S.; Azad, A. K.; Chen, H. T.; Yin, X.; Taylor, A. J.; Zhang, X. *Nat. Commun.* **2012**, *3*(1), 942.
- [164] Schreiber, R.; Luong, N.; Fan, Z.; Kuzyk, A.; Nickels, P. C.; Zhang, T.; Smith, D. M.; Yurke, B.; Kuang, W.; Govorov, A. O.; Liedl, T. *Nat. Commun.* **2013**, *4*(1), 2948.
- [165] Zhao, R.; Zhou, J.; Koschny, T.; Economou, E. N.; Soukoulis, C. M. *Phys. Rev. Lett.* **2009**, *103*(10).
- [166] Canaguier-Durand, A.; Hutchison, J. A.; Genet, C.; Ebbesen, T. W. *New J. Phys.* **2013**, *15*(12), 123037.
- [167] Wang, M.; Li, H.; Dong, Y.; Zhang, X.; Du, M.; Wang, R.; Xu, T.; Wu, J. *Opt. Mater. (Amst.)* **2016**, *62*, 411–418.
- [168] Song, C.; Blaber, M. G.; Zhao, G.; Zhang, P.; Fry, H. C.; Schatz, G. C.; Rosi, N. L. *Nano Lett.* **2013**, *13*(7), 3256–3261.
- [169] Wu, X.; Xu, L.; Ma, W.; Liu, L.; Kuang, H.; Kotov, N. A.; Xu, C. *Adv. Mater.* **2016**, *28*(28), 5907–5915.
- [170] Chen, Z.; Lan, X.; Chiu, Y. C.; Lu, X.; Ni, W.; Gao, H.; Wang, Q. *ACS Photonics* **2015**, *2*(3), 392–397.
- [171] Yin, X.; Schäferling, M.; Michel, A.-K. U.; Tittel, A.; Wuttig, M.; Taubner, T.; Giessen, H. *Nano Lett.* **2015**, *15*(7), 4255–4260.
- [172] Luo, Y.; Chi, C.; Jiang, M.; Li, R.; Zu, S.; Li, Y.; Fang, Z. *Adv. Opt. Mater.* **2017**, *5*(16), 1700040.
- [173] Valev, V. K.; Baumberg, J. J.; Sibilica, C.; Verbiest, T. *Adv. Mater.* **2013**, *25*(18), 2517–2534.
- [174] Slocik, J. M.; Govorov, A. O.; Naik, R. R. *Nano Lett.* **2011**, *11*(2), 701–705.

- [175] Schaaff, T. G.; Whetten, R. L. *J. Phys. Chem. B* **2000**, *104*(12), 2630–2641.
- [176] Sánchez-Castillo, A.; Noguez, C.; Garzón, I. L. *J. Am. Chem. Soc.* **2010**, *132*(5), 1504–1505.
- [177] Fan, Z.; Govorov, A. O. *Nano Lett.* **2012**, *12*(6), 3283–3289.
- [178] Maoz, B. M.; Chaikin, Y.; Tesler, A. B.; Bar Elli, O.; Fan, Z.; Govorov, A. O.; Markovich, G. *Nano Lett.* **2013**, *13*(3), 1203–1209.
- [179] Semichaevsky, A.; Akyurtlu, A.; Kern, D.; Werner, D. H.; Bray, M. G. *IEEE Trans. Antennas Propag.* **2006**, *54*(3), 925–932.
- [180] Akyurtlu, A.; Werner, D. *IEEE Trans. Antennas Propag.* **2004**, *52*(2), 416–425.
- [181] Pereda, J. A.; Grande, A.; González, O.; Vegas, Á. *IEEE Antennas Wirel. Propag. Lett.* **2006**, *5*(1), 327–330.
- [182] Mohammadi-Baghaee, R.; Dehmollaian, M.; Rashed-Mohassel, J. In *2017 11th Eur. Conf. Antennas Propag.*, pages 525–528. IEEE, 2017.
- [183] Purcell, T. A. R.; Yochelis, S.; Paltiel, Y.; Seideman, T. *J. Phys. Chem. C* **2018**, page acs.jpcc.8b05051.
- [184] Lindell, I. V.; Sihvola, A. H.; Tretyakov, S. A.; Viitanen, A. J. *Electromagnetic Waves in Chiral and Bi-Isotropic Media*; Artech House: Boston, MA, 1st ed., 1994.
- [185] Taflov, A.; Hagness, S. C. *Computational Electrodynamics*; Artech House, Inc.: Norwood, MA, third ed., 2005.
- [186] Djorović, A.; Meyer, M.; Darby, B. L.; Le Ru, E. C. *ACS Omega* **2017**, *2*(5), 1804–1811.
- [187] Yamaguchi, T.; Ichihashi, Y.; Mishima, T.; Matsubara, N.; Yamanishi, T. *IEEE J. Photovoltaics*. **2014**, *4*(6), 1433–1435.
- [188] Levelized Cost and Levelized Avoided Cost of New Generation Resources in the Annual Energy Outlook 2018. U.S. Energy Information Administration. **2018**.
- [189] Powell, D. M.; Winkler, M. T.; Choi, H. J.; Simmons, C. B.; Needleman, D. B.; Buonassisi, T. *Energy Environ. Sci.* **2012**, *5*(3), 5874.
- [190] O'Regan, B.; Grätzel, M. *Nature*. **1991**, *353*(6346), 737–740.

- [191] Kakiage, K.; Aoyama, Y.; Yano, T.; Oya, K.; Fujisawa, J. I.; Hanaya, M. *Chem. Commun.* **2015**, 51(88), 15894–15897.
- [192] Yoshikawa, K.; Kawasaki, H.; Yoshida, W.; Irie, T.; Konishi, K.; Nakano, K.; Uto, T.; Adachi, D.; Kanematsu, M.; Uzu, H.; Yamamoto, K. *Nat. Energy* **2017**, 2(5), 17032.
- [193] Hardin, B. E.; Snaith, H. J.; McGehee, M. D. *Nat. Photon.* **2012**, 6(3), 162–169.
- [194] Li, L.-L.; Diau, E. W.-G. *Chem. Soc. Rev.* **2013**, pages 291–304.
- [195] Yella, A.; Lee, H.; Tsao, H. K.; Yi, C.; Chandiran, A. K.; Nazeeruddin, M. K.; Diau, E. W.; Yeh, C.; Zakeeruddin, S.; Grätzel, M. *Science* **2011**, 334(6056), 629–634.
- [196] Snaith, H. J. *Adv. Funct. Mater.* **2010**, 20(1), 13–19.
- [197] Zhao, G.; Kozuka, H.; Yoko, T. *Sol. Energy Mater. Sol. Cells.* **1997**, 46(3), 219.
- [198] Standridge, S. D.; Schatz, G. C.; Hupp, J. T. *Langmuir.* **2009**, 25(5), 2596–2600.
- [199] Sheehan, S. W.; Noh, H.; Brudvig, G. W.; Cao, H.; Schmittenmaer, C. A. *J. Phys. Chem. C.* **2013**, 117(2), 927–934.
- [200] Song, M.-K.; Rai, P.; Ko, K.-J.; Jeon, S.-H.; Chon, B.-S.; Lee, C.-H.; Yu, Y.-T. *RSC Adv.* **2014**, 4(7), 3529–3535.
- [201] Dong, H.; Wu, Z.; El-Shafei, A.; Xia, B.; Xi, J.; Ning, S.; Jiao, B.; Hou, X. *J. Mater. Chem. A* **2015**, 3, 4659–4668.
- [202] Holland, J. H. *Adaptation in natural and artificial systems: an introductory analysis with applications to biology, control, and artificial intelligence*; University of Michigan Press, 1975.
- [203] Yang, X.-S. *Nature-Inspired Optimization Algorithms*; Elsevier Inc, 2014.
- [204] Hagfeldt, A.; Boschloo, G.; Sun, L.; Kloo, L.; Pettersson, H. *Chem. Rev.* **2010**, 110(11), 6595–6663.
- [205] Reference Solar Spectral Irradiance: Air Mass 1.5. The National Renewable Energy Laboratory.
- [206] Yelk, J.; Sukharev, M.; Seideman, T. *J. Chem. Phys.* **2008**, 129(6), 064706.
- [207] Sukharev, M.; Seideman, T. *J. Phys. B At. Mol. Opt. Phys.* **2007**, 40, S283–S298.

- [208] Sanchez-de Armas, R.; Oviedo Lopez, J.; A. San-Miguel, M.; Sanz, J. F.; Ordejon, P.; Pruneda, M. *J. Chem. Theory Comput.* **2010**, *6*(9), 2856–2865.
- [209] Nazeeruddin, M. K.; De Angelis, F.; Fantacci, S.; Selloni, A.; Viscardi, G.; Liska, P.; Ito, S.; Takeru, B.; Grätzel, M. *J. Am. Chem. Soc.* **2005**, *127*(48), 16835–16847.
- [210] Chandrasekharam, M.; Rajkumar, G.; Suresh, T.; Rao, C. S.; Reddy, P. Y.; Yum, J.-H.; Nazeeruddin, M. K.; Graetzel, M. *Adv. Optoelectron.* **2011**, *2011*, 1–10.

## APPENDIX A

**Consistency Conditions for TF/SF**

All the consistency equation displayed here are a combination of those given in Taflove and Hagness<sup>62</sup> and Taflove, et al.<sup>71</sup> Along the  $i_0$  face the fields are updated with

For  $i = i_0$ ,  $j = j_0 + \frac{1}{2}, \dots, j_1 - \frac{1}{2}$ , and  $k = k_0, \dots, k_1$

$$(A.1) \quad E_y|_{i_0,j,k}^{n+1} = \left\{ E_y|_{i_0,j,k}^{n+1} \right\}_{2.5b} + \frac{\Delta_t}{\epsilon_{i_0,j,k}\Delta_x} H_{z,inc}|_{i_r+\frac{m_y-m_x}{2}}^{n+\frac{1}{2}}$$

For  $i = i_0$ ,  $j = j_0, \dots, j_1$ , and  $k = k_0 + \frac{1}{2}, \dots, k_1 - \frac{1}{2}$

$$(A.2) \quad E_z|_{i_0,j,k}^{n+1} = \left\{ E_z|_{i_0,j,k}^{n+1} \right\}_{2.5c} - \frac{\Delta_t}{\epsilon_{i_0,j,k}\Delta_x} H_{y,inc}|_{i_r+\frac{m_z-m_x}{2}}^{n+\frac{1}{2}}$$

For  $i = i_0 - \frac{1}{2}$ ,  $j = j_0 + \frac{1}{2}, \dots, j_1 - \frac{1}{2}$ , and  $k = k_0, \dots, k_1$

$$(A.3) \quad H_z|_{i_0,j,k}^{n+\frac{1}{2}} = \left\{ H_z|_{i_0,j,k}^{n+\frac{1}{2}} \right\}_{2.5f} + \frac{\Delta_t}{\mu_{i_0,j,k}\Delta_x} E_{y,inc}|_{i_r+m_x+\frac{m_y}{2}}^n$$

For  $i = i_0 - \frac{1}{2}$ ,  $j = j_0, \dots, j_1$ , and  $k = k_0 + \frac{1}{2}, \dots, k_1 - \frac{1}{2}$

$$(A.4) \quad H_y|_{i_0,j,k}^{n+\frac{1}{2}} = \left\{ H_y|_{i_0,j,k}^{n+\frac{1}{2}} \right\}_{2.5e} - \frac{\Delta_t}{\mu_{i_0,j,k}\Delta_x} E_{z,inc}|_{i_r+m_x+\frac{m_z}{2}}^n$$

Along the  $i_1$  face the fields are updated with

For  $i = i_1$ ,  $j = j_0 + \frac{1}{2}, \dots, j_1 - \frac{1}{2}$ , and  $k = k_0, \dots, k_1$

$$(A.5) \quad E_y|_{i_1,j,k}^{n+1} = \left\{ E_y|_{i_1,j,k}^{n+1} \right\}_{2.5b} - \frac{\Delta_t}{\epsilon_{i_1,j,k}\Delta_x} H_{z,inc}|_{i_r+\frac{m_y+m_x}{2}}^{n+\frac{1}{2}}$$

For  $i = i_1, j = j_0, \dots, j_1$ , and  $k = k_0 + \frac{1}{2}, \dots, k_1 - \frac{1}{2}$

$$(A.6) \quad E_z|_{i_1, j, k}^{n+1} = \left\{ E_z|_{i_1, j, k}^{n+1} \right\}_{2.5c} + \frac{\Delta_t}{\epsilon_{i_1, j, k} \Delta_x} H_{y, inc}|_{i_r + \frac{m_z + m_x}{2}}^{n + \frac{1}{2}}$$

For  $i = i_1 + \frac{1}{2}, j = j_0 + \frac{1}{2}, \dots, j_1 - \frac{1}{2}$ , and  $k = k_0, \dots, k_1$

$$(A.7) \quad H_z|_{i_1, j, k}^{n + \frac{1}{2}} = \left\{ H_z|_{i_1, j, k}^{n + \frac{1}{2}} \right\}_{2.5f} - \frac{\Delta_t}{\mu_{i_1, j, k} \Delta_x} E_{y, inc}|_{i_r + \frac{m_y}{2}}^n$$

For  $i = i_1 + \frac{1}{2}, j = j_0, \dots, j_1$ , and  $k = k_0 + \frac{1}{2}, \dots, k_1 - \frac{1}{2}$

$$(A.8) \quad H_y|_{i_1, j, k}^{n + \frac{1}{2}} = \left\{ H_y|_{i_1, j, k}^{n + \frac{1}{2}} \right\}_{2.5e} + \frac{\Delta_t}{\mu_{i_1, j, k} \Delta_x} E_{z, inc}|_{i_r + \frac{m_z}{2}}^n$$

Along the  $j_0$  face the fields are updated with

For  $i = i_0, \dots, i_1, j = j_0$ , and  $k = k_0 + \frac{1}{2}, \dots, k_1 - \frac{1}{2}$

$$(A.9) \quad E_z|_{i, j_0, k}^{n+1} = \left\{ E_z|_{i, j_0, k}^{n+1} \right\}_{2.5c} + \frac{\Delta_t}{\epsilon_{i, j_0, k} \Delta_y} H_{x, inc}|_{i_r + \frac{m_z - m_y}{2}}^{n + \frac{1}{2}}$$

For  $i = i_0 + \frac{1}{2}, \dots, i_1 - \frac{1}{2}, j = j_0$ , and  $k = k_0, \dots, k_1$

$$(A.10) \quad E_x|_{i, j_0, k}^{n+1} = \left\{ E_x|_{i, j_0, k}^{n+1} \right\}_{2.5a} - \frac{\Delta_t}{\epsilon_{i, j_0, k} \Delta_y} H_{z, inc}|_{i_r + \frac{m_x - m_y}{2}}^{n + \frac{1}{2}}$$

For  $i = i_0, \dots, i_1, j = j_0$ , and  $k = k_0 + \frac{1}{2}, \dots, k_1 - \frac{1}{2}$

$$(A.11) \quad H_x|_{i, j_0, k}^{n + \frac{1}{2}} = \left\{ H_x|_{i, j_0, k}^{n + \frac{1}{2}} \right\}_{2.5d} + \frac{\Delta_t}{\mu_{i, j_0, k} \Delta_y} E_{z, inc}|_{i_r + m_y + \frac{m_z}{2}}^n$$

For  $i = i_0 + \frac{1}{2}, \dots, i_1 - \frac{1}{2}$ ,  $j = j_0$ , and  $k = k_0, \dots, k_1$

$$(A.12) \quad H_z|_{i,j_0,k}^{n+\frac{1}{2}} = \left\{ H_z|_{i,j_0,k}^{n+\frac{1}{2}} \right\}_{2.5f} - \frac{\Delta_t}{\mu_{i,j_0,k}\Delta_y} E_{x,inc}|_{i_r+m_y+\frac{m_x}{2}}^n$$

Along the  $j_1$  face the fields are updated with

For  $i = i_0, \dots, i_1$ ,  $j = j_1$ , and  $k = k_0 + \frac{1}{2}, \dots, k_1 - \frac{1}{2}$

$$(A.13) \quad E_z|_{i,j_1,k}^{n+1} = \left\{ E_z|_{i,j_1,k}^{n+1} \right\}_{2.5c} - \frac{\Delta_t}{\epsilon_{i,j_1,k}\Delta_y} H_{x,inc}|_{i_r+\frac{m_z+m_y}{2}}^{n+\frac{1}{2}}$$

For  $i = i_0 + \frac{1}{2}, \dots, i_1 - \frac{1}{2}$ ,  $j = j_1$ , and  $k = k_0, \dots, k_1$

$$(A.14) \quad E_x|_{i,j_1,k}^{n+1} = \left\{ E_x|_{i,j_1,k}^{n+1} \right\}_{2.5a} + \frac{\Delta_t}{\epsilon_{i,j_1,k}\Delta_y} H_{z,inc}|_{i_r+\frac{m_x+m_y}{2}}^{n+\frac{1}{2}}$$

For  $i = i_0, \dots, i_1$ ,  $j = j_1$ , and  $k = k_0 + \frac{1}{2}, \dots, k_1 - \frac{1}{2}$

$$(A.15) \quad H_x|_{i,j_1,k}^{n+\frac{1}{2}} = \left\{ H_x|_{i,j_1,k}^{n+\frac{1}{2}} \right\}_{2.5d} - \frac{\Delta_t}{\mu_{i,j_1,k}\Delta_y} E_{z,inc}|_{i_r+\frac{m_z}{2}}^n$$

For  $i = i_0 + \frac{1}{2}, \dots, i_1 - \frac{1}{2}$ ,  $j = j_1$ , and  $k = k_0, \dots, k_1$

$$(A.16) \quad H_z|_{i,j_1,k}^{n+\frac{1}{2}} = \left\{ H_z|_{i,j_1,k}^{n+\frac{1}{2}} \right\}_{2.5f} + \frac{\Delta_t}{\mu_{i,j_1,k}\Delta_y} E_{x,inc}|_{i_r+\frac{m_x}{2}}^n$$

Along the  $k_0$  face the fields are updated with

For  $i = i_0 + \frac{1}{2}, \dots, i_1 - \frac{1}{2}$ ,  $j = j_0, \dots, j_1$ , and  $k = k_0$

$$(A.17) \quad E_x|_{i,j,k_0}^{n+1} = \left\{ E_x|_{i,j,k_0}^{n+1} \right\}_{2.5a} + \frac{\Delta_t}{\epsilon_{i,j,k_0}\Delta_z} H_{y,inc}|_{i_r+\frac{m_x-m_z}{2}}^{n+\frac{1}{2}}$$

For  $i = i_0, \dots, i_1, j = j_0 + \frac{1}{2}, \dots, j_1 - \frac{1}{2}$ , and  $k = k_0$

$$(A.18) \quad E_y|_{i,j,k_0}^{n+1} = \left\{ E_y|_{i,j,k_0}^{n+1} \right\}_{2.5b} - \frac{\Delta_t}{\epsilon_{i,j,k_0} \Delta_z} H_{x,inc}|_{i_r + \frac{m_x - m_z}{2}}^{n + \frac{1}{2}}$$

For  $i = i_0 + \frac{1}{2}, \dots, i_1 - \frac{1}{2}, j = j_0, \dots, j_1$ , and  $k = k_0$

$$(A.19) \quad H_y|_{i,j,k_0}^{n + \frac{1}{2}} = \left\{ H_y|_{i,j,k_0}^{n + \frac{1}{2}} \right\}_{2.5e} + \frac{\Delta_t}{\mu_{i,j,k_0} \Delta_z} E_{x,inc}|_{i_r + m_z + \frac{m_x}{2}}^n$$

For  $i = i_0, \dots, i_1, j = j_0 + \frac{1}{2}, \dots, j_1 - \frac{1}{2}$ , and  $k = k_0$

$$(A.20) \quad H_x|_{i,j,k_0}^{n + \frac{1}{2}} = \left\{ H_x|_{i,j,k_0}^{n + \frac{1}{2}} \right\}_{2.5d} - \frac{\Delta_t}{\mu_{i,j,k_0} \Delta_z} E_{y,inc}|_{i_r + m_z + \frac{m_y}{2}}^n$$

Along the  $k_1$  face the fields are updated with

For  $i = i_0 + \frac{1}{2}, \dots, i_1 - \frac{1}{2}, j = j_0, \dots, j_1$ , and  $k = k_1$

$$(A.21) \quad E_x|_{i,j,k_1}^{n+1} = \left\{ E_x|_{i,j,k_1}^{n+1} \right\}_{2.5a} - \frac{\Delta_t}{\epsilon_{i,j,k_1} \Delta_z} H_{y,inc}|_{i_r + \frac{m_x + m_z}{2}}^{n + \frac{1}{2}}$$

For  $i = i_0, \dots, i_1, j = j_0 + \frac{1}{2}, \dots, j_1 - \frac{1}{2}$ , and  $k = k_1$

$$(A.22) \quad E_y|_{i,j,k_1}^{n+1} = \left\{ E_y|_{i,j,k_1}^{n+1} \right\}_{2.5b} + \frac{\Delta_t}{\epsilon_{i,j,k_1} \Delta_z} H_{x,inc}|_{i_r + \frac{m_x + m_z}{2}}^{n + \frac{1}{2}}$$

For  $i = i_0 + \frac{1}{2}, \dots, i_1 - \frac{1}{2}, j = j_0, \dots, j_1$ , and  $k = k_1$

$$(A.23) \quad H_y|_{i,j,k_1}^{n + \frac{1}{2}} = \left\{ H_y|_{i,j,k_1}^{n + \frac{1}{2}} \right\}_{2.5e} - \frac{\Delta_t}{\mu_{i,j,k_1} \Delta_z} E_{x,inc}|_{i_r + \frac{m_x}{2}}^n$$

For  $i = i_0, \dots, i_1, j = j_0 + \frac{1}{2}, \dots, j_1 - \frac{1}{2}$ , and  $k = k_1$

$$(A.24) \quad H_x|_{i,j,k_1}^{n + \frac{1}{2}} = \left\{ H_x|_{i,j,k_1}^{n + \frac{1}{2}} \right\}_{2.5d} + \frac{\Delta_t}{\mu_{i,j,k_1} \Delta_z} E_{y,inc}|_{i_r + \frac{m_y}{2}}^n$$

APPENDIX B

**Curriculum Vita**

# Thomas A. R. Purcell

PH.D. CANDIDATE · CHEMISTRY

907 Elmwood Ave, Apt B1, Evanston, IL, USA 60202

☎ 908-577-0044 | ✉ thomaspurcell2018@u.northwestern.edu | 📱 tpurcell90 | 🌐 Thomas Purcell

## Education

---

### Northwestern University

PH.D. IN PHYSICAL CHEMISTRY

*Evanston, IL*

*Sept. 2013 - Jul. 2018*

- Advisor: Prof. Tamar Seideman
- GPA: 3.97/4.00

### New York University

B.S. IN CHEMISTRY

*New York, NY*

*Sept. 2009 - May 2013*

- Advisor: Prof. Mark E. Tuckerman
- GPA: 3.689/4.00

## Skills

---

**Programming** Python, C/C++, Matlab, LaTeX, shell scripting

## Research Experience

---

### Northwestern University

RESEARCH ASSISTANT

*Evanston, IL*

*Sept. 2013 - Exp. May 2018*

- Advisor: Prof. Tamar Seideman
- Modeling optical properties of quantum emitter-metal hybrid systems
- Writing a general Maxwell-Liouville code
- Mentoring junior students on their Ph.D. projects

### Weizmann Institute of Science

VISITING SCHOLAR

*Rehovot, Israel*

*Jan. 2017 - Feb. 2017*

- Advisor: Prof. Leeor Kronik
- Developing a new interpolation scheme for calculating the nonlocal component of the coulomb potential for real space density functional theory methods

### Applied Materials

PROCESS ENGINEER, ADVANCED TECHNOLOGY GROUP

*Santa Clara, CA*

*May. 2013 - Aug. 2013*

- Supervisor: Dr. Subra Herle
- Synthesized and characterized a lithium thiophosphide electrolyte for an all solid state lithium ion battery.

### New York University

UNDERGRADUATE RESEARCHER

*New York, NY*

*Oct. 2010 - May. 2013*

- Advisor: Prof. Mark E. Tuckerman
- Used driven-Adiabatic Free Energy Dynamics to obtain free-energy surfaces of a small peptide based PDZ inhibitor

## Max Planck Institute for Polymer Research

SUMMER INTERN

Mainz, Germany

May. 2012 - Aug. 2012

- Advisor: Prof. Dr. Klaus Mullen
- Fabricated organic field effect transistors using compounds developed in the group using dip coating, drop casting and spin coating, and tested them in a nitrogen atmosphere

## Georgia Institute of Technology

REU STUDENT

Atlanta, Georgia

May. 2010 - Jul. 2010

- Advisor: Prof. Seth Marder
- Synthesized and characterized a series of dithiophenopyrroles and diselenopyrroles to test the effects of atom size on the performance of materials for the active layer in n-channel organic field effect transistors

## Publications

---

- Getmanenko, Y. A.; Purcell, T. A.; Hwang, D. K.; Kippelen, B.; Marder, S. R. **Easily Reducible Materials from the Reactions of Diselenopheno[3,2-b:2',3'-d]pyrrole and Dithieno[3,2-b:2',3'-d]pyrrole with Tetracyanoethylene.** *J. Org. Chem.* **2012**, *77*, 10931
- Purcell, T. A. R.; Galanty, M.; Yochelis, S.; Paltiel, Y.; Seideman, T. **Coupling Quantum Emitters to Random 2D Nanoplasmonic Structures.** *J. Phys. Chem. C.* **2016**, *120*, 21837–21842.
- Purcell, T. A. R.; Yochelis, S.; Paltiel, Y.; Seideman, T. **Determining the Molecular Dipole Orientation on Nanoplasmonic Structures.** *Accepted in J. Phys. Chem. C.*
- Purcell, T. A. R.; Seideman, T. **Modeling the Chiral Imprinting Response of Oriented Dipole Moments on Arbitrary Metal Nanostructures.** *Submitted to ACS Photonics.*
- Purcell, T. A. R.; Sukharev, M.; Seideman, T. **Modeling Optical Coupling of Plasmons and Inhomogeneously Broadened Emitters.** *In Preparation*

## Presentations

---

### Gordon Research Conference: Plasmonics and Nanophotonics

POSTER PRESENTER

Sunday River, ME

Jul. 2016

- Coupling Quantum Emitters to Random 2D Nanoplasmonic Structures

### Midwest Theoretical Chemistry Conference

POSTER PRESENTER

East Lansing, MI

Jun. 2017

- Coupling Quantum Emitters to Random 2D Nanoplasmonic Structures

### 255th American Chemical Society National Meeting

INVITED SPEAKER

New Orleans, LA

Mar. 2018

- Determining the orientation of molecular dipoles on random 2D nanoplasmonic structures

## Leadership

---

### Northwestern Energy Technology Group

VICE PRESIDENT

Northwestern University

Aug. 2015 - Aug. 2017

- Invited 3 speakers and organized 5-7 events per year to increase the discussion of how policy affects sustainability efforts
- Assisted the President with organizing biweekly board meetings to have evenly spaced events on a wide variety of topics

## **Northwestern Energy Technology Group**

*Northwestern University*

TREASURER

*Aug. 2014 - Aug. 2015*

- Managed the organizations budget of approximately \$2,000, and reimbursed members for cost of food and drinks for the events

## **Phi Lambda Upsilon**

*Northwestern University*

VICE PRESIDENT

*Aug. 2016 - Jul. 2017*

- Organized and managed the yearly undergraduate lab coat and goggle sales, raising over \$37,000
- Implemented universal use of point of sale to get a complete sales record
- Recruited 30 new members to the 120 member organization
- Secured a \$3,000 grant to ensure funding for Science in the Classroom

## **Phi Lambda Upsilon**

*Northwestern University*

SERVICE CHAIR

*Aug. 2015 - Jul. 2016*

- Coordinated between the teachers and graduate students to work out the logistics of teaching the lessons for Science in the Classroom
- Prepared all materials for the lessons to streamline the teaching process for group leaders and members
- Organized the final show for approximately 200 elementary school students at Northwestern University
- Reviewed service grant applications, leading to the renewal of the \$500 Lincolnwood Science Partnership
- Ran the Holiday Food Drive and Charity Fundraiser Social to raise more than \$2,000 for Connections for the Homeless
- Organized service events for the Chemistry Department, such as Sports and STEM Day and ETOPIA 2015 to enhance community impact

## **Service and Outreach**

---

### **Science in the Classroom**

*Northwestern University*

MEMBER AND GROUP LEADER

*Sept. 2014 - Jul. 2018*

- Taught interactive science lessons a class at local elementary school, to inspire students to enjoy science.
- Led a team of 5-6 graduate students to ensure we had enough people to run the lessons
- Participated in the final show at Northwestern where we can do larger scale demonstrations

### **CHEMUnity**

*Northwestern University*

MENTOR

*Aug. 2015 - Jul. 2018*

- Mentored a total of three incoming graduate students to ensure they had a smooth transition into the program as an inaugural mentor

### **Sports and STEM Day**

*Northwestern University*

ORGANIZER AND VOLUNTEER

*Sept. 2015, 2016, Oct. 2017*

- Collaborated with the Athletics Department to teach boy scouts and their families about science before a Northwestern football game
- Prepared the Chemistry Department's program, organized the graduate student volunteers, and helped preform the demonstrations to make an entertaining and educational program

## **Honors & Awards**

---

NORTHWESTERN UNIVERSITY

2017	<b>Gelewitz Award Finalist</b>
2015	<b>National Science Foundation GFRP Honorable Mention</b>
2013	<b>Pople Fellowship</b>

## NEW YORK UNIVERSITY

2013      **Arthur E. Hill Prize**  
2010, 2012, 2013   **Dean's List**  
2010      **Collegiate Research Scholar**

## Teaching Experience

---

### Northwestern University

TEACHING ASSISTANT

*Fall 2013 - Fall 2016*

- Taught a total of 5 classes (3 undergraduate and 2 graduate level)
- Reviewed material with students in the Principles of Physical Chemistry before they lectured the class
- Led review sessions of approximately 30 students to clarify points covered in class and in the homework
- Reviewed and helped write exams to ensure fair questioning
- Held office hours to answer any questions about classes from small groups of 5-10 students
- Managed General Chemistry Lab sections of 10-15 students so they could complete the experiments
- Graded assignments for the classes

## Professional Societies

---

- American Chemical Society
- American Physical Society
- Phi Lambda Upsilon

## References

---

### Tamar Seideman

T-SEIDEMAN@NORTHWESTERN.EDU

*Northwestern University*

*+1 847-467-4979*

### George Schatz

G-SCHATZ@NORTHWESTERN.EDU

*Northwestern University*

*+1 847-491-5657*

### Yossi Paltiel

PALTIEL@MAIL.HUJI.AC.IL

*Hebrew University of Jerusalem*

*+972 2-658-5760*